HYBRID SOLVATION MODELS FOR ELECTROSTATIC INTERACTIONS IN
MOLECULAR DYNAMICS SIMULATIONS OF IONIC SOLVENT

by

Ming Xiang

A dissertation submitted to the faculty of
The University of North Carolina at Charlotte
in partial fulfillment of the requirements
for the degree of Doctor of Philosophy in
Applied Mathematics

Charlotte

2012

Approved by:

_____

Dr. Wei Cai

_____

Dr. Shaozhong Deng

_____

Dr. Hae-Soo Oh

_____

Dr. Gregory J Gbur

ABSTRACT

MING XIANG. Hybrid solvation models for electrostatic interactions in molecular dynamics simulations of ionic solvent. (Under the direction of DR. WEI CAI)

In this dissertation, we mainly discuss the image approximation methods to the reaction field and their applications to electrostatic interactions in molecular dynamics simulations. The Poisson-Boltzman (PB) equation, a three-dimensional second order nonlinear elliptic partial differential equation arising in biophysics, as well as the Debye-Hückel theory are studied as fundamentals throughout this work.

We first outline a fourth-order image approximation proposed by Deng and Cai to the reaction field for a charge inside a dielectric sphere immersed in a solvent of low ionic strength [36]. To present such a reaction field, the image approximations employ a point charge at the classical Kelvin image point and two line charges that extend from the Kelvin image point along the radial direction to infinity. A sixth-order image approximation is then developed, using the same point charge with three different line charges. Procedures on how to discretize the line charges by point image charges and how to implement the resulting point image approximation in $O(N)$ complexity for potential and force field calculations are included. Numerical results demonstrate the sixth-order convergence rate of the image approximation and the $O(N)$ complexity of the fast implementation of the point image approximation.

We then apply the image-based reaction field method to the calculation for electrostatic interactions in molecular dynamics simulations. To extend a model developed by Lin *et al.* [30], a new hybrid solvation model, termed the Image-Charge Solvation Model (ICSM),

is extended for simulations of bioimolecules in ionic solvent, which combines the strengths of explicit and implicit solvent representations. In our model, an accurate and efficient multiple-image charge method to compute reaction fields is employed together with the fast multipole method for the direct Coulomb interactions. To minimize the surface effect, we pursue the periodic boundary strategy for nonelectrostatic interactions. We test our model in a simulation of sodium-chloride-water solvent. Using the Particle Mesh Ewald (PME) simulations as a reference, our results demonstrate that the proposed model can faithfully reproduce known solvation properties of sodium and chloride ions as well as many structural and dynamic properties of the water. We conclude that the employed model achieves convergence and controlled accuracy with only one image charge in the case of ionic solvent.

ACKNOWLEDGEMENTS

First and foremost, I owe my deepest gratitude to my advisor, Dr. Wei Cai for his guidance, supervision, motivation, and patience that extended far beyond this dissertation. His spirit of enquiry and insatiable quest for knowledge has always inspired me to be a better student and a better person. His immense knowledge in mathematics, physics, and biology helped me tremendously finish this dissertation.

I gratefully acknowledge Dr. Shaozhong Deng, who has always been willing to share his knowledge and expertise without reservation, and to help me with the research and writing when I needed it the most. He was always the first one I turned to when I had difficulties. I also would like to acknowledge Dr. Hae-Soo Oh and Dr. Gregory J Gbur as my committee members for their time and insights. The dissertation would not be possible without their generosity of attention.

In addition, the acknowledgement would not be complete if I did not mention my academic advisor Dr. Joel Avrin who has always been there to provide guidance since day one of my graduate study. I was constantly amazed by how many things he had to deal with everyday, but he was still so patient with any requests or questions I had and was always able to find a perfect solution to any of my problems.

I would like to thank Dr. Yuchun Lin and Wei Song. Dr. Lin introduced me to the field of molecular simulation and went out of his way to educate me on many aspects of the subject. He was always readily available to answer my questions even after he left the project team. Wei, a Ph.D. student at the department of physics and optical science, spent a lot of time helping me with my simulation code in spite of his own heavy workload.

TABLE OF CONTENTS

LIST OF TABLES

LIST OF FIGURES

CHAPTER 1: INTRODUCTION

1.1   Poisson equation

In this section, we motivate the material to follow by starting our contents from the Poisson equation - the fundamental of the basic theory of molecular dynamics simulation. A further discussion of the Poisson equation as well as the Poisson-Boltzman (PB) equation, based on the Debye-Hückel's potential of mean force (PMF) approximation for electrostatic interactions for biomolecules in ionic solvent, will be provided in Chapter 2 and 3. Let us begin with a quote from an article appearing in *Chemical Review* in 1990's [9]:

> *Electromagnetism is the force of chemistry. Combined with the consequences of quantum and statistical mechanics, electromagnetic forces maintain the structure and drive the processes of the chemistry around us and inside us. Because of the long-range nature of Coulombic interactions, electrostatics plays a particularly vital role in intra- and intermolecular interactions of chemistry and biochemistry.*

Currently, there is intensive study of the electrostatic structure and stability properties of biomolecules in an aqueous environment. The continuum models of molecules in ionic solutions first proposed in 1923 by Debye and Hückel were developed and applied to the medium comprising of the solute macromolecule and the surrounding ionic solvent

environment [10].

In this classical continuum approach, the solute is usually described as a region with a low dielectric constant ϵ_i, typically $\epsilon_i = 1 \sim 4$, and the enclosed atoms are treated explicitly, while the solvent, occupying the exterior of the solute, is generally assigned with a higher dielectric constant ϵ_o. Between the solute and solvent, the solute boundary Γ is defined by the molecular surface which is given by either the van der Waals (vdW) surface or the Solvent Accessible Surface (SAS), as shown in Figure 1.1 [5].
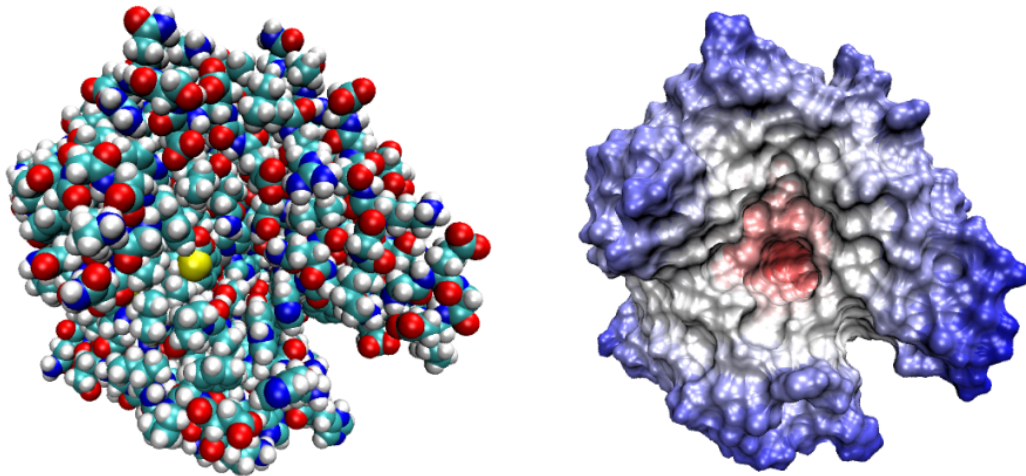
Figure 1.1: Molecular surfaces of the carbonic anhydrases-II. (Left) The van der Waals (vdW) surface of the domain composed of the sum of overlapping vdW spheres. (Right) The Solvent Accessible Surface (SAS) generated by rolling a small sphere on the vdW surface.

Due to the embedded charges in the solute and the mobile ionic charges in the solvent, the macroscopic potential $\Phi(\mathbf{r})$ at a field position $\mathbf{r}$ is described by the following Poisson equation:

$$-\nabla \cdot \epsilon(\mathbf{r})\nabla\Phi(\mathbf{r}) = \rho(\mathbf{r}) + \rho_n(\mathbf{r}), \tag{1.1}$$

where $\epsilon(\mathbf{r})$ is the dielectric constant function at the field position $\mathbf{r}$ and $\rho(\mathbf{r}) = \sum_j^N q_j\delta(\mathbf{r} - \mathbf{r}_j)$ is the interior charge distribution inside of the solute. q_j are the particle charges assigned

to atomic locations $\mathbf{r}_j$. $\rho_n(\mathbf{r})$ is given by

$$\rho_n(\mathbf{r}) = \sum_i n_i(\mathbf{r}) z_i e, \tag{1.2}$$

where $n_i(\mathbf{r})$ is the mobile ionic charge number density outside of the solute for the ions of

the type i at the field position $\mathbf{r}$.

At the boundary Γ, due to the discontinuities of dielectric constants inside and outside of

the solute, the continuities of the potential $\Phi(\mathbf{r})$ and the normal displacement flux require

two interface conditions given by

$$\Phi(\mathbf{r}^-) = \Phi(\mathbf{r}^+), \;\; \epsilon_i \frac{\partial \Phi(\mathbf{r}^-)}{\partial \mathbf{n}} = \epsilon_o \frac{\partial \Phi(\mathbf{r}^+)}{\partial \mathbf{n}}, \tag{1.3}$$

where $\mathbf{r}^-$ and $\mathbf{r}^+$ are the inner and outer limits at the position $\mathbf{r} \in \Gamma$, and $\mathbf{n}$ is the outward

unit normal to the surface of the solute.

1.2   Review of recent developments of methods for macroscopic electrostatic calculations in biological applications

As discussed in section 1.1, electrostatic interactions play a centrally important role in

computer simulations of chemical and biological systems in condensed phase. When

considering ionic materials, the electrostatic interaction is by far the dominant term and

can represent, typically, up to 90% of the total energy. A diverse class of physical

properties and processes in simulation systems such as equilibrium structures, reaction

rates, electronic spectra, charge separation and transfer, rely on the treatment of the

long-range electrostatic interactions. Although the approaches to treat electrostatic

interactions differ greatly in their conceptual framework, complexity, and technical detail,

the majority of these approaches can be broadly divided into two general categories:

implicit and explicit.

In implicit solvation models, the solute is treated 'explicitly' in atomic details while the solvent is modeled 'implicitly' as a dielectric continuum. To model the effect of solvent on the solute, Poisson or Poisson-Boltzmann (PB) equations are employed. A number of existing numerical algorithms are available for solving the PB equation in the simulation, including finite-difference, finite-element, and boundary-element methods. One advantage of this group of models is that with water molecules integrated out, implicit solvents present far fewer degrees of freedom in computer simulations than the explicit solvents. This greatly reduces the computational cost, which is the main motivation behind the development of the implicit models. However, in spite of much recent progress in developing numerical methods and formulating approximate treatment, the demanding numerical implementation of solving a three-dimensional PB equation for a macromolecule of arbitrary shape still presents a major challenge for the computer simulations. The approximate representation of discrete molecular solvent as continuum medium is another drawback of the implicit models, which is encountered in many situations mentioned in [36].

In contrast, explicit models represent the entire simulated system, both solute and solvent explicitly, namely, in atomic details, by assigning fixed charges to all atoms present in the system. A wide range of approaches have been developed to compute interactions among charges in the explicit solvents. These approaches include simple cutoff methods, a variety of lattice-sum methods such as Ewald summation, Particle Mesh Ewald (PME), and fast multipole methods (FMM), among which the lattice-sum methods are considered the most accurate. To avoid surface effects, periodic boundary conditions (PBCs) are used in the

simulations with explicit models. This application of PBCs eliminates the boundary of the central simulation box by introducing an infinite number of identical boxes around it throughout physical space on a lattice. However, periodicity also induces undesirable artifacts resulting from the interactions between particles in different image boxes. The effect of these artificial interactions depends on the sizes of box L. It was mentioned that large L significantly improves accuracy but increases the computational cost of the simulations, negatively affecting their practical use [30]. A more detailed discussion about the effect of L on reducing the periodicity artifacts can be found in [16]. Compared to explicit solvents, implicit model has a distinct advantage that they do not require PBCs and thus are not affected by the periodicity artifacts.

Combining their complementary strengths of both implicit and explicit approaches, a promising research strategy led to the development of numerous implicit/explicit models, also referred as hybrid models. A common design principle of all the hybrid models is the following: a central part of the simulation system containing the solute and some solvent is treated explicitly in atomic details while the rest of the surrounding part is modeled implicitly as dielectric continuum. Between these two explicit and implicit parts, a buffer layer is constructed in which molecules are treated atomically but experience forces that are different than those present in the central part, as shown in Figure 1.2. The total potential within the explicit solvent region is the sum of two types of potentials, namely, $\Phi_S + \Phi_{RF}$, where Φ_S is the direct electrostatic (or Coulomb) potential through which the charges in the explicit solvent region interact with one another; Φ_{RF} is the indirect reaction field resulting from the polarization of the continuum solvent region (implicit solvent part) by the explicit solvent charges.
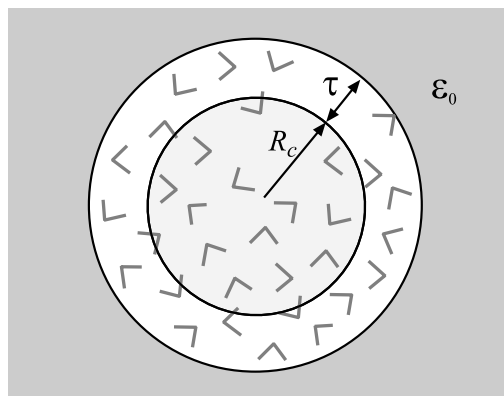
Figure 1.2: Cartoon illustrating the buffer layer filled with solvent.

How Φ_{RF} is computed becomes a major difference among the hybrid electrostatic solvation models. Friedman was first to apply an approach termed the image charge method in the context of the solvation problem [16]. This group of approaches computes the reaction field by one or more fictitious charges particles, called 'image charges', located outside of the area where potential is calculated. In a recent paper by Lin *et al*, a hybrid solvation model was introduced, in which the reaction fields are computed efficiently using the image charge method and the fast multipole expansion technique [30]. This model was successfully tested in a simulation of pure water solutions previously and is extended in this work to the ionic solutions with arbitrary ionic strength.

The structure of this thesis is as follows. In Chapter 2, a high-order image approximation to the ionic solvent induced reaction field is developed followed by the numerical results to validate the convergence property and investigate the efficiency of this image approximation. Next in Chapter 3, the image approximation methodology is applied on the biological molecular simulation. After a brief review of the basics of molecular dynamics simulation and a short description of mathematical formulation, a

new hybrid solvation model based on the image charge method is discussed and tested for simulations of biomolecules in ionic solvent. Finally, a conclusion is made in Chapter 4 followed by the intended future research topics.

CHAPTER 2: A SIXTH-ORDER IMAGE APPROXIMATION TO THE IONIC SOLVENT INDUCED REACTION FIELD

2.1   Background and exact solutions

2.1.1   Background

We concern fast and accurate calculation of electrostatic interactions among point charges inside a spherical dielectric cavity embedded in an ionic solvent of dissimilar dielectric constant. Such a problem could be encountered in many applications such as hybrid explicit/implicit solvent biomolecular dynamics simulations [28, 29, 36], in which biomolecules and a part of solvent molecules within a dielectric cavity are explicitly modeled while a surrounding dielectric continuum is used to model bulk effects of the solvent outside the cavity.

The point charges in the dielectric cavity will polarize the surrounding dielectric medium, which in turn generates a reaction field to the electric field throughout the cavity. The electric potential field inside the cavity is thus expressed as $\Phi_{\text{in}} = \Phi_{\text{S}} + \Phi_{\text{RF}}$, where Φ_{S} is the Coulomb potential given by the Coulomb's Law, and Φ_{RF} is the reaction field which will dominate the computational cost for calculating the electric field inside the cavity. Therefore, fast and accurate calculation of such a reaction field will have a wide impact on computational simulations for chemical and biological systems involving electrostatic interactions within a solvent.

In case of a spherical cavity, a popular approach to calculate the reaction field is the

method of images, in which the reaction field is represented in terms of potentials of discrete image charges. For the pure water solvent, namely, with no ions present in the solvent, a variety of approaches exist for calculating the reaction field for charges inside the spherical cavity, for example, the high-order accurate multiple image approximation [6] and references therein. For an ionic solvent, by assuming that the ionic strength of the solvent is low enough so that the product of the inverse Debye screening length of the solvent and the radius of the spherical cavity is less than one, image approximations of various orders (up to fourth-order) to the ionic solvent induced reaction field have been developed. More specifically, in [11], a first- and a second-order image approximations are presented using a point image charge at the classical Kelvin image point and a line image charge that extends from this Kelvin image point along the radial direction to infinity. Later in [12], a fourth-order image approximation and its improved version are obtained using the same point image charge together with two line image charges that extend from the Kelvin image point along the radial direction to infinity. Following the same procedure as used in [11, 12], we shall develop a sixth-order accurate image approximation to the ionic solvent induced reaction field, which will provide higher accuracy in the evaluation of potential and force fields inside the cavity.

2.1.2   Exact series solution to the ionic solvent induced reaction field

By the principle of linear superposition, the reaction field due to a single point charge q inside a spherical cavity of radius a centered at the origin only needs to be considered. The sphere has a dielectric constant ϵ_i, and the surrounding ionic solvent is represented as a homogeneous medium of a dielectric constant ϵ_o. The point charge q is located on

the x-axis inside the sphere at a distance $r_\mathrm{s} < a$ from the spherical center, as shown in Figure 2.1.
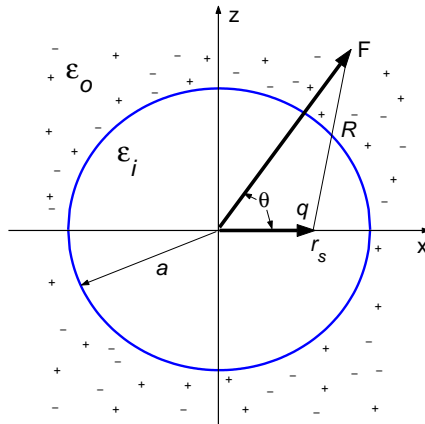
Figure 2.1: A point charge and a dielectric sphere immersed in an ionic solvent.

It is well-known that the total electric potential $\Phi_\mathrm{in}(\mathbf{r})$ inside the cavity is given by the solution of the Poisson equation

$$\nabla \cdot (\epsilon_\mathrm{i} \nabla \Phi_\mathrm{in}(\mathbf{r})) = -q\delta(|\mathbf{r} - \mathbf{r}_\mathrm{s}|), \tag{2.1}$$

where $\delta(r)$ denotes the Dirac delta function. Moreover, this potential can be expressed as $\Phi_\mathrm{in}(\mathbf{r}) = \Phi_\mathrm{S}(\mathbf{r}) + \Phi_\mathrm{RF}(\mathbf{r})$, where $\Phi_\mathrm{S}(\mathbf{r})$ is the Coulomb potential due to the source charge q alone, and $\Phi_\mathrm{RF}(\mathbf{r})$ is the reaction potential due to the polarization of the outside dielectric medium.

Outside the cavity, on the other hand, by assuming that the mobile ion concentration follows the Debye-Hückel theory, namely, the mobile ion charges follow a Boltzmann distribution in the mean field approximation, for a solvent of low ionic strength, the electric potential $\Phi_\mathrm{out}(\mathbf{r})$ is then given by the solution of the linearized Poisson-Boltzmann equation (LPBE) [24]

$$\nabla^2 \Phi_\mathrm{out}(\mathbf{r}) - \lambda^2 \Phi_\mathrm{out}(\mathbf{r}) = 0, \tag{2.2}$$

here λ is the inverse Debye screening length determined by

$$\lambda^2 = \frac{8\pi N_A e^2 \rho_A}{1000\epsilon_o k_B T} c_s, \tag{2.3}$$

where N_A is Avogadro's number, ρ_A is the solvent density, e is the protonic charge $(4.803 \times 10^{-10}$esu), k_B is the Boltzmann constant, T is the absolute temperature, and c_s is the ionic concentration measured in molar units. From (2.3), we see that the inverse Debye screening length λ is proportional to the square root of the ionic concentration c_s. In particular, for 1:1 electrolytes (monovalent:monovalent salts like NaCl),

$$\lambda \approx 0.33\sqrt{c_s}\text{Å}^{-1} \tag{2.4}$$

at room temperature (25°), with ϵ_o=78.5 and Å=10^{-10}m [38].

On the interface Γ of the dielectric cavity and its surrounding dielectric medium, the following two boundary conditions are to be satisfied for the continuities of the potential and the fluxes along the normal direction of the interface

$$\Phi_{\text{out}}|_\Gamma = \Phi_{\text{in}}|_\Gamma \quad \text{and} \quad \epsilon_o \frac{\partial \Phi_{\text{out}}}{\partial \mathbf{n}}\bigg|_\Gamma = \epsilon_i \frac{\partial \Phi_{\text{in}}}{\partial \mathbf{n}}\bigg|_\Gamma, \tag{2.5}$$

where $\mathbf{n}$ is the unit outward vector normal to the surface of the cavity.

Using the classical electrostatic theory, the reaction field of the spherical dielectric can be solved analytically [11]. More precisely, with respect to a spherical coordinate system (r, θ, ϕ) originating in the center of the sphere (*the pole is denoted by the x-axis in this paper*), due to the azimuthal symmetry, the reaction field at a point $\mathbf{r}=(r, \theta, \phi)$ inside the sphere takes on the form

$$\Phi_{\text{RF}}(\mathbf{r}) = \sum_{n=0}^{\infty} A_n r^n P_n(\cos\theta), \tag{2.6}$$

where $P_n(x)$ represent the Legendre polynomials and A_n are the expansion coefficients
given by

$$A_n = \frac{q}{\epsilon_i a} \frac{1}{r_K^n} \frac{\epsilon_i(n+1)k_n(u) + \epsilon_o u k_n'(u)}{\epsilon_i n k_n(u) - \epsilon_o u k_n'(u)}, \qquad n \geq 0, \qquad (2.7)$$

where $u = \lambda a$, $r_K = a^2/r_S$ with $\mathbf{r}_K = (r_K, 0, 0)$ denoting the classical Kelvin image point, and
$k_n(r)$ are the modified spherical Hankel functions [1, 19]

$$k_n(r) = \frac{\pi}{2r} e^{-r} \sum_{k=0}^{n} \frac{(n+k)!}{k!(n-k)!} \frac{1}{(2r)^k}, \qquad n \geq 0. \qquad (2.8)$$

In theory, any desired degree of accuracy can be obtained using the direct series
expansion (2.6). In the case that the point charge is close to the spherical boundary, when
calculating the reaction field at an observation point also close to the boundary, the
convergence of the series expansion is slow due to the fact that $r/r_K = r r_S/a^2 \approx 1$,
requiring a great number of terms in the series expansion to achieve satisfactory accuracy
in the reaction field.

2.2   Line and point image approximations to the reaction field

Let us now turn ourselves to the problem of finding image charges outside the spherical
region giving rise to the reaction potential inside the sphere. For the pure water solvent,
such image charges include a point charge at the classical Kelvin image point and a
continuous line charge extending along the radial direction from this Kelvin image point
to infinity [31, 34, 35]. For an ionic solvent, as mentioned earlier, by assuming that the
ionic strength of the solvent is low enough such that the product of the inverse Debye
screening length λ (which is proportional to the square root of the ionic concentration)
and the radius of the spherical cavity a is less than one ($u = \lambda a < 1$), several image

approximations of various orders (in terms of $u=\lambda a$) to the ionic solvent induced reaction field have been developed [11, 12]. It should be emphasized again that the assumption of $u=\lambda a < 1$ is physically justifiable since the condition of low ionic strength is required for the linearization of the Poisson-Boltzmann equation to be meaningful.

2.2.1 Previous first- and second-order image approximations

In this subsection, we review the mathematical formulation of a previous paper [11]. The key idea in the development of the foregoing image charge methods is to approximate $k_n(u)/uk_n'(u)$ with simple rational functions of n when u is small. In fact, by applying the expansion of the modified spherical Hankel function

$$k_n(r) = \pi \frac{(2n)!}{(n)!} \frac{1}{(2r)^{n+1}} + O\left(\frac{1}{r^n}\right), \quad n \geq 0, \tag{2.9}$$

which essentially implies

$$\frac{k_n(r)}{rk_n'(r)} = -\frac{1}{n+1} + O(r), \qquad n \geq 0,$$

a first-order image approximation to the ionic solvent induced reaction field can be obtained as follows [11]

$$\Phi_{\mathrm{RF}}(\mathbf{r}) = \frac{q_{\mathrm{K}}}{\epsilon_{\mathrm{i}}|\mathbf{r} - \mathbf{r}_{\mathrm{K}}|} + \int_{r_{\mathrm{K}}}^{\infty} \frac{\hat{q}_{\mathrm{L0}}(x)}{\epsilon_{\mathrm{i}}|\mathbf{r} - \mathbf{x}|} \mathrm{d}x + O(u), \tag{2.10}$$

where the point image charge q_{K} and the line image charge $\hat{q}_{\mathrm{L0}}(x)$ are defined by

$$q_{\mathrm{K}} = \gamma \frac{a}{r_{\mathrm{S}}} q, \quad \hat{q}_{\mathrm{L0}}(x) = \frac{\hat{\delta}_0 q}{a} \left(\frac{x}{r_{\mathrm{K}}}\right)^{-\hat{\sigma}_0}, \qquad r_{\mathrm{K}} \leq x,$$

respectively, where

$$\gamma = \frac{\epsilon_i - \epsilon_o}{\epsilon_i + \epsilon_o}, \quad \hat{\sigma}_0 = \frac{\epsilon_o}{\epsilon_i + \epsilon_o}, \quad \hat{\delta}_0 = \frac{\epsilon_i(\epsilon_i - \epsilon_o)}{(\epsilon_i + \epsilon_o)^2}.$$

Note that neither of the point charge q_K and the line charge $\hat{q}_{L0}(x)$ depends on the inverse Debye screening length λ, indicating that in essence the first-order image approximation to the ionic solvent induced reaction field totally ignores the ionic strength effect in the reaction potential. Hence, more accurate image approximations have to be developed to account for the ionic strength effect. To this end, by noticing that instead of the $(1/r^n)$ truncation error as described in (2.9), in fact we have

$$k_n(r) = \pi \frac{(2n)!}{(n)!} \frac{1}{(2r)^{n+1}} + O\left(\frac{1}{r^{n-1}}\right), \quad n \geq 1, \tag{2.11}$$

The first-order image approximation thus can be improved by simply including a constant, position-independent correction potential, resulting in the following second-order image approximation to the ionic solvent induced reaction field [11]:

$$\Phi_{RF}(\mathbf{r}) = \frac{q_K}{\epsilon_i|\mathbf{r} - \mathbf{r}_K|} + \int_{r_K}^{\infty} \frac{\hat{q}_{L0}(x)}{\epsilon_i|\mathbf{r} - \mathbf{x}|} dx + \hat{\Phi}_{C1}(\mathbf{r}) + O(u^2), \tag{2.12}$$

with the constant, position-independent correction potential $\hat{\Phi}_{C1}$ defined by

$$\hat{\Phi}_{C1} = \frac{q}{\epsilon_i a}\left(C_0(u) - \gamma - \frac{\hat{\delta}_0}{\hat{\sigma}_0}\right),$$

where

$$C_0(u) = \frac{\epsilon_i - (1 + u)\epsilon_o}{(1 + u)\epsilon_o}. \tag{2.13}$$

Moreover, the accuracy of the second-order image approximation (2.12) can be further improved by including another position-dependent correction potential, yielding the

improved second-order image approximation [11]

$$\Phi_{\mathrm{RF}}(\mathbf{r}) = \frac{q_{\mathrm{K}}}{\epsilon_{\mathrm{i}}|\mathbf{r} - \mathbf{r}_{\mathrm{K}}|} + \int_{r_{\mathrm{K}}}^{\infty} \frac{\hat{q}_{\mathrm{L0}}(x)}{\epsilon_{\mathrm{i}}|\mathbf{r} - \mathbf{x}|} \mathrm{d}x + \hat{\Phi}_{\mathrm{C1}} + \hat{\Phi}_{\mathrm{C2}}(\mathbf{r}) + O(u^2), \tag{2.14}$$

with the *position-dependent* correction potential $\hat{\Phi}_{\mathrm{C2}}(\mathbf{r})$ defined by

$$\hat{\Phi}_{\mathrm{C2}}(\mathbf{r}) = \frac{q}{\epsilon_{\mathrm{i}}a} \left(C_1(u) - \gamma - \frac{\hat{\delta}_0}{1 + \hat{\sigma}_0} \right) \left(\frac{r}{r_{\mathrm{K}}} \right) \cos\theta,$$

where

$$C_1(u) = \frac{2(1 + u)\epsilon_{\mathrm{i}} - (2 + 2u + u^2)\epsilon_{\mathrm{o}}}{(1 + u)\epsilon_{\mathrm{i}} + (2 + 2u + u^2)\epsilon_{\mathrm{o}}}. \tag{2.15}$$

2.2.2 Previous fourth-order image approximations

Using the same key idea as Section 2.2.1, a fourth-order image approximation is obtained

in [12]. In fact, by applying the expansion of the modified spherical Hankel function

$$k_n(r) = \pi \frac{(2n - 2)!}{(n - 1)!} \left(\frac{2(2n - 1)}{(2r)^{n+1}} - \frac{1}{4(2r)^{n-1}} \right) + O\left(\frac{1}{r^{n-3}} \right), \; n \geq 2, \tag{2.16}$$

which essentially implies

$$\frac{k_n(r)}{rk'_n(r)} = -\frac{-(2 + r^2) + 4n}{(r^2 - 2) + (2 - r^2)n + 4n^2} + O(r^4), \qquad n \geq 2,$$

a fourth-order image approximation to the ionic solvent induced reaction field can be obtained as follows [12]

$$\Phi_{\mathrm{RF}}(\mathbf{r}) = \frac{q_{\mathrm{K}}}{\epsilon_{\mathrm{i}}|\mathbf{r} - \mathbf{r}_{\mathrm{K}}|} + \int_{r_{\mathrm{K}}}^{\infty} \frac{\hat{q}_{\mathrm{L1}}(x)}{\epsilon_{\mathrm{i}}|\mathbf{r} - \mathbf{x}|} \mathrm{d}x + \int_{r_{\mathrm{K}}}^{\infty} \frac{\hat{q}_{\mathrm{L2}}(x)}{\epsilon_{\mathrm{i}}} \left(\frac{1}{|\mathbf{r} - \mathbf{x}|} - \frac{1}{x} \right) \mathrm{d}x$$

$$+ \hat{\Phi}_{\mathrm{C0}} + \hat{\Phi}_{\mathrm{C1}}(\mathbf{r}) + O(u^4), \tag{2.17}$$

where the constant *position-independent* correction potential $\hat{\Phi}_{\mathrm{C0}}$ and the *position-dependent* correction potential $\hat{\Phi}_{\mathrm{C1}}(\mathbf{r})$ are defined as

$$\hat{\Phi}_{\mathrm{C0}} = \frac{q}{\epsilon_{\mathrm{i}} a} \left(C_0(u) - \gamma - \frac{\hat{\delta}_1}{\hat{\sigma}_1} \right), \tag{2.18}$$

$$\hat{\Phi}_{\mathrm{C1}}(\mathbf{r}) = \frac{q}{\epsilon_{\mathrm{i}} a} \left(C_1(u) - \gamma - \frac{\hat{\delta}_1}{1 + \hat{\sigma}_1} - \frac{\hat{\delta}_2}{1 - \hat{\sigma}_2} \right) \left(\frac{r}{r_{\mathrm{K}}} \right) \cos \theta, \tag{2.19}$$

respectively. Here we denote

$$C_0(u) = \frac{\epsilon_{\mathrm{i}} - (1 + u)\epsilon_{\mathrm{o}}}{(1 + u)\epsilon_{\mathrm{o}}}, \tag{2.20}$$

$$C_1(u) = \frac{2(1 + u)\epsilon_{\mathrm{i}} - (2 + 2u + u^2)\epsilon_{\mathrm{o}}}{(1 + u)\epsilon_{\mathrm{i}} + (2 + 2u + u^2)\epsilon_{\mathrm{o}}}. \tag{2.21}$$

The point image charge q_{K} and the two line image charges $\hat{q}_{\mathrm{L1}}(x)$ and $\hat{q}_{\mathrm{L2}}(x)$ are defined by

$$q_{\mathrm{K}} = \gamma \frac{a}{r_{\mathrm{S}}} q, \ \ \hat{q}_{\mathrm{L1}}(x) = \frac{\hat{\delta}_1 q}{a} \left(\frac{x}{r_{\mathrm{K}}} \right)^{-\hat{\sigma}_1}, \ \ \hat{q}_{\mathrm{L2}}(x) = \frac{\hat{\delta}_2 q}{a} \left(\frac{x}{r_{\mathrm{K}}} \right)^{\hat{\sigma}_2}, \qquad r_{\mathrm{K}} \le x,$$

respectively, where $\hat{\sigma}_1, \hat{\delta}_1, \hat{\sigma}_2, \hat{\delta}_2$ are defined in [12], and $\gamma = (\epsilon_{\mathrm{i}} - \epsilon_{\mathrm{o}})/(\epsilon_{\mathrm{i}} + \epsilon_{\mathrm{o}})$.

Moreover, the accuracy of the fourth-order image approximation (2.17) can be further improved by including another *position-dependent* correction potential, yielding the

improved fourth-order image approximation [12]

$$\Phi_{\mathrm{RF}}(\mathbf{r}) = \frac{q_{\mathrm{K}}}{\epsilon_{\mathrm{i}}|\mathbf{r} - \mathbf{r}_{\mathrm{K}}|} + \int_{r_{\mathrm{K}}}^{\infty} \frac{\hat{q}_{\mathrm{L1}}(x)}{\epsilon_{\mathrm{i}}|\mathbf{r} - \mathbf{x}|} \mathrm{d}x + \int_{r_{\mathrm{K}}}^{\infty} \frac{\hat{q}_{\mathrm{L2}}(x)}{\epsilon_{\mathrm{i}}} \left(\frac{1}{|\mathbf{r} - \mathbf{x}|} - \frac{1}{x} \right) \mathrm{d}x$$

$$+ \hat{\Phi}_{\mathrm{C0}} + \hat{\Phi}_{\mathrm{C1}}(\mathbf{r}) + \hat{\Phi}_{\mathrm{C2}}(\mathbf{r}) + O(u^4), \tag{2.22}$$

with the *position-dependent* correction potential $\hat{\Phi}_{\mathrm{C2}}(\mathbf{r})$ defined by

$$\hat{\Phi}_{\mathrm{C2}}(\mathbf{r}) = \frac{q}{\epsilon_{\mathrm{i}} a} \left(C_2(u) - \gamma - \frac{\hat{\delta}_1}{2 + \hat{\sigma}_1} - \frac{\hat{\delta}_2}{2 - \hat{\sigma}_2} \right) \left(\frac{r}{r_{\mathrm{K}}} \right)^2 P_2(\cos\theta),$$

where

$$C_2(u) = \frac{3(3 + 3u + u^2)\epsilon_{\mathrm{i}} - (9 + 9u + 4u^2 + u^3)\epsilon_{\mathrm{o}}}{2(3 + 3u + u^2)\epsilon_{\mathrm{i}} + (9 + 9u + 4u^2 + u^3)\epsilon_{\mathrm{o}}}. \tag{2.23}$$

2.2.3 Formulation of the sixth-order image approximation

To construct a sixth-order image approximation for better accuracy, by using the Taylor

expansion

$$e^{-r} = 1 - r + \frac{r^2}{2} - \frac{r^3}{6} + \frac{r^4}{24} - \frac{r^5}{120} + O(r^6),$$

and the truncation

$$\sum_{k=0}^{n} \frac{(n+k)!}{k!(n-k)!} \frac{1}{(2r)^k} = \sum_{k=0}^{5} \frac{(2n-k)!}{k!(n-k)!} \frac{1}{(2r)^{n-k}} + O\left(\frac{1}{r^{n-6}} \right), \quad n \geq 5,$$

one can arrive at the expansion of the modified spherical Hankel function in terms of $1/r$

as follows

$$k_n(r) = \pi \frac{(2n-4)!}{(n-2)!} \left[\frac{4(2n-1)(2n-3)}{(2r)^{n+1}} - \frac{2n-3}{2(2r)^{n-1}} + \frac{1}{32(2r)^{n-3}} \right] + O\left(\frac{1}{r^{n-5}} \right), \ n \geq 5.$$

$$\tag{2.24}$$

However, after expanding $k_4(r)$ directly in terms of $1/r$, it turns out that (2.24) is also true

for $n=4$. Correspondingly, the derivative of the modified spherical Hankel function can be

expanded as

$$k_n'(r) = -\pi \frac{(2n-4)!}{(n-2)!} \left[\frac{8(2n-3)(2n-1)(n+1)}{(2r)^{n+2}} \right.$$
$$\left. - \frac{(2n-3)(n-1)}{(2r)^n} + \frac{n-3}{16(2r)^{n-2}} \right] + O\left(\frac{1}{r^{n-4}}\right), \quad n \geq 4. \quad (2.25)$$

Consequently, for $n \geq 4$ we obtain

$$\frac{k_n(r)}{rk_n'(r)} = -\frac{r^4 + 12r^2 + 24 - 8(r^2+8)n + 32n^2}{-3(r^4+4r^2-8) + (r^4+20r^2-40)n - 8(r^2+4)n^2 + 32n^3} + O(r^6).$$

Inserting this approximation into (2.7) leads to

$$A_n = \frac{q}{\epsilon_i a} \frac{1}{r_K^n} \frac{a_1 + a_2 n + a_3 n^2 + a_4 n^3}{b_1 + b_2 n + b_3 n^2 + b_4 n^3} + O(u^6), \quad n \geq 4,$$

where

$$a_1 = 24(\epsilon_i - \epsilon_o) + 12\epsilon_i u^2 + 12\epsilon_o u^2 + \epsilon_i u^4 + 3\epsilon_o u^4,$$

$$a_2 = -40(\epsilon_i - \epsilon_o) + 4\epsilon_i u^2 - 20\epsilon_o u^2 + \epsilon_i u^4 - \epsilon_o u^4,$$

$$a_3 = -32(\epsilon_i - \epsilon_o) - 8\epsilon_i u^2 + 8\epsilon_o u^2,$$

$$a_4 = 32(\epsilon_i - \epsilon_o),$$

$$b_1 = -3\epsilon_o(u^4 + 4u^2 - 8),$$

$$b_2 = -64\epsilon_o + 24(\epsilon_i + \epsilon_o) + 12\epsilon_i u^2 + 20\epsilon_o u^2 + \epsilon_i u^4 + \epsilon_o u^4,$$

$$b_3 = -8(8\epsilon_i + 4\epsilon_o + (\epsilon_i + \epsilon_o)u^2),$$

$$b_4 = 32(\epsilon_i + \epsilon_o).$$

After some algebraic manipulations, the expansion coefficients A_n can be further expressed as

$$A_n = \frac{q}{\epsilon_i a} \frac{1}{r_K^n} \left(\gamma + \frac{\alpha_1 + \alpha_2 n + \alpha_3 n^2}{\beta_1 + \beta_2 n + \beta_3 n^2 + n^3} \right) + O(u^6), \qquad n \geq 4,$$

where

$$\alpha_1 = \frac{a_1}{b_4} - \gamma\beta_1, \quad \beta_1 = \frac{b_1}{b_4},$$

$$\alpha_2 = \frac{a_2}{b_4} - \gamma\beta_2, \quad \beta_2 = \frac{b_2}{b_4},$$

$$\alpha_3 = \frac{a_3}{b_4} - \gamma\beta_3, \quad \beta_3 = \frac{b_3}{b_4}.$$

Now using the root-finding formula for a cubic equation [43], one can get the three roots of the equation $\beta_1 + \beta_2 n + \beta_3 n^2 + n^3 = 0$ as

$$n_1 = \frac{1}{3}\left[-\beta_3 - A^{\frac{1}{2}}\left(\cos\left(\frac{\varphi}{3}\right) + \sqrt{3}\sin\left(\frac{\varphi}{3}\right) \right) \right] = \frac{1}{3}\left[-\beta_3 - 2A^{\frac{1}{2}}\sin\left(\frac{\pi}{6} + \frac{\varphi}{3}\right) \right],$$

$$n_2 = \frac{1}{3}\left[-\beta_3 - A^{\frac{1}{2}}\left(\cos\left(\frac{\varphi}{3}\right) - \sqrt{3}\sin\left(\frac{\varphi}{3}\right) \right) \right] = \frac{1}{3}\left[-\beta_3 - 2A^{\frac{1}{2}}\sin\left(\frac{\pi}{6} - \frac{\varphi}{3}\right) \right],$$

$$n_3 = \frac{1}{3}\left[-\beta_3 + 2A^{\frac{1}{2}}\cos\left(\frac{\varphi}{3}\right) \right],$$

where

$$A = \beta_3^2 - 3\beta_2, \quad B = \frac{9\beta_2\beta_3 - 27\beta_1 - 2\beta_3^3}{54},$$

$$\rho = \sqrt{\left(\frac{A}{9}\right)^3}, \quad \varphi = \arccos\left(\frac{B}{\rho}\right).$$

Theorem 1. *If* $0 \leq u \leq 1$, *then the three roots* n_1, n_2 *and* n_3 *of the cubic equation* $\beta_1 + \beta_2 n + \beta_3 n^2 + n^3 = 0$ *satisfy*

$$-1 < n_1 < 0 < n_2 < 1 < n_3 < 2.$$

Proof: Let

$$f(n) = (b_1 + b_2 n + b_3 n^2 + b_4 n^3)/\epsilon_o.$$

Then, we have

$$f(-1) = -4u^4 - 40u^2 - 20\epsilon_r u^2 - 120\epsilon_r - \epsilon_r u^4,$$

$$f(0) = -3u^4 + 24 - 12u^2,$$

$$f(1) = -2u^4 - 16 + 4\epsilon_r u^2 - 8\epsilon_r + \epsilon_r u^4,$$

$$f(2) = -u^4 + 72 - 4u^2 - 8\epsilon_r u^2 + 48\epsilon_r + 2\epsilon_r u^4,$$

where $\epsilon_r = \epsilon_i/\epsilon_o > 0$. For $0 \le u \le 1$, it can be seen that

$$f(-1) < 0, \quad f(0) > 0, \quad f(1) < 0, \quad f(2) > 0,$$

indicating that the equation $f(n) = 0$ has exactly one root in each of the three open intervals $(-1, 0), (0, 1)$ and $(1, 2)$.

On the other hand, note that for $0 \le \varphi \le \pi$, we have

$$n_1 \le \frac{1}{3}\left(-\beta_3 - A^{\frac{1}{2}}\right) \le n_2 \le \frac{1}{3}\left(-\beta_3 + A^{\frac{1}{2}}\right) \le n_3,$$

and that n_1, n_2 and n_3 are also the three roots of the equation $f(n) = 0$. Therefore, we must have

$$-1 < n_1 < 0 < n_2 < 1 < n_3 < 2.$$

Then, using partial fractions gives us

$$A_n = \frac{q}{\epsilon_i a} \frac{1}{r_K^n}\left(\gamma + \frac{\delta_1}{n + \sigma_1} + \frac{\delta_2}{n - \sigma_2} + \frac{\delta_3}{n - \sigma_3}\right) + O(u^6), \ n \ge 4, \tag{2.26}$$

where $\sigma_1 = -n_1$, $\sigma_2 = n_2$, $\sigma_3 = n_3$, and

$$\delta_1 = \frac{\sigma_1^2 \alpha_3 - \sigma_1 \alpha_2 + \alpha_1}{(\sigma_1 + \sigma_2)(\sigma_1 + \sigma_3)},$$

$$\delta_2 = \frac{\sigma_2^2 \alpha_3 + \sigma_2 \alpha_2 + \alpha_1}{(\sigma_1 + \sigma_2)(\sigma_2 - \sigma_3)},$$

$$\delta_3 = \frac{\sigma_3^2 \alpha_3 + \sigma_3 \alpha_2 + \alpha_1}{(\sigma_1 + \sigma_3)(\sigma_2 + \sigma_3)}.$$

On the other hand, for $n \leq 3$, directly applying the exact expressions of $k_0(r)$, $k_1(r)$, $k_2(r)$ and $k_3(r)$, in fact we can arrive at

$$\frac{k_0(r)}{r k_0'(r)} = -\frac{1}{1+r},$$

$$\frac{k_1(r)}{r k_1'(r)} = -\frac{1+r}{2+2r+r^2},$$

$$\frac{k_2(r)}{r k_2'(r)} = -\frac{3+3r+r^2}{9+9r+4r^2+r^3},$$

$$\frac{k_3(r)}{r k_3'(r)} = -\frac{90+30r+6r^2+r^3}{270+150r+36r^2+6r^3+r^4},$$

and accordingly, we have

$$A_j = C_j(u) \frac{q}{\epsilon_i a} \left(\frac{1}{r_{\mathrm{K}}^j} \right), \quad j = 0, 1, 2, 3, \tag{2.27}$$

where $C_0(u)$, $C_1(u)$ and $C_2(u)$ are given in (2.20), (2.21) and (2.23), respectively, and $C_3(u)$ is defined below

$$C_3(u) = \frac{4(15+15u+6u^2+u^3)\epsilon_i - (60+60u+27u^2+7u^3+u^4)\epsilon_o}{3(15+15u+6u^2+u^3)\epsilon_i + (60+60u+27u^2+7u^3+u^4)\epsilon_o}. \tag{2.28}$$

Inserting now the approximation of A_n given by (2.26) into (2.6), the reaction field inside the sphere can be expressed as

$$\Phi_{\mathrm{RF}}(\mathbf{r}) = \sum_{n=0}^{3} A_n r^n P_n(\cos\theta) + S_1 + S_2 + S_3 + S_4 + O(u^6), \tag{2.29}$$

where S_1, S_2, S_3 and S_4 represent the following four series

$$S_1 = \frac{\gamma q}{\epsilon_i a} \sum_{n=4}^{\infty} \left(\frac{r}{r_K}\right)^n P_n(\cos\theta),$$

$$S_2 = \frac{\delta_1 q}{\epsilon_i a} \sum_{n=4}^{\infty} \frac{1}{n + \sigma_1} \left(\frac{r}{r_K}\right)^n P_n(\cos\theta),$$

$$S_3 = \frac{\delta_2 q}{\epsilon_i a} \sum_{n=4}^{\infty} \frac{1}{n - \sigma_2} \left(\frac{r}{r_K}\right)^n P_n(\cos\theta),$$

$$S_4 = \frac{\delta_3 q}{\epsilon_i a} \sum_{n=4}^{\infty} \frac{1}{n - \sigma_3} \left(\frac{r}{r_K}\right)^n P_n(\cos\theta).$$

Now, the problem reduces to how to represent each of the above four series by a line image charge. To this end, we recall that the Coulomb potential $\Phi_s(\mathbf{r})$, the potential at $\mathbf{r}$ due to a point charge q at $\mathbf{r}_s$, can be expanded in terms of the Legendre polynomials of $\cos\theta$ as follows [33].

$$\Phi_s(\mathbf{r}) = \frac{q}{\epsilon_i|\mathbf{r} - \mathbf{r}_s|} = \begin{cases} \dfrac{q}{\epsilon_i r} \displaystyle\sum_{n=0}^{\infty} \left(\dfrac{r_s}{r}\right)^n P_n(\cos\theta), & r_s \leq r \leq a, \\ \dfrac{q}{\epsilon_i r_s} \displaystyle\sum_{n=0}^{\infty} \left(\dfrac{r}{r_s}\right)^n P_n(\cos\theta), & 0 \leq r \leq r_s. \end{cases} \tag{2.30}$$

First, in order to obtain an image representation for the series S_1, we note that it can be written as

$$S_1 = \frac{\gamma q}{\epsilon_i r_K} \frac{a}{r_s} \sum_{n=0}^{\infty} \left(\frac{r}{r_K}\right)^n P_n(\cos\theta) - \frac{\gamma q}{\epsilon_i a} \sum_{n=0}^{3} \left(\frac{r}{r_K}\right)^n P_n(\cos\theta),$$

where the first part is exactly the expansion of the potential at $\mathbf{r}$ due to a point charge of magnitude q_K outside the sphere at the classical Kelvin image point $\mathbf{r}_K = (r_K, 0, 0)$. Therefore, we have

$$S_1 = \frac{q_K}{\epsilon_i|\mathbf{r} - \mathbf{r}_K|} - \frac{\gamma q}{\epsilon_i a} \sum_{n=0}^{3} \left(\frac{r}{r_K}\right)^n P_n(\cos\theta). \tag{2.31}$$

Next, to find an image representation for the second series S_2, we need the integral identity which can be regarded as a Mellin transformation

$$\frac{1}{n+\sigma} = r_{\text{K}}^{n+\sigma} \int_{r_{\text{K}}}^{\infty} \frac{1}{x^{n+\sigma+1}} \, \mathrm{d}x, \tag{2.32}$$

and is valid for all $n \geq 0$ when $\sigma > 0$. Inserting (2.32) with $\sigma=\sigma_1$ into S_2 yields

$$S_2 = \int_{r_{\text{K}}}^{\infty} \left[\frac{q_{\text{L1}}(x)}{\epsilon_{\text{i}} x} \sum_{n=0}^{\infty} \left(\frac{r}{x} \right)^n P_n(\cos\theta) \right] \mathrm{d}x - \frac{\delta_1 q}{\epsilon_{\text{i}} a} \sum_{n=0}^{3} \frac{1}{n+\sigma_1} \left(\frac{r}{r_{\text{K}}} \right)^n P_n(\cos\theta),$$

where

$$q_{\text{L1}}(x) = \frac{\delta_1 q}{a} \left(\frac{x}{r_{\text{K}}} \right)^{-\sigma_1}, \qquad r_{\text{K}} \leq x. \tag{2.33}$$

Note that the integrand in the above integral again becomes the expansion given by (2.30) for a charge of magnitude $q_{\text{L1}}(x)$ outside the sphere at the point $\mathbf{x}=(x,0,0)$. Therefore, $q_{\text{L1}}(x)$ can be regarded as a continuous line charge which stretches from the classical Kelvin image point $\mathbf{r}_{\text{K}}$ along the radial direction to infinity. Thus, the second series S_2 becomes

$$S_2 = \int_{r_{\text{K}}}^{\infty} \frac{q_{\text{L1}}(x)}{\epsilon_{\text{i}} |\mathbf{r} - \mathbf{x}|} \mathrm{d}x - \frac{\delta_1 q}{\epsilon_{\text{i}} a} \sum_{n=0}^{3} \frac{1}{n+\sigma_1} \left(\frac{r}{r_{\text{K}}} \right)^n P_n(\cos\theta). \tag{2.34}$$

To find image representations for the series S_3 and S_4, we use a similar integral identity

$$\frac{1}{n-\sigma} = r_{\text{K}}^{n-\sigma} \int_{r_{\text{K}}}^{\infty} \frac{1}{x^{n-\sigma+1}} \, \mathrm{d}x, \tag{2.35}$$

which is valid for all $n \geq 1$ when $\sigma < 1$ and valid for all $n \geq 2$ when $\sigma < 2$. Inserting this into S_3 yields

$$S_3 = \int_{r_{\text{K}}}^{\infty} \frac{q_{\text{L2}}(x)}{\epsilon_{\text{i}}} \left[\sum_{n=0}^{\infty} \frac{1}{x} \left(\frac{r}{x} \right)^n P_n(\cos\theta) - \sum_{n=0}^{3} \frac{1}{x} \left(\frac{r}{x} \right)^n P_n(\cos\theta) \right] \mathrm{d}x,$$

where

$$q_{\mathrm{L2}}(x) = \frac{\delta_2 q}{a} \left(\frac{x}{r_{\mathrm{K}}}\right)^{\sigma_2}, \qquad r_{\mathrm{K}} \leq x. \tag{2.36}$$

Then, applying the identity (Expansion (2.30) with $r_{\mathrm{s}} = x$, $q = 1$ and $\epsilon_{\mathrm{i}} = 1$)

$$\frac{1}{|\mathbf{r} - \mathbf{x}|} = \sum_{n=0}^{\infty} \frac{1}{x} \left(\frac{r}{x}\right)^n P_n(\cos\theta), \qquad r < x,$$

and noting that

$$\int_{r_{\mathrm{K}}}^{\infty} \frac{q_{\mathrm{L2}}(x)}{\epsilon_{\mathrm{i}}} \frac{1}{x} \left(\frac{r}{x}\right)^n P_n(\cos\theta)\mathrm{d}x = \frac{\delta_2 q}{\epsilon_{\mathrm{i}} a(n - \sigma_2)} \left(\frac{r}{r_{\mathrm{K}}}\right)^n P_n(\cos\theta), \quad 1 \leq n \leq 3,$$

we obtain

$$S_3 = \int_{r_{\mathrm{K}}}^{\infty} \frac{q_{\mathrm{L2}}(x)}{\epsilon_{\mathrm{i}}} \left(\frac{1}{|\mathbf{r} - \mathbf{x}|} - \frac{1}{x}\right) \mathrm{d}x - \frac{\delta_2 q}{\epsilon_{\mathrm{i}} a} \sum_{n=1}^{3} \frac{1}{n - \sigma_2} \left(\frac{r}{r_{\mathrm{K}}}\right)^n P_n(\cos\theta). \tag{2.37}$$

Similarly, we can obtain

$$S_4 = \int_{r_{\mathrm{K}}}^{\infty} \frac{q_{\mathrm{L3}}(x)}{\epsilon_{\mathrm{i}}} \left(\frac{1}{|\mathbf{r} - \mathbf{x}|} - \frac{1}{x} - \frac{r}{x^2} \cos\theta\right) \mathrm{d}x - \frac{\delta_3 q}{\epsilon_{\mathrm{i}} a} \sum_{n=2}^{3} \frac{1}{n - \sigma_3} \left(\frac{r}{r_{\mathrm{K}}}\right)^n P_n(\cos\theta),$$
$$\tag{2.38}$$

where

$$q_{\mathrm{L3}}(x) = \frac{\delta_3 q}{a} \left(\frac{x}{r_{\mathrm{K}}}\right)^{\sigma_3}, \qquad r_{\mathrm{K}} \leq x. \tag{2.39}$$

Finally, inserting (2.31), (2.34), (2.37) and (2.38) into (2.29) and then combining like

terms, we have the sixth-order line image approximation to the ionic solvent induced

reaction potential

$$\Phi_{\mathrm{RF}}(\mathbf{r}) = \frac{q_{\mathrm{K}}}{\epsilon_{\mathrm{i}}|\mathbf{r} - \mathbf{r}_{\mathrm{K}}|} + \int_{r_{\mathrm{K}}}^{\infty} \frac{q_{\mathrm{L1}}(x)}{\epsilon_{\mathrm{i}}|\mathbf{r} - \mathbf{x}|}\mathrm{d}x + \int_{r_{\mathrm{K}}}^{\infty} \frac{q_{\mathrm{L2}}(x)}{\epsilon_{\mathrm{i}}} \left(\frac{1}{|\mathbf{r} - \mathbf{x}|} - \frac{1}{x} \right) \mathrm{d}x$$

$$+ \int_{r_{\mathrm{K}}}^{\infty} \frac{q_{\mathrm{L3}}(x)}{\epsilon_{\mathrm{i}}} \left(\frac{1}{|\mathbf{r} - \mathbf{x}|} - \frac{1}{x} - \frac{r}{x^2} \cos\theta \right) \mathrm{d}x$$

$$+ \Phi_{\mathrm{C0}} + \Phi_{\mathrm{C1}}(\mathbf{r}) + \Phi_{\mathrm{C2}}(\mathbf{r}) + \Phi_{\mathrm{C3}}(\mathbf{r}) + O(u^6), \tag{2.40}$$

where Φ_{C0} is a *position-independent* correction potential defined as

$$\Phi_{\mathrm{C0}} = \frac{q}{\epsilon_{\mathrm{i}}a} \left(C_0(u) - \gamma - \frac{\delta_1}{\sigma_1} \right), \tag{2.41}$$

and on the other hand, $\Phi_{\mathrm{C1}}(\mathbf{r})$, $\Phi_{\mathrm{C2}}(\mathbf{r})$, and $\Phi_{\mathrm{C3}}(\mathbf{r})$ are *position-dependent* correction potentials given by

$$\Phi_{\mathrm{C1}}(\mathbf{r}) = \frac{q}{\epsilon_{\mathrm{i}}a} \left(C_1(u) - \gamma - \frac{\delta_1}{1 + \sigma_1} - \frac{\delta_2}{1 - \sigma_2} \right) \left(\frac{r}{r_{\mathrm{K}}} \right) \cos\theta,$$

$$\Phi_{\mathrm{C2}}(\mathbf{r}) = \frac{q}{\epsilon_{\mathrm{i}}a} \left(C_2(u) - \gamma - \frac{\delta_1}{2 + \sigma_1} - \frac{\delta_2}{2 - \sigma_2} - \frac{\delta_3}{2 - \sigma_3} \right) \left(\frac{r}{r_{\mathrm{K}}} \right)^2 P_2(\cos\theta),$$

$$\Phi_{\mathrm{C3}}(\mathbf{r}) = \frac{q}{\epsilon_{\mathrm{i}}a} \left(C_3(u) - \gamma - \frac{\delta_1}{3 + \sigma_1} - \frac{\delta_2}{3 - \sigma_2} - \frac{\delta_3}{3 - \sigma_3} \right) \left(\frac{r}{r_{\mathrm{K}}} \right)^3 P_3(\cos\theta).$$

For convenience, in terms of the Kronecker delta δ_{1n} we define

$$c_n = \frac{1}{\epsilon_{\mathrm{i}}a} \left(C_n(u) - \gamma - \frac{\delta_1}{n + \sigma_1} - \frac{\delta_2}{n - \sigma_2} - \frac{(1 - \delta_{1n})\delta_3}{n - \sigma_3} \right), \quad n = 1, 2, 3.$$

Then, we have

$$\Phi_{\mathrm{C}n}(\mathbf{r}) = q c_n \left(\frac{r}{r_{\mathrm{K}}} \right)^n P_n(\cos\theta), \quad n = 1, 2, 3. \tag{2.42}$$

2.2.4   Point image approximations to the reaction field

In this section, we will discuss how to approximate each line image charge involved in the image approximation in the previous section by a set of point image charges. Without loss of generality, we consider

$$I = \int_{r_{\mathrm{K}}}^{\infty} f(x) \left(\frac{x}{r_{\mathrm{K}}}\right)^{-\sigma} \mathrm{d}x, \tag{2.43}$$

where $\sigma > 0$. First, by introducing the change of variables $r_{\mathrm{K}}/x = ((1-s)/2)^{\tau}$ with $\tau > 0$, we have

$$I = 2^{-\tau\sigma}\tau \int_{-1}^{1} (1-s)^{\alpha} h(s,\tau)\mathrm{d}s, \tag{2.44}$$

where $\alpha = \tau\sigma - 1$ and

$$h(s,\tau) = \frac{2^{\tau}r_{\mathrm{K}}}{(1-s)^{\tau}} \, f\left(\frac{2^{\tau}r_{\mathrm{K}}}{(1-s)^{\tau}}\right). \tag{2.45}$$

Next, a numerical quadrature will be employed to approximate the integral in (2.44). Although in principle any numerical quadrature can be used, considering that $s = -1$ corresponds to the Kelvin image point $x = r_{\mathrm{K}}$ and that $\alpha > -1$ because $\sigma > 0$ and $\tau > 0$, the Jacobi-Gauss-Radau quadrature is particularly used in this paper. More precisely, let $s_m, \omega_m, m = 1, 2, \cdots, M$, be the Jacobi-Gauss-Radau points and weights on the interval $[-1, 1]$ with $\alpha = \tau\sigma - 1$ and $\beta = 0$, which can be obtained with the program ORTHPOL [17]. Then, the numerical quadrature for the integral in (2.44) is

$$I = \int_{r_{\mathrm{K}}}^{\infty} f(x) \left(\frac{x}{r_{\mathrm{K}}}\right)^{-\sigma} \mathrm{d}x \approx 2^{-\tau\sigma}\tau \sum_{m=1}^{M} \omega_m x_m f(x_m) \tag{2.46}$$

where for $m = 1, 2, \cdots, M$,

$$x_m = r_{\mathrm{K}} \left(\frac{2}{1-s_m}\right)^{\tau}. \tag{2.47}$$

The parameter $\tau > 0$ in the change of variables $r_{\mathrm{K}}/x = ((1-s)/2)^{\tau}$ can be used as a parameter to control the accuracy of numerical approximations. When $\tau = 1/\sigma$ we have $\alpha = 0$, and in this case the quadrature given by (2.46) simply reduces to the usual Gauss-Radau quadrature.

2.2.5 Discretization by point image charges at different locations

Note that

$$\frac{q_{\mathrm{L1}}(x)}{\epsilon_{\mathrm{i}}|\mathbf{r} - \mathbf{x}|} = \frac{\delta_1 q}{\epsilon_{\mathrm{i}} a |\mathbf{r} - \mathbf{x}|} \left(\frac{x}{r_{\mathrm{K}}}\right)^{-\sigma_1}.$$

Recall that $0 < \sigma_1 < 1$. Then using (2.46) with $\sigma = \sigma_1$ leads to

$$\int_{r_{\mathrm{K}}}^{\infty} \frac{q_{\mathrm{L1}}(x)}{\epsilon_{\mathrm{i}}|\mathbf{r} - \mathbf{x}|} \mathrm{d}x \approx \sum_{m=1}^{M} \frac{q_m^{\mathrm{L1}}}{\epsilon_{\mathrm{i}}|\mathbf{r} - \mathbf{x}_m^{\mathrm{L1}}|}, \tag{2.48}$$

where for $m = 1, 2, \cdots, M$,

$$q_m^{\mathrm{L1}} = 2^{-\tau\sigma_1} \tau \delta_1 \omega_m^{\mathrm{L1}} \frac{x_m^{\mathrm{L1}}}{a} q, \quad x_m^{\mathrm{L1}} = r_{\mathrm{K}} \left(\frac{2}{1 - s_m^{\mathrm{L1}}}\right)^{\tau}. \tag{2.49}$$

Here s_m^{L1} and ω_m^{L1} are the quadrature points and weights with $\alpha = \tau\sigma_1 - 1$.

Similarly, note that

$$\frac{q_{\mathrm{L2}}(x)}{\epsilon_{\mathrm{i}}} \left(\frac{1}{|\mathbf{r} - \mathbf{x}|} - \frac{1}{x}\right) = \frac{\delta_2 q}{\epsilon_{\mathrm{i}} a} \left(\frac{1}{|\mathbf{r} - \mathbf{x}|} - \frac{1}{x}\right) \left(\frac{x}{r_{\mathrm{K}}}\right) \left(\frac{x}{r_{\mathrm{K}}}\right)^{-(1-\sigma_2)}.$$

Recall that $0 < \sigma_2 < 1$. Then, applying (2.46) with $\sigma = (1 - \sigma_2) > 0$, we get

$$\int_{r_{\mathrm{K}}}^{\infty} \frac{q_{\mathrm{L2}}(x)}{\epsilon_{\mathrm{i}}} \left(\frac{1}{|\mathbf{r} - \mathbf{x}|} - \frac{1}{x}\right) \mathrm{d}x \approx \sum_{m=1}^{M} \frac{q_m^{\mathrm{L2}}}{\epsilon_{\mathrm{i}}|\mathbf{r} - \mathbf{x}_m^{\mathrm{L2}}|} - \sum_{m=1}^{M} \frac{q_m^{\mathrm{L2}}}{\epsilon_{\mathrm{i}} x_m^{\mathrm{L2}}}, \tag{2.50}$$

where for $m = 1, 2, \cdots, M$,

$$q_m^{\mathrm{L2}} = 2^{-\tau(1-\sigma_2)} \tau \delta_2 \omega_m^{\mathrm{L2}} \left(\frac{x_m^{\mathrm{L2}}}{r_{\mathrm{K}}}\right) \frac{x_m^{\mathrm{L2}}}{a} q, \quad x_m^{\mathrm{L2}} = r_{\mathrm{K}} \left(\frac{2}{1 - s_m^{\mathrm{L2}}}\right)^{\tau}. \tag{2.51}$$

Here s_m^{L2} and ω_m^{L2} are the quadrature points and weights with $\alpha = \tau(1 - \sigma_2) - 1$.

Also, it can be noted that

$$\frac{q_{\mathrm{L3}}(x)}{\epsilon_{\mathrm{i}}}\left(\frac{1}{|\mathbf{r} - \mathbf{x}|} - \frac{1}{x} - \frac{r}{x^2}\cos\theta\right) = \frac{\delta_3 q}{\epsilon_{\mathrm{i}} a}\left(\frac{1}{|\mathbf{r} - \mathbf{x}|} - \frac{1}{x} - \frac{r}{x^2}\cos\theta\right)\left(\frac{x}{r_{\mathrm{K}}}\right)^2\left(\frac{x}{r_{\mathrm{K}}}\right)^{-(2-\sigma_3)}.$$

Recalling that $1 < \sigma_3 < 2$, and applying (2.46) with $\sigma = (2 - \sigma_3) > 0$, we get

$$\int_{r_{\mathrm{K}}}^{\infty}\frac{q_{\mathrm{L3}}(x)}{\epsilon_{\mathrm{i}}}\left(\frac{1}{|\mathbf{r} - \mathbf{x}|} - \frac{1}{x} - \frac{r}{x^2}\cos\theta\right)\mathrm{d}x \approx \sum_{m=1}^{M}\frac{q_m^{\mathrm{L3}}}{\epsilon_{\mathrm{i}}|\mathbf{r} - \mathbf{x}_m^{\mathrm{L3}}|} - \sum_{m=1}^{M}\frac{q_m^{\mathrm{L3}}}{\epsilon_{\mathrm{i}}x_m^{\mathrm{L3}}} - \sum_{m=1}^{M}\frac{q_m^{\mathrm{L3}}r\cos\theta}{\epsilon_{\mathrm{i}}\left(x_m^{\mathrm{L3}}\right)^2},$$

$$(2.52)$$

where for $m = 1, 2, \cdots, M$,

$$q_m^{\mathrm{L3}} = 2^{-\tau(2-\sigma_3)}\tau\delta_3\omega_m^{\mathrm{L3}}\left(\frac{x_m^{\mathrm{L3}}}{r_{\mathrm{K}}}\right)^2\frac{x_m^{\mathrm{L3}}}{a}q, \quad x_m^{\mathrm{L3}} = r_{\mathrm{K}}\left(\frac{2}{1 - s_m^{\mathrm{L3}}}\right)^{\tau}. \qquad (2.53)$$

Here s_m^{L3} and ω_m^{L3} are the quadrature points and weights with $\alpha = \tau(2 - \sigma_3) - 1$.

Note that the second summation in the right-hand side of (2.50) and that in the right-hand side of (2.52) are position-independent. Adding them to Φ_{C0} leaves us with a modified position-independent correction potential

$$\bar{\Phi}_{\mathrm{C0}} = \Phi_{\mathrm{C0}} - \sum_{m=1}^{M}\frac{q_m^{\mathrm{L2}}}{\epsilon_{\mathrm{i}}x_m^{\mathrm{L2}}} - \sum_{m=1}^{M}\frac{q_m^{\mathrm{L3}}}{\epsilon_{\mathrm{i}}x_m^{\mathrm{L3}}}. \qquad (2.54)$$

Likewise, adding the last summation in the right-hand side of (2.52) to $\Phi_{\mathrm{C1}}(\mathbf{r})$ gives us a modified position-dependent correction potential

$$\bar{\Phi}_{\mathrm{C1}}(\mathbf{r}) = \Phi_{\mathrm{C1}}(\mathbf{r}) - \sum_{m=1}^{M}\frac{q_m^{\mathrm{L3}}r\cos\theta}{\epsilon_{\mathrm{i}}\left(x_m^{\mathrm{L3}}\right)^2} = q\bar{c}_1\left(\frac{r}{r_{\mathrm{K}}}\right)\cos\theta, \qquad (2.55)$$

where

$$\bar{c}_1 = c_1 - \frac{1}{\epsilon_{\mathrm{i}}a}\sum_{m=1}^{M}2^{-\tau(2-\sigma_3)}\tau\delta_3\omega_m^{\mathrm{L3}}\left(\frac{2}{1 - s_m^{\mathrm{L3}}}\right)^{\tau}.$$

2.2.6   Discretization by point image charges at the same locations

For computational efficiency, we can choose to discretize the three line image charges $q_{L1}(x)$, $q_{L2}(x)$ and $q_{L3}(x)$ by point charges at the same locations. More specifically, one can choose a common parameter $\sigma_c > 0$ to rewrite the line charge $q_{L1}(x)$ as

$$q_{L1}(x) = \frac{\delta_1 q}{a} \left(\frac{x}{r_K} \right)^{\sigma_c - \sigma_1} \left(\frac{x}{r_K} \right)^{-\sigma_c}.$$

Then, for $m=1, 2, \cdots, M$, we have

$$q_m^{L1} = 2^{-\tau\sigma_c}\tau\delta_1\omega_m \left(\frac{x_m}{r_K} \right)^{\sigma_c - \sigma_1} \frac{x_m}{a} q. \tag{2.56}$$

Here the quadrature points and weights are obtained using $\alpha = \tau\sigma_c - 1$.

Similarly, the line image charges $q_{L2}(x)$ and $q_{L3}(x)$ are discretized into

$$q_m^{L2} = 2^{-\tau\sigma_c}\tau\delta_2\omega_m \left(\frac{x_m}{r_K} \right)^{\sigma_c + \sigma_2} \frac{x_m}{a} q, \tag{2.57}$$

$$q_m^{L3} = 2^{-\tau\sigma_c}\tau\delta_3\omega_m \left(\frac{x_m}{r_K} \right)^{\sigma_c + \sigma_3} \frac{x_m}{a} q. \tag{2.58}$$

The parameter $\sigma_c > 0$ is tunable for optimal computational efficiency. For example, depending on the value of $u = \lambda a$, any of the three natural choices $\sigma_c = \sigma_1$, $\sigma_c = 1 - \sigma_2$ or $\sigma_c = 2 - \sigma_3$ could perform well.

Furthermore, since $s_1 = -1$ and consequently $x_1 = r_K$, the classical Kelvin image charge and the first discrete image charge of each image line charge can be combined. In conclusion, in general we have the following multiple discrete image approximation to the reaction potential inside the sphere in terms of the potentials of $3M - 2$ point charges (or

M charges if a common parameter σ_c is utilized) and some correction potentials.

$$
\begin{aligned}
\Phi_{\mathrm{RF}}(\mathbf{r}) \quad &\approx \quad \frac{1}{\epsilon_\mathrm{i}} \left[\frac{q'_\mathrm{K}}{|\mathbf{r} - \mathbf{r}_\mathrm{K}|} + \sum_{m=2}^{M} \left(\frac{q_m^{\mathrm{L1}}}{|\mathbf{r} - \mathbf{x}_m^{\mathrm{L1}}|} + \frac{q_m^{\mathrm{L2}}}{|\mathbf{r} - \mathbf{x}_m^{\mathrm{L2}}|} + \frac{q_m^{\mathrm{L3}}}{|\mathbf{r} - \mathbf{x}_m^{\mathrm{L3}}|} \right) \right] \\
&\quad + \bar{\Phi}_{\mathrm{C0}} + \bar{\Phi}_{\mathrm{C1}}(\mathbf{r}) + \Phi_{\mathrm{C2}}(\mathbf{r}) + \Phi_{\mathrm{C3}}(\mathbf{r}),
\end{aligned} \tag{2.59}
$$

where

$$
q'_\mathrm{K} = q_\mathrm{K} + q_1^{\mathrm{L1}} + q_1^{\mathrm{L2}} + q_1^{\mathrm{L3}}.
$$

For the sake of convenience, we simply write (2.59) as

$$
\Phi_{\mathrm{RF}}(\mathbf{r}) \approx \sum_{m=1}^{N_{\mathrm{im}}} \frac{q_m^{\mathrm{Im}}}{\epsilon_\mathrm{i} |\mathbf{r} - \mathbf{x}_m|} + \bar{\Phi}_{\mathrm{C0}} + \bar{\Phi}_{\mathrm{C1}}(\mathbf{r}) + \Phi_{\mathrm{C2}}(\mathbf{r}) + \Phi_{\mathrm{C3}}(\mathbf{r}), \tag{2.60}
$$

where the summation over m includes the modified Kelvin image charge q'_K at the corresponding Kelvin image point $\mathbf{r}_\mathrm{K}$ and all discrete image point charges q_m^{L1}, q_m^{L2}, and q_m^{L3} at $\mathbf{x}_m^{\mathrm{L1}}$, $\mathbf{x}_m^{\mathrm{L2}}$, and $\mathbf{x}_m^{\mathrm{L3}}$, respectively, and N_{im} is the total number of all point image charges.

2.3 $O(N)$ implementation of the point image approximation

The main purpose for the discrete image approximation to the reaction field is to enable us to apply existing fast algorithms, such as the pre-corrected FFT [37] or the fast multipole method (FMM) [7, 8, 20–22], directly in calculating the electrostatic interactions among N source point charges inside the spherical cavity in $O(N \log N)$ or even $O(N)$ operations. In particular, below we give a straightforward $O(N)$ implementation of the discrete image approximation with using the FMM.

For convenience, let $\mathbf{r}_i^\mathrm{F} = (x_i^\mathrm{F}, y_i^\mathrm{F}, z_i^\mathrm{F})$, $i = 1, 2, \cdots, N$, be N observation points and $\mathbf{r}_j^\mathrm{S} = (x_j^\mathrm{S}, y_j^\mathrm{S}, z_j^\mathrm{S})$, $j = 1, 2, \cdots, N$, be the locations of N source charges with charge

strengths $q_1, q_2, \cdots, q_N$. By linear superposition, the reaction field at an observation point $\mathbf{r}_i^{\mathrm{F}}$, in the case that the sixth-order image approximation (2.60) is employed, becomes

$$\Phi_{\mathrm{RF}}(\mathbf{r}_i^{\mathrm{F}}) \approx \sum_{j=1}^{N} \sum_{m=1}^{N_{\mathrm{im}}} \frac{q_{m,j}^{\mathrm{Im}}}{\epsilon_{\mathrm{i}} |\mathbf{r}_i^{\mathrm{F}} - \mathbf{x}_{m,j}|} + \sum_{j=1}^{N} \left(\bar{\Phi}_{\mathrm{C0},j} + \bar{\Phi}_{\mathrm{C1},j}(\mathbf{r}_i^{\mathrm{F}}) + \Phi_{\mathrm{C2},j}(\mathbf{r}_i^{\mathrm{F}}) + \Phi_{\mathrm{C3},j}(\mathbf{r}_i^{\mathrm{F}}) \right).$$

$$(2.61)$$

Here and in the sequel a quantity with a second subscript j designates a quantity associated with the source charge $\mathbf{r}_j^{\mathrm{S}}$, such as

$$r_{\mathrm{K},j} = \frac{a^2}{r_j^{\mathrm{S}}}, \qquad x_{m,j} = r_{\mathrm{K},j} \left(\frac{2}{1 - s_m} \right)^{\tau}.$$

2.3.1 $O(N)$ calculation of the correction potentials

Obviously, the *position-independent* correction potential

$$\sum_{j=1}^{N} \bar{\Phi}_{\mathrm{C0},j} = \sum_{j=1}^{N} \left[\frac{q_j}{\epsilon_{\mathrm{i}} a} \left(C_0(u) - \gamma - \frac{\delta_1}{\sigma_1} \right) - \sum_{m=1}^{M} \frac{q_{m,j}^{\mathrm{L2}}}{\epsilon_{\mathrm{i}} x_{m,j}^{\mathrm{L2}}} - \sum_{m=1}^{M} \frac{q_{m,j}^{\mathrm{L3}}}{\epsilon_{\mathrm{i}} x_{m,j}^{\mathrm{L3}}} \right]$$

can be evaluated in $O(N)$ operations. The evaluation of other correction potentials in $O(N)$ operations, however, needs some manipulations due to their position-dependence. First of all, from (2.55) we have

$$\sum_{j=1}^{N} \bar{\Phi}_{\mathrm{C1},j}(\mathbf{r}_i^{\mathrm{F}}) = \left(\frac{\bar{c}_1}{a^2} \sum_{j=1}^{N} q_j \mathbf{r}_j^{\mathrm{S}} \right) \bullet \mathbf{r}_i^{\mathrm{F}}, \tag{2.62}$$

which in component form can be written as

$$\sum_{j=1}^{N} \bar{\Phi}_{\mathrm{C1},j}(\mathbf{r}_i^{\mathrm{F}}) = d_1 x_i^{\mathrm{F}} + d_2 y_i^{\mathrm{F}} + d_3 z_i^{\mathrm{F}}, \tag{2.63}$$

where

$$d_1 = \frac{\bar{c}_1}{a^2} \sum_{j=1}^{N} q_j x_j^{\mathrm{S}}, \quad d_2 = \frac{\bar{c}_1}{a^2} \sum_{j=1}^{N} q_j y_j^{\mathrm{S}}, \quad d_3 = \frac{\bar{c}_1}{a^2} \sum_{j=1}^{N} q_j z_j^{\mathrm{S}}.$$

Now it becomes clear that the second correction potential can be evaluated in $O(N)$ operations as well. Analogously, the third correction potential can also be evaluated in $O(N)$ operations. In fact, from (2.42) we have

$$\sum_{j=1}^{N} \Phi_{\text{C2},j}(\mathbf{r}_i^{\text{F}}) = \frac{3c_2}{2a^4} \sum_{j=1}^{N} q_j \left(\mathbf{r}_j^{\text{S}} \bullet \mathbf{r}_i^{\text{F}}\right)^2 - \left(\frac{c_2}{2a^4} \sum_{j=1}^{N} q_j \left(r_j^{\text{S}}\right)^2\right) \left(r_i^{\text{F}}\right)^2,$$

which can be written as

$$\sum_{j=1}^{N} \Phi_{\text{C2},j}(\mathbf{r}_i^{\text{F}}) = e_0 \left(r_i^{\text{F}}\right)^2 + \left(M\mathbf{r}_i^{\text{F}}\right) \bullet \mathbf{r}_i^{\text{F}}, \tag{2.64}$$

where

$$e_0 = -\frac{c_2}{2a^4} \sum_{j=1}^{N} q_j \left(r_j^{\text{S}}\right)^2, \quad M = \frac{3c_2}{2a^4} \sum_{j=1}^{N} q_j \mathbf{r}_j^{\text{S}} \otimes \mathbf{r}_j^{\text{S}},$$

and $\otimes$ represents the outer product of two vectors.

In component form, (2.64) can be written as

$$\sum_{j=1}^{N} \Phi_{\text{C2},j}(\mathbf{r}_i^{\text{F}}) = e_0 \left(r_i^{\text{F}}\right)^2 + e_1 \left(x_i^{\text{F}}\right)^2 + e_2 \left(y_i^{\text{F}}\right)^2 + e_3 \left(z_i^{\text{F}}\right)^2$$

$$+ e_4 x_i^{\text{F}} y_i^{\text{F}} + e_5 x_i^{\text{F}} z_i^{\text{F}} + e_6 y_i^{\text{F}} z_i^{\text{F}}, \tag{2.65}$$

where

$$e_1 = \frac{3c_2}{2a^4} \sum_{j=1}^{N} q_j \left(x_j^{\text{S}}\right)^2, \quad e_2 = \frac{3c_2}{2a^4} \sum_{j=1}^{N} q_j \left(y_j^{\text{S}}\right)^2, \quad e_3 = \frac{3c_2}{2a^4} \sum_{j=1}^{N} q_j \left(z_j^{\text{S}}\right)^2,$$

$$e_4 = \frac{3c_2}{a^4} \sum_{j=1}^{N} q_j x_j^{\text{S}} y_j^{\text{S}}, \quad e_5 = \frac{3c_2}{a^4} \sum_{j=1}^{N} q_j x_j^{\text{S}} z_j^{\text{S}}, \quad e_6 = \frac{3c_2}{a^4} \sum_{j=1}^{N} q_j y_j^{\text{S}} z_j^{\text{S}}.$$

Similarly, the fourth correction potential can be evaluated in $O(N)$ operations as well. By expressing the cosine of the angle θ between $\mathbf{r}_i^{\text{F}}$ and $\mathbf{r}_j^{\text{S}}$ in terms of their rectangular

coordinates, from (2.42) one can arrive at

$$
\sum_{j=1}^{N} \Phi_{\mathrm{C3},j}(\mathbf{r}_i^{\mathrm{F}}) = f_1 \left(x_i^{\mathrm{F}}\right)^3 + f_2 \left(y_i^{\mathrm{F}}\right)^3 + f_3 \left(z_i^{\mathrm{F}}\right)^3 + f_4 \left(x_i^{\mathrm{F}}\right)^2 y_i^{\mathrm{F}} + f_5 \left(x_i^{\mathrm{F}}\right)^2 z_i^{\mathrm{F}}
$$

$$
+ f_6 x_i^{\mathrm{F}} \left(y_i^{\mathrm{F}}\right)^2 + f_7 \left(y_i^{\mathrm{F}}\right)^2 z_i^{\mathrm{F}} + f_8 x_i^{\mathrm{F}} \left(z_i^{\mathrm{F}}\right)^2 + f_9 y_i^{\mathrm{F}} \left(z_i^{\mathrm{F}}\right)^2
$$

$$
+ f_{10} x_i^{\mathrm{F}} y_i^{\mathrm{F}} z_i^{\mathrm{F}} + f_{11} x_i^{\mathrm{F}} \left(r_i^{\mathrm{F}}\right)^2 + f_{12} y_i^{\mathrm{F}} \left(r_i^{\mathrm{F}}\right)^2 + f_{13} z_i^{\mathrm{F}} \left(r_i^{\mathrm{F}}\right)^2, \qquad (2.66)
$$

where

$$
f_1 = \frac{5c_3}{2a^6} \sum_{j=1}^{N} q_j \left(x_j^{\mathrm{S}}\right)^3, \ \ f_2 = \frac{5c_3}{2a^6} \sum_{j=1}^{N} q_j \left(y_j^{\mathrm{S}}\right)^3, \ \ f_3 = \frac{5c_3}{2a^6} \sum_{j=1}^{N} q_j \left(z_j^{\mathrm{S}}\right)^3,
$$

$$
f_4 = \frac{15c_3}{2a^6} \sum_{j=1}^{N} q_j \left(x_j^{\mathrm{S}}\right)^2 y_j^{\mathrm{S}}, \ \ f_5 = \frac{15c_3}{2a^6} \sum_{j=1}^{N} q_j \left(x_j^{\mathrm{S}}\right)^2 z_j^{\mathrm{S}}, \ \ f_6 = \frac{15c_3}{2a^6} \sum_{j=1}^{N} q_j x_j^{\mathrm{S}} \left(y_j^{\mathrm{S}}\right)^2,
$$

$$
f_7 = \frac{15c_3}{2a^6} \sum_{j=1}^{N} q_j \left(y_j^{\mathrm{S}}\right)^2 z_j^{\mathrm{S}}, \ \ f_8 = \frac{15c_3}{2a^6} \sum_{j=1}^{N} q_j x_j^{\mathrm{S}} \left(z_j^{\mathrm{S}}\right)^2, \ \ f_9 = \frac{15c_3}{2a^6} \sum_{j=1}^{N} q_j y_j^{\mathrm{S}} \left(z_j^{\mathrm{S}}\right)^2,
$$

$$
f_{10} = \frac{15c_3}{a^6} \sum_{j=1}^{N} q_j x_j^{\mathrm{S}} y_j^{\mathrm{S}} z_j^{\mathrm{S}}, \ \ f_{11} = -\frac{3c_3}{2a^6} \sum_{j=1}^{N} q_j x_j^{\mathrm{S}} \left(r_j^{\mathrm{S}}\right)^2,
$$

$$
f_{12} = -\frac{3c_3}{2a^6} \sum_{j=1}^{N} q_j y_j^{\mathrm{S}} \left(r_j^{\mathrm{S}}\right)^2, \ \ f_{13} = -\frac{3c_3}{2a^6} \sum_{j=1}^{N} q_j z_j^{\mathrm{S}} \left(r_j^{\mathrm{S}}\right)^2.
$$

2.3.2 $O(N)$ calculation of the potentials of the image charges

The FMM is known to be extremely efficient in the evaluation of pairwise interactions in large ensembles of particles, such as that included in (2.61)

$$
\sum_{j=1}^{N} \sum_{m=1}^{N_{\mathrm{im}}} \frac{q_{m,j}^{\mathrm{Im}}}{\epsilon_i |\mathbf{r}_i^{\mathrm{F}} - \mathbf{x}_{m,j}|}, \qquad i = 1, 2, \cdots, N.
$$

For instance, the adaptive FMM of [8] requires $O(N)$ work and breaks even with the direct calculation at about $N{=}750$ for three-digit precision, $N{=}1500$ for six-digit precision, and $N{=}2500$ for nine-digit precision, respectively [23]. Using such an adaptive FMM with

$O(N)$ computational complexity, the calculation of the potentials of the discrete image charges for all observation points can be evaluated in $O(N)$ operations in a straightforward way.

In the simplest implementation, such evaluation can be carried out with a single FMM run by including all point image charges $q_{m,j}^{\text{Im}}$ into the FMM cube. In the case that the total potential is to be calculated, all original source charges are also included in the FMM box. All charges are taken as acting in a homogeneous medium of the dielectric constant ϵ_i.

2.3.3   Local expansions for potential calculations

The introduced discrete image charges outside the sphere will result in a large computational domain and the image charges are highly nonuniformly distributed, particularly because the image charges of those source charges close to the center of the sphere are far away from the spherical boundary. Therefore, direct application of the FMM by including all image charges in this large computational box is not efficient. Instead, a simple but more efficient way would be to calculate the local expansion due to the far field image charges directly inside the sphere. This way, one can achieve not only a smaller FMM box but also a smaller number of total charges in the FMM box.

More specifically, in practice we could introduce a bigger cut-off sphere of radius κa centered at the origin with $\kappa > 1$. The calculation of the potentials inside the original dielectric sphere due to those image charges inside this cut-off sphere is still carried out by the chosen fast method.   For all image charges outside this cut-off sphere at $(\rho_l, \alpha_l, \beta_l), l=1, 2 \cdots, L$, with charge strengths $\hat{q}_l, l=1, 2, \cdots, L$, the calculation of the potential at $\mathbf{r}=(r, \theta, \phi)$ inside the dielectric sphere generated by these image charges can

be described by a local expansion

$$\Phi(\mathbf{r}) \approx \sum_{j=0}^{p} \sum_{k=-j}^{j} L_j^k \cdot Y_j^k(\theta, \phi) \cdot r^j, \qquad (2.67)$$

where $Y_j^k(\theta, \phi)$ are the spherical harmonics, and L_j^k are the local expansion coefficients given by

$$L_j^k = \sum_{l=1}^{L} \hat{q}_l \cdot \frac{Y_j^{-k}(\alpha_l, \beta_l)}{\rho_l^{j+1}}. \qquad (2.68)$$

Furthermore, for any $p \geq 1$,

$$\left| \Phi(\mathbf{r}) - \sum_{j=0}^{p} \sum_{k=-j}^{j} L_j^k \cdot Y_j^k(\theta, \phi) \cdot r^j \right| \leq \left(\frac{\sum_{l=1}^{L} |\hat{q}_l|}{\kappa a - r} \right) \left(\frac{r}{\kappa a} \right)^{p+1}. \qquad (2.69)$$

2.3.4 $O(N)$ calculation of the force field

In practice, most time in molecular dynamics simulations the electric force field needs to be calculated. Although force equations are not difficult to derive, we would like to include them here for completeness.

In general, electric forces are computed by taking gradients of electric potentials. Therefore, the electric force exerted on Particle i at the position $\mathbf{r}_i^{\mathrm{F}}$ is expressed as

$$\mathbf{f}(\mathbf{r}_i^{\mathrm{F}}) = -q_i \nabla_{\mathbf{r}} \Phi(\mathbf{r}_i^{\mathrm{F}}).$$

In the case that the reaction potential field is approximated by the sixth-order image approximation (2.60), the image approximation for the electric force field becomes (note that $-\nabla_{\mathbf{r}} \bar{\Phi}_{\mathrm{C0},j} = 0$)

$$\mathbf{f}(\mathbf{r}_i^{\mathrm{F}}) = q_i \sum_{j=1}^{N} \sum_{m=1}^{N_{\mathrm{im}}} \frac{q_{m,j}^{\mathrm{Im}}(\mathbf{r}_i^{\mathrm{F}} - \mathbf{x}_{m,j})}{\epsilon_{\mathrm{i}} |\mathbf{r}_i^{\mathrm{F}} - \mathbf{x}_{m,j}|^3} - q_i \nabla_{\mathbf{r}} \sum_{j=1}^{N} \left(\bar{\Phi}_{\mathrm{C1},j}(\mathbf{r}_i^{\mathrm{F}}) + \Phi_{\mathrm{C2},j}(\mathbf{r}_i^{\mathrm{F}}) + \Phi_{\mathrm{C3},j}(\mathbf{r}_i^{\mathrm{F}}) \right).$$

First of all, $O(N)$ calculation of the gradients of the correction potentials can be derived directly from the $O(N)$ calculation of the corresponding correction potentials. For examples, from (2.62) and (2.64) we can obtain

$$-\nabla_{\mathbf{r}} \sum_{j=1}^{N} \bar{\Phi}_{\mathrm{C1},j}(\mathbf{r}_i^{\mathrm{F}}) = -\frac{\bar{c}_1}{a^2} \sum_{j=1}^{N} q_j \mathbf{r}_j^{\mathrm{S}},$$

and

$$-\nabla_{\mathbf{r}} \sum_{j=1}^{N} \Phi_{\mathrm{C2},j}(\mathbf{r}_i^{\mathrm{F}}) = -2(e_0 I + M)\mathbf{r}_i^{\mathrm{F}} = -\begin{pmatrix} 2(e_0 + e_1) & e_4 & e_5 \\ e_4 & 2(e_0 + e_2) & e_6 \\ e_5 & e_6 & 2(e_0 + e_3) \end{pmatrix} \mathbf{r}_i^{\mathrm{F}}.$$

On the other hand, the FMM can be used to calculate

$$q_i \sum_{j=1}^{N} \sum_{m=1}^{N_{\mathrm{im}}} \frac{q_{m,j}^{\mathrm{Im}}(\mathbf{r}_i^{\mathrm{F}} - \mathbf{x}_{m,j})}{\epsilon_i |\mathbf{r}_i^{\mathrm{F}} - \mathbf{x}_{m,j}|^3}, \quad i = 1, 2, \cdots, N$$

in $O(N)$ complexity.

Moreover, the force field inside the sphere due to the far field image charges can also be described in local expansions. Local expansion for force calculations in the FMM can be found in [14, 32]. When using the local expansion (2.67) to calculate the far-field electric potential due to all image charges outside the cut-off sphere, the corresponding far-field force $\mathbf{f}(\mathbf{r})$ exerted on a particle q at $\mathbf{r} = (r, \theta, \phi)$ inside the dielectric sphere can also be described by local expansions. Passing the details, we have

$$f_x(\mathbf{r}) = -q \frac{\partial}{\partial x} \Phi(\mathbf{r}) = -q \cdot \mathrm{Re}\,(H_2 - H_3), \qquad (2.70)$$

$$f_y(\mathbf{r}) = -q \frac{\partial}{\partial y} \Phi(\mathbf{r}) = -q \cdot \mathrm{Im}\,(H_2 + H_3), \qquad (2.71)$$

$$f_z(\mathbf{r}) = -q \frac{\partial}{\partial z} \Phi(\mathbf{r}) = -q \cdot (H_0 + 2\mathrm{Re}(H_1)), \qquad (2.72)$$

where $\mathrm{Re}(\ldots)$ and $\mathrm{Im}(\ldots)$ represent the real and the imaginary parts of a complex number, respectively, and

$$H_0 = \sum_{j=1}^{p} j L_j^0 P_{j-1}(\cos\theta) r^{j-1},$$

$$H_1 = \sum_{j=1}^{p} \sum_{k=1}^{j-1} (j+k) C_j^k \cdot L_j^k e^{ik\phi} P_{j-1}^k(\cos\theta) r^{j-1},$$

$$H_2 = \sum_{j=1}^{p} L_j^0 e^{i\phi} P_{j-1}^1(\cos\theta) r^{j-1} + \sum_{j=1}^{p} \sum_{k=1}^{j} C_j^k L_j^k e^{i(k+1)\phi} P_{j-1}^{k+1}(\cos\theta) r^{j-1},$$

$$H_3 = \sum_{j=1}^{p} C_j^{-1} L_j^1 P_{j-1}(\cos\theta) r^{j-1} + \sum_{j=1}^{p} \sum_{k=2}^{j} B_j^k C_j^k L_j^k e^{i(k-1)\phi} P_{j-1}^{k-1}(\cos\theta) r^{j-1},$$

and

$$B_j^k = (j+k)(j+k-1), \qquad C_j^k = \sqrt{\frac{(j-k)!}{(j+k)!}}.$$

2.4   Numerical examples

For illustration purpose, a unit dielectric sphere is used. The dielectric constants of the sphere and its surrounding medium are assumed to be $\epsilon_i=2$ (normally 1, 2 or 4) and $\epsilon_o=80$ (the dielectric constant of water), respectively. Unless otherwise specified, the results obtained by the direct series expansion with 400 terms are treated as the exact reaction fields to calculate the errors of the sixth-order image approximation.

2.4.1   Accuracy vs the ionic strength

We begin by considering a single point charge located on the x-axis inside the sphere at a distance $r_s=0.5$ or $r_s=0.95$ from the center of the sphere. Different σ values are used in discretizing the underlying image line charges, but for simplicity, we always choose $\tau=1/\sigma$ and $M=40$ so that the same Gauss-Radau quadrature points and weights s_m and

ω_m are involved. For each selected value of $u=\lambda a$, we calculate the relative error of the image approximation in the reaction field, respectively, at $10,000$ observation points uniformly distributed (under the polar coordinates) within the unit disk in the plane $y = 0$. The maximal relative error $\parallel E \parallel$ at these observation points for various u values and the corresponding order of convergence are shown in Tables 2.1 and 2.2. For sake of comparison, the results obtained using the improved fourth-order image approximation are also included. As can be observed, the results clearly demonstrate the $O(u^6)$ convergence rate of the sixth-order image approximation.

Table 2.1: Convergence rate of the proposed image approximation ($r_{\mathrm{s}} = 0.5$).

u	Impr. 4th-order		6th-order	
	$\parallel E \parallel$	Order	$\parallel E \parallel$	Order
0.8	2.13E-5		2.22E-7	
0.4	1.42E-6	3.91	3.46E-9	6.00
0.2	9.08E-8	3.97	5.61E-11	5.94
0.1	5.68E-9	4.00	4.20E-11	

Table 2.2: Convergence rate of the proposed image approximation ($r_{\mathrm{s}} = 0.95$).

u	Impr. 4th-order		6th-order	
	$\parallel E \parallel$	Order	$\parallel E \parallel$	Order
0.8	1.68e-4		3.25e-6	
0.4	1.12e-5	3.90	5.30e-8	5.94
0.2	7.20e-7	3.96	7.16e-10	6.21
0.1	4.64e-8	3.96	9.03e-11	

2.4.2   Accuracy vs the number of discrete image charges

One natural concern with the proposed discrete image approximation is the final number of point image charges required to achieve certain order of degree of accuracy. For a desired accuracy, this number depends on the locations of the source charge and the observation

point. It should be small if compared to the number of terms needed to achieve the same degree of accuracy in the direct series expansion to make the image approximation useful in practice.

In this test, the source location is fixed at $r_{\mathrm{s}} = 0.95$. For each selected value of $u = \lambda a$ ranging from 0.05 to 0.9, we approximate the reaction fields at the same 10,000 points within the sphere by the sixth-order image approximation with several different numbers of point image charges. Figure 2.2 shows the maximum relative errors of the point image approximation using $M = 2$, $M = 6$ and $M = 10$, without a common σ being used. For the sake of comparison, the corresponding error analysis results for the improved fourth-order image approximation are also plotted.

Figure 2.2: Maximum relative errors in the ionic solvent induced reaction field due to a source charge inside the unit sphere at distance $r_{\mathrm{s}} = 0.95$ from the spherical center. No common σ is used.

As can be seen, when $M = 2$, the sixth-order multiple discrete image approximation can achieve 10^{-3} accuracy. However, as M is small, the accuracy of the sixth-order image

approximation is no better than that of the improved fourth-order image approximation. This is because when M is small, the numerical error stemming from the approximation of the line image charges by point image charges dominates. Nevertheless, when M is relatively large, the advantage of the sixth-order image approximation becomes evident in the sense of accuracy. For example, as shown in Figure 2.2, the sixth-order image approximation is clearly shown to be more accurate than the fourth-order one when $M = 10$ is used, particularly for cases with large u values. It should be pointed out that, since different line images are discretized by point images at different locations, the number of total point images in the sixth-order method is $3M - 2$, while that in the fourth-order method is only $2M - 1$ in this particular test.

Similar error analysis results with a common σ being used are displayed in Figure 2.3. Note that in this case the sixth-order and the fourth-order methods both use M point images for a given M value. As shown in Figure 2.3, for low accuracy (such as 10^{-2}), for all u values in the range of $[0.05, 0.9]$, both the sixth-order and the fourth-order methods need 2 point images and thus the same computational cost to achieve the required accuracy. For high accuracy (such as 10^{-5}), on the one hand, when the u value is small, the two methods still have comparable performance, namely, they need to use the same number of point images to achieve the same accuracy. On the other hand, when the u value is large such as 0.9, the error of the sixth-order method using 10 point images can be less than 4×10^{-5}, but that of the fourth-order method using the same number of point images is around 2×10^{-4}, implying that if it is possible for the the fourth-order method to realize the same 4×10^{-5} accuracy, it must use more than 10 image charges and consequently more computational cost. Actually, as shown by Figure 2.4, the best accuracy the fourth-

order method can achieve is around 1.2×10^{-3} for $u = 0.9$ and 1.5×10^{-4} for $u = 0.5$, respectively. Therefore, when the u value is large, high-accuracy can only be accomplished by using the sixth-order method.
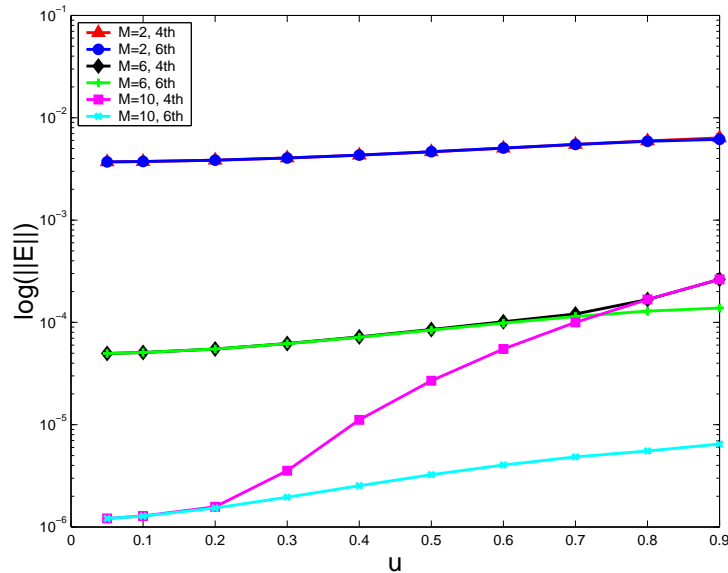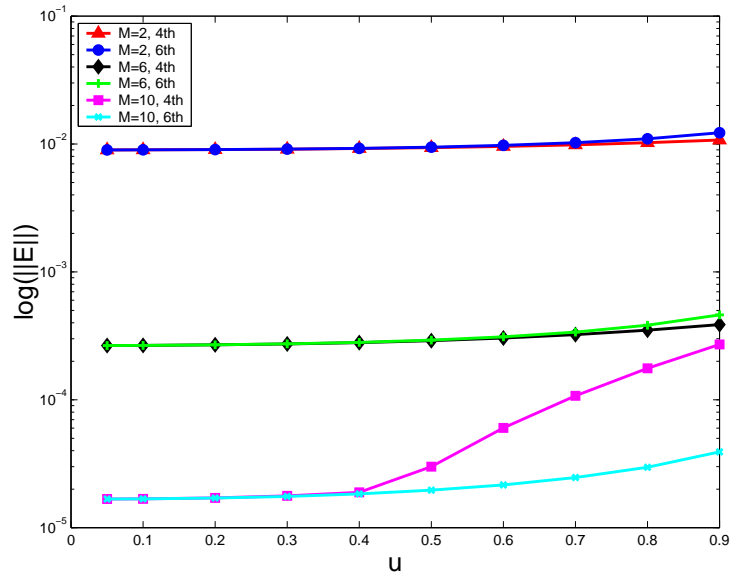

Figure 2.3: Maximum relative errors in the ionic solvent induced reaction field due to a source charge inside the unit sphere at distance $r_{\mathrm{S}} = 0.95$ from the spherical center. A common σ is used.

2.4.3 Computational complexity of the point image approximation

To demonstrate the $O(N)$ computational complexity of the $O(N)$ implementation of the point image approximation as described in Sections 2.3 and 2.3.4, the sixth-order image approximation has been implemented with using the free software *KIFMM*, developed by L. Ying using a so-called kernel-independent adaptive fast multipole method [40]. The experiments are carried out on a Linux-based Dell OptiPlex 745 workstation with a CPU clock rate of 3GHz and a memory of 4GB, using GNU Fortran 3.4.6 and C++ 4.1.2 compilers. In Tables 2.3 and 2.4, timing results of the potential and the force evaluations are reported and compared with those obtained without using the
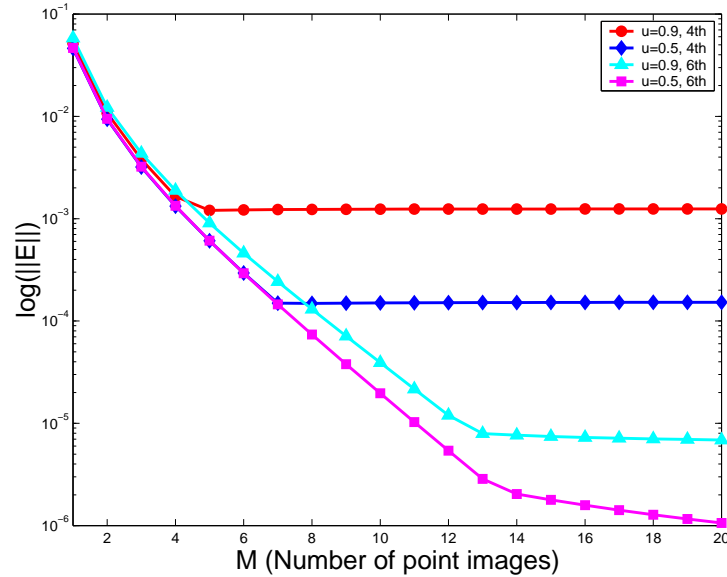
Figure 2.4: Maximum relative errors in the ionic solvent induced reaction field due to a source charge inside the unit sphere at distance $r_{\mathrm{s}} = 0.95$ from the spherical center. A common σ is used.

FMM. The Gauss-Radau quadrature with M=2 and a common parameter $\sigma_{\mathrm{c}}=\sigma_2$ are used to construct discrete image charges, so for each source charge, there are two discrete image charges. As can be seen, the timing scales as $O(N^2)$ without using the FMM, and linearly with using the FMM. In the tables, N denotes the number of total source charges, either uniformly or non-uniformly distributed inside the unit sphere, and NC the number of total point charges included in the FMM box, respectively.

Table 2.3: Timing results for potential calculation.

N	NC	FMM/uniform	FMM/non-uniform	Pairwise
1,000	3,000	0.175	0.173	0.134
2,000	6,000	0.329	0.325	0.535
4,000	12,000	0.751	0.745	2.144
8,000	24,000	1.435	1.355	8.564
16,000	48,000	2.701	2.665	34.274

Table 2.4: Timing results for force calculation.

N	NC	FMM/uniform	FMM/non-uniform	Pairwise
1,000	3,000	0.386	0.384	0.319
2,000	6,000	0.534	0.529	1.276
4,000	12,000	1.004	0.990	5.099
8,000	24,000	2.141	2.132	20.365
16,000	48,000	3.707	3.555	81.556

2.4.4   A simple application of the method

Finally, the proposed sixth-order method is tested through calculation of solvation effects. A spherical cavity of radius 15 Åcontains 333 TIP3P water molecules and is immersed in an ionic solvent. To calculate the total solvation energy of these water molecules, $\epsilon_i = 1$ and $\epsilon_o = 80$ are used in this test. Here the solvation energy of a collection of N charges q_i located at $\mathbf{r}_i$, $i = 1, 2, \cdots, N$, is defined as

$$U_{\text{sol}} = \frac{1}{2} \sum_{i=1}^{N} q_i \Phi_{\text{RF}}(\mathbf{r}_i).$$

Figure 2.5 shows the relative error in the solvation energy obtained with the the fourth-order and the sixth-order image approximations by using $M = 6$ and $M = 10$ point image charges, respectively, where the exact solvation energy is calculated by the series solution with 400 terms. As can be seen, the sixth-order accuracy of the present method has a noticeable effect on the solvation energy.
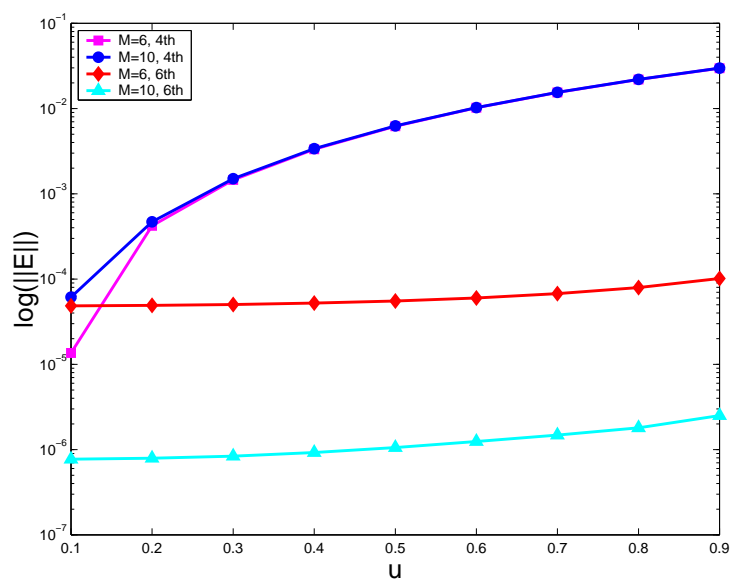
Figure 2.5: Relative error in the solvation energy calculation of water molecules in ionic solvents by two image approximation methods.

CHAPTER 3: AN IMAGE-BASED REACTION FIELD METHOD FOR
ELECTROSTATIC INTERACTIONS IN MOLECULAR DYNAMICS SIMULATION
OF IONIC SOLUTIONS

3.1   Theory of molecular dynamics simulation and Poisson-Boltzman equation

In Section 1.1, we introduced the Poisson equation as the one of the basic theories of

molecular dynamics (MD) simulation. In this section, we will discuss in detail its derivation

and applications to the MD simulation in this section, providing in-depth background to our

proposed simulation model.

3.1.1   Basics of molecular dynamics simulation

To discuss the molecular dynamic as well as PB equation in more detail and to give a

full derivation of the equation from a few assumptions, we first introduce the fundamental

problem of classical mechanics which is the *n-Body Problem* [27]:

Given n particles of mass m_i acted upon by forces $\mathbf{f}_i$ with initial particle

positions $\mathbf{r}_i(0) = (x_{i0}, y_{i0}, z_{i0})$ and velocities $\mathbf{v}_i(0) = \dot{\mathbf{r}}(0)$, describe the

positions of the particles, $\mathbf{r}_i(t)$, over time.

The function $\mathbf{r}_i(t) : \mathbb{R} \mapsto \mathbb{R}^3$ represents the motion of the ith particle over time, for $i =$

$1, 2, \ldots, n$. The configuration space of the n-particle system is simply the space $\mathbb{R}^N = \mathbb{R}^3 \times$

$\ldots \times \mathbb{R}^3$ where $N = 3n$. Then the mapping $\mathbf{r}(t) = (\mathbf{r}_1(t)^T, \ldots, \mathbf{r}_n(t)^T)^T$ which represents

the motion of the n-particle system over time is defined by $\mathbf{r} : \mathbb{R} \mapsto \mathbb{R}^N$, mapping time into

configuration space. The force mapping is defined as $\mathbf{f}(\mathbf{r}, \dot{\mathbf{r}}, t) : \mathbb{R}^N \times \mathbb{R}^N \times \mathbb{R} \mapsto \mathbb{R}^N$.

Now, we can formulate the problem described above by Newton's second law of motion, $\mathbf{f} = M\mathbf{a}$, where $M = diag(m_1, m_1, m_1, m_2, m_2, m_2, \ldots, m_n, m_n, m_n)$ is an $N \times N$ diagonal matrix with the masses m_i repeated along the diagonal. Utilizing $\mathbf{a} = \ddot{\mathbf{r}}$, it yields a system of ordinary differential equations for the system configurations $\mathbf{r}$ at time t, given by

$$M\ddot{\mathbf{r}} = \mathbf{f}, \quad \mathbf{r}(0) = \mathbf{r}_0, \quad \dot{\mathbf{r}}(0) = \mathbf{v}_0. \tag{3.1}$$

If assuming that the total force on the particles $\mathbf{f}$ is conservative (irrotational and time-independent), then the force can be expressed in terms of the potential function as

$$\mathbf{f} = -\nabla \Phi(\mathbf{r}),$$

where $\Phi : \mathbb{R}^N \mapsto \mathbb{R}$, and the gradient operator is defined as $\nabla = (\partial\Phi/\partial\mathbf{r}_1, \ldots, \partial\Phi/\partial\mathbf{r}_n)$. Then the system can be rewritten as:

$$M\ddot{\mathbf{r}} = -\nabla\Phi, \quad \mathbf{r}(0) = \mathbf{r}_0, \quad \dot{\mathbf{r}}(0) = \mathbf{v}_0. \tag{3.2}$$

Solving this system of equations analytically is not practically possible in most cases, so numerical methods must be employed. In any numerical procedure, the focus is to evaluate the force function $\mathbf{f}$ from the potential function Φ which is generally the sum of three distinct potential functions, namely,

$$\Phi = \Phi_1 + \Phi_2 + \Phi_3, \tag{3.3}$$

where Φ_1 is the short-ranged field which may include the van der Waals (vdW) potential, or the Lennard-Jones potential, while Φ_2 is the external field which could include the externally applied fields. The long-ranged field Φ_3 would include the electrostatic

potential. While the short-ranged field, by definition, exhibits rapid decay (for example, the Lennard-Jones 6-12 power potential of noble gases decays as $|\mathbf{r}|^{-6}$), the long-ranged field decays much more slowly (for example, the electrostatic potential decays only as $|\mathbf{r}|^{-1}$). Therefore, to approximate each field for a N-particle system to a high accuracy, the complexity of the computation is clear:

Φ_1: short-ranged, rapid decay, only local interactions considered, $O(N)$;

Φ_2: external field, independent of all the other particles, $O(N)$;

Φ_3: long-ranged, slow decay, all pair-wise interactions, $O(N^2)$.

A more detailed empirical potential energy function is given by [41]

$$E = \sum_{\text{bonds}} k_b (b - b_0)^2 + \sum_{\text{angles}} k_\theta (\theta - \theta_0)^2 + \sum_{\text{torsions}} k_\omega [\cos(n\omega + \gamma) + 1]$$
$$+ \sum_{\text{atom pairs}} \left[\left(\frac{A_{ij}}{r_{ij}^{12}} - \frac{B_{ij}}{r_{ij}^{6}} \right) + \frac{q_i q_j}{r_{ij}} \right], \tag{3.4}$$

where the first three summations are contributions due to, respectively, deviations of bond lengths b from their equilibrim values b_0, deviations of valence angles θ from their equilibrium values θ_0, and torsional potentials from bond rotations (dihedral angles ω with phase shifts γ of the n-fold term). The fourth summation is composed of the van der Waals (vdW) interactions represented by Lennard-Jones 6-12 potentials, and the Coulomb electrostatic interactions [41].

As the first three terms and the vdW potential in the fourth summation in (3.4) are all short-ranged interactions which are negligible when inter-particle distances are great enough, computation of the long-ranged field potential shows the most challenges in practical numerical computations. Furthermore, as the biomolecules always occur in solvents such as ionic water solutions, the large numbers of ions, together with the

difficulty in far field computation, makes this approach infeasible for large biomolecules. The continuum model mentioned in Section 1.1, in which some portion of problem (3.2) is treated as a dielectric continuum governed by partial differential equations instead of the system of ODEs, provides an alternative way in many cases where only the macro-properties of the system are important. The Debye-Hückel theory, discussed more fully later, is a continuum approach which may be particularly suitable for molecular dynamics when the electrostatic interaction is the dominant force in determining the behavior of the simulation system.

3.1.2   Debye-Hückel theory and Poisson-Boltzman equation

In this sub-section, starting from Equation (1.1) in Section 1.1, we provide a comprehensive derivation of the Poisson-Boltzman (PB) equation based on the Debye-Hückels potential of mean force (PMF) approximation for electrostatic interactions for biomolecules in ionic solvent. More in-depth topics in Poisson-Boltzman electrostatics and analytical approximations are discussed in [5].

Recall that the macroscopic potential $\Phi(\mathbf{r})$ is governed by the Poisson equation (1.1) and two interface conditions (1.3), where $n_i(\mathbf{r})$ is the density of i-type ions at the position $\mathbf{r}$ which needs to be derived based on Debye-Hückel theory for homogeneous electrolytes of various ions. In this theory, an *ion-cloud* model is adopted to compute the electric potential of an overall neutral system, where one single ion is randomly selected as the reference point of the system while the rest of the ions in the solvent will be modeled as a *cloud made of continuous charge density distribution* [4]. This selected single ion (called a j-ion) is considered non-polarizable by other ions or external charges and can be represented by a

spherical cavity of radius a with total charge at its center ez_j. In the ion-cloud model, all the other ions except the j-ion is described by a continuous charge number distribution $n_i^j(\mathbf{r})$ per unit volume, centering around the j-ion, though all types of ions are of finite size [18]. Then the potential $\Phi_j(\mathbf{r})$ resulting from the j-ion satisfies the Poisson equation below [26]:

$$-\epsilon\nabla^2\Phi_j(\mathbf{r}) = \begin{cases} ez_j\delta(\mathbf{r}), & \text{if } r < a, \\ e\sum\limits_i z_i n_i^j(\mathbf{r}), & \text{if } r > a, \end{cases} \tag{3.5}$$

where $n_i^j(\mathbf{r})$ is the number concentration per unit volume of the i-type ions around the selected j-ion and is given by the following equation in terms of a radial distribution function (RDF) between two types of ions $g_{ij}(r)$ [5]:

$$n_i^j(\mathbf{r}) = n_i^0 g_{ij}(\mathbf{r}), \tag{3.6}$$

where n_i^0 is the number density of the i-type ions in the bulk and the RDF $g_{ij}(r)$ tends to 1 as r tends to infinity. The fact that n_i^j is a function of the distance r is only due to the fact that the system is homogeneous. The RDF $g_{ij}(r)$ can also be expressed in terms of a Gibbs average over all other ions and charge configurations. For example, by a Boltzman factor weighted integration over all other ions and charge positions in the phase space [26], $g_{ij}(\mathbf{r})$ is given by

$$g_{ij}(\mathbf{r}) = g_{ij}(\mathbf{r}_i, \mathbf{r}_j) = N(N-1)\frac{\int e^{-U/k_B T}d\Gamma'}{Z}, \tag{3.7}$$

where $d\Gamma' = dr_1\ldots dr_N/dr_i dr_j$, and $U(\mathbf{r}_1, \ldots, \mathbf{r}_N)$ is the interaction potential among all N particles including ions, solvent molecules, etc., while Z is the partition function given

by

$$Z = \int e^{-U/k_B T} dr_1 \cdots dr_N. \tag{3.8}$$

Rewriting (3.7) yields the following form

$$g_{ij}(\mathbf{r}_i, \mathbf{r}_j) = e^{-\omega(r_i, r_j)/k_B T} = e^{-\omega_{ij}/k_B T}, \tag{3.9}$$

in which the physical meaning of $g_{ij}(\mathbf{r}_i, \mathbf{r}_j)$ is shown. And we have

$$-\omega_{ij} = k_B T ln \int e^{-U/k_B T} d\Gamma' + C, \tag{3.10}$$

where C is a constant. Now differentiating w_{ij} with respect to either of the two particles, say, r_i, we have

$$-\nabla_i \omega_{ij} = \frac{\int e^{-U/kT}(-\nabla_i U) d\Gamma'}{\int e^{-U/kT} d\Gamma'} \equiv \frac{\int e^{-U/kT} \mathbf{f}_i d\Gamma'}{\int e^{-U/kT} d\Gamma'} \equiv < \mathbf{f}_i >_{mean}, \tag{3.11}$$

where $\mathbf{f}_i = -\nabla_i U$ is the force acting on the particle i for any given configuration of other $N-1$ particles in the system, while $< \mathbf{f}_i >_{mean}$ is the mean force on the particle i averaging from all possible configurations of other $N-1$ particles. ω_{ij} is therefore called the potential of mean force (PMF).

One of the important assumptions in the Debye-Hückel theory is that the mean force applied on the i-type ions is the electrostatic force only, ignoring all nonelectrostatic potentials such as short range van der Waals (vdW) potentials [10]. This assumption means, in terms of the potentials, that the PMF is given by

$$\omega_{ij} = ez_i \Phi_j(\mathbf{r}). \tag{3.12}$$

Now by substituting (3.9) and (3.12) into (3.6), we have the distribution of the i-type

ions given by

$$n_i(r) = n_i^0 \, exp\left(-\frac{ez_i\Phi_j}{k_BT}\right). \tag{3.13}$$

Dropping the subscript j and combining (3.13) and (1.1), we obtain the equation for electrostatic potential Φ:

$$-\nabla \cdot \epsilon(\mathbf{r})\nabla\Phi(\mathbf{r}) = \rho(\mathbf{r}) + \sum_i ez_i n_i^0 exp\left(-\frac{ez_i\Phi}{k_BT}\right). \tag{3.14}$$

(3.14) is referred to as the nonlinear Poisson-Boltzman equation governing the electrostatic potential Φ in all regions in the system. If using the first two terms in the Taylor series $e^{-x} = 1 - x + \frac{x^2}{2!} + \ldots$ as an approximation to e^{-x}, a linearization of (3.14) is obtained [26]:

$$-\nabla \cdot \epsilon(\mathbf{r})\nabla\Phi(\mathbf{r}) = \rho(\mathbf{r}) + \sum_i ez_i n_i^0 \left(1 - \frac{ez_i\Phi}{k_BT}\right), \tag{3.15}$$

provided that

$$\frac{ez_i\Phi}{k_BT} \ll 1. \tag{3.16}$$

Due to the neutrality of the solution, we have $\sum_i ez_i n_i^0 = 0$, with which (3.15) can be further simplified to

$$\nabla^2\Phi(\mathbf{r}) - \lambda^2\Phi(\mathbf{r}) = -\frac{1}{\epsilon}\rho(\mathbf{r}), \tag{3.17}$$

where λ is the inverse Debye-Hückel screening length given by

$$\lambda^2 = \frac{e}{\epsilon k_BT}\sum_i en_i^0 z_i^2 = \frac{2e}{\epsilon k_BT}I, \tag{3.18}$$

and I is the ionic strength defined as

$$I = \frac{1}{2}\sum_i en_i^0 z_i^2. \tag{3.19}$$

Although the validation of (3.16) is not justified in some cases of the biological

simulation system, the solution of nonlinearized Poisson-Boltzman is usually approximated by solving the linearized form (3.17). Analytical solutions to both the nonlinear and linearized poisson-Boltzman equations are complex, even in some simple situations for which they exist. To simplify the notations, we combine the Poisson equation in the solute region and the Poisson-Boltzman equation in the solvent region into a single equation given by

$$-\nabla \cdot \epsilon(\mathbf{r})\nabla\Phi(\mathbf{r}) + \kappa^2\Phi(\mathbf{r}) = \rho(\mathbf{r}), \quad \mathbf{r} \in \Omega_i \text{ or } \mathbf{r} \in \Omega_o, \tag{3.20}$$

with the interface condition (1.3) and a decaying condition at infinity, namely,

$$\lim_{r \to \infty} \Phi(\mathbf{r}) = 0, \tag{3.21}$$

where

$$\epsilon(r) = \begin{cases} \epsilon_i, & \text{if } \mathbf{r} \in \Omega_i, \\ \epsilon_o, & \text{if } \mathbf{r} \in \Omega_o, \end{cases} \qquad \kappa^2 = \begin{cases} \epsilon_i\lambda_i^2, & \text{if } \mathbf{r} \in \Omega_i, \\ \epsilon_o\lambda_o^2, & \text{if } \mathbf{r} \in \Omega_o. \end{cases} \tag{3.22}$$

Note that the dielectric constant $\epsilon(\mathbf{r})$ and ionic density are assumed to be piecewise constants at Ω_i and Ω_e. At Ω_i, $\kappa = 0$ is results from $\lambda_i = 0$ because the interior solute region is modeled by the Poisson equation.

3.2 2nd order image charge approximation with arbitrary ionic strength

As discussed in Section 2.1.1, the point charge in the dielectric cavity polarizes the surrounding dielectric medium, which in turn generates a reaction field to the electric field throughout the cavity. This reaction field, which dominates the computational cost for calculating the electric field inside the cavity, can be efficiently taken care of by the image charge methods.

For an ionic solvent, various order accurate multiple image charge approximations were developed, provided that $u = \lambda a < 1$, where λ is the inverse Debye screening length and a is the spherical radius. In some hybrid explicit/implicit solvent models of biomolecular simulations, λ^2 is proportional to the ionic strength I, and a is the radius of the sphere which is often used to enclose biomolecules of irregular shapes (e.g. ions, proteins, etc.). In practice, the requirement $u = \lambda a < 1$ is hard to meet due to the high ionic strength or large size of the biomolecule that often occurs. A new image charge approximation was proposed recently for the reaction field for solvents with no restriction on u imposed [42]. In this section, we give a review of this new development of image charge approximations of reaction fields for a charge inside a dielectric spherical cavity immersed in an ionic solvent with arbitrary ionic strength and cavity size. This method extends our applicability of the image charge approximations of the reaction field in computer simulations of biomolecular solvation.

3.2.1   Reaction field of a point charge

As discussed in Section 3.1.2, the electrostatic potential Φ is given by (3.20) in the Poisson-Boltzman theory. Writing this equation in the interior and exterior regions of the sphere separately, we have

$$\nabla \cdot (\epsilon_{\mathrm{i}} \nabla \Phi(\mathbf{r})) = -\sum_k q_k \delta(\mathbf{r} - \mathbf{r}_k), \quad \mathbf{r} \in \Omega_{\mathrm{i}}, \tag{3.23}$$

$$\nabla^2 \Phi(\mathbf{r}) - \lambda^2 \Phi(\mathbf{r}) = 0, \quad \mathbf{r} \in \Omega_{\mathrm{e}}, \tag{3.24}$$

and the two interface conditions for the continuities of the potentials and the fluxes along the normal direction hold as in (1.3).

By the principle of linear superposition, the reaction field due to a single point charge q located at $\mathbf{r}_s=(r_s,0,0)$ inside a spherical cavity of radius a centered at the origin only needs to be considered.

The solution $\Phi(\mathbf{r})$ inside and outside the sphere for the Poisson-Boltzmann system can be written in the following form of the Kirkwood series expansion [25, 39],

$$\Phi(\mathbf{r}) = \begin{cases} \sum_{n=0}^{\infty} \left[\dfrac{q}{4\pi\epsilon_i r_s} \left(\dfrac{r}{r_s} \right)^n + A_n r^n \right] P_n(\cos\theta), & \text{when } 0 \leq r \leq r_s, \\[2mm] \sum_{n=0}^{\infty} \left[\dfrac{q}{4\pi\epsilon_i r} \left(\dfrac{r_s}{r} \right)^n + A_n r^n \right] P_n(\cos\theta), & \text{when } r_s \leq r \leq a, \\[2mm] \sum_{n=0}^{\infty} B_n k_n(\lambda r) P_n(\cos\theta), & \text{when } r \geq a, \end{cases} \qquad (3.25)$$

in which

$$\Phi_{\mathrm{RF}}(\mathbf{r}) = \sum_{n=0}^{\infty} A_n r^n P_n(\cos\theta) \qquad (3.26)$$

defines the reaction field inside the dielectric cavity. Here, $P_n(x)$ are the Legendre polynomials, and $k_n(r)$ are the modified spherical Hankel functions of order n defined by

$$k_n(r) = \frac{\pi e^{-r}}{2r} \sum_{k=0}^{n} \frac{(n+k)!}{k!(n-k)!} \frac{1}{(2r)^k}. \qquad (3.27)$$

The expansion coefficients A_n and B_n are determined by the boundary conditions (1.3) as

$$A_n = \frac{q}{4\pi\epsilon_i a} \frac{1}{r_K^n} \frac{\epsilon(n+1)k_n(u) + uk_n'(u)}{\epsilon n k_n(u) - uk_n'(u)}, \qquad (3.28)$$

$$B_n = \frac{q}{4\pi\epsilon_i a} \left(\frac{r_s}{a} \right)^n \frac{\epsilon(2n+1)}{\epsilon n k_n(u) - uk_n'(u)}, \qquad (3.29)$$

where $\epsilon=\epsilon_i/\epsilon_o$, and $r_K=a^2/r_s$ with $\mathbf{r}_K=(r_K,0,0)$ being the conventional Kelvin image point.

3.2.2 Image charge approximation for solvents with high ionic strength

In a solution with low ionic strength, the key idea in the development of the image charge methods is to approximate $\mathcal{S}_n(u) = \frac{k_n(u)}{uk'_n(u)}$ with simple rational functions of n when u is small. In the case of high ionic strength when u is large, however, we approximate $\mathcal{S}_n(u)$ in terms of $O\left(1/u^m\right)$. In particular, we have

$$\mathcal{S}_n(u) = -\frac{1}{n+1+u} + O\left(\frac{1}{u^2}\right), \quad \text{for } n \geq 0, \tag{3.30}$$

which is a second-order approximation for large u. In addition, when u tends to zero, we have

$$\mathcal{S}_n(u) = -\frac{1}{n+1+u} + O\left(u\right), \quad \text{for } n \geq 0. \tag{3.31}$$

The order of convergence can be easily proved as following:

As $u \to \infty$, since $k_n(u)/k'_n(u) = -1 + O(1/u)$ and $\mathcal{S}_n(u) = -1/u + O(1/u^2)$, we have

$$\mathcal{S}_n(u) + \frac{1}{n+1+u} = -\frac{n+1}{u(n+1+u)} + O\left(\frac{1}{u^2}\right) = O\left(\frac{1}{u^2}\right).$$

On the other hand, as $u \to 0$, due to $\mathcal{S}_n(u) = -1/(n+1) + O(u^2)$ and

$$\frac{1}{n+1} - \frac{1}{n+1+u} = \frac{u}{(n+1)(n+1+u)} = O(u),$$

we have

$$\mathcal{S}_n(u) = -\frac{1}{n+1+u} + O\left(u\right).$$

Applying (3.31) to (3.28) leads to an approximation of the expansion coefficient A_n as

$$A_n = \frac{q}{4\pi\epsilon_i a}\frac{1}{r_K^n}\left(\gamma + \frac{\delta_A}{n+\sigma_A}\right), \tag{3.32}$$

where

$$\sigma_{\mathrm{A}} = \frac{1 + u}{1 + \epsilon}, \qquad \delta_{\mathrm{A}} = \gamma\left(1 - \sigma_{\mathrm{A}}\right) - \frac{u}{1 + \epsilon}.$$

Since

$$\frac{1}{n + \sigma_{\mathrm{A}}} = r_{\mathrm{K}}^{n + \sigma_{\mathrm{A}}} \int_{r_{\mathrm{K}}}^{\infty} \frac{1}{x^{n + \sigma_{\mathrm{A}} + 1}} \mathrm{d}x, \tag{3.33}$$

and the expansion of the reciprocal distance

$$\frac{1}{|\mathbf{r} - \mathbf{x}|} = \frac{1}{x} \sum_{n=0}^{\infty} \left(\frac{r}{x}\right)^n P_n(\cos\theta), \quad \text{when} \quad 0 \le r < x, \tag{3.34}$$

we obtain the following line image approximation for the reaction field

$$\Phi_{\mathrm{RF}}(\mathbf{r}) \approx \frac{q_{\mathrm{K}}}{4\pi\epsilon_{\mathrm{i}}|\mathbf{r} - \mathbf{r}_{\mathrm{K}}|} + \int_{r_{\mathrm{K}}}^{\infty} \frac{q_{\mathrm{A}}^{\mathrm{line}}(x)}{4\pi\epsilon_{\mathrm{i}}|\mathbf{r} - \mathbf{x}|} \mathrm{d}x, \tag{3.35}$$

where the line image charge is now

$$q_{\mathrm{A}}^{\mathrm{line}}(x) = q\frac{\delta_{\mathrm{A}}}{a}\left(\frac{x}{r_{\mathrm{K}}}\right)^{-\sigma_{\mathrm{A}}}, \quad \text{for} \quad r_{\mathrm{K}} \le x. \tag{3.36}$$

Note that when $n = 0$, the approximation of $\mathcal{S}_0(u)$ equals exactly $-1/(1 + u)$, so no correction term is required for the reaction field.

3.2.3 Line image charge approximation

We can improve the accuracy of the line image approximation (3.35) by modifying the asymptotical formula of $\mathcal{S}_n(u)$ to

$$\mathcal{S}_n(u) = -\frac{1}{(n + 1) + \frac{u^2}{1 + u}} + O\left(\frac{1}{u^2}\right). \tag{3.37}$$

The second-order accuracy can be analyzed in the same way as u tends to infinity. In addition, when u tends to zero, the approximation is at an order of $O(u^2)$; therefore, this

new image charge approximation can cover the low ionic strength as well as the high ionic strength case [11]. The approximation (3.37) is analytical for $n = 1$, and we need to add a position-independent correction term for $n = 0$. By performing a similar deduction, we obtain an approximation to the reaction field

$$\Phi_{\mathrm{RF}}(\mathbf{r}) \approx \frac{q_{\mathrm{K}}}{4\pi\epsilon_{\mathrm{i}}|\mathbf{r} - \mathbf{r}_{\mathrm{K}}|} + \int_{r_{\mathrm{K}}}^{\infty} \frac{q_{\mathrm{B}}^{\mathrm{line}}(x)}{4\pi\epsilon_{\mathrm{i}}|\mathbf{r} - \mathbf{x}|}\mathrm{d}x + \Phi_{\mathrm{B}}^{\mathrm{cor}}, \tag{3.38}$$

with the line image charge

$$q_{\mathrm{B}}^{\mathrm{line}}(x) = q\frac{\delta_{\mathrm{B}}}{a}\left(\frac{x}{r_{\mathrm{K}}}\right)^{-\sigma_{\mathrm{B}}}, \quad \text{for} \quad r_{\mathrm{K}} \leq x, \tag{3.39}$$

and

$$\sigma_{\mathrm{B}} = \frac{1 + \tilde{u}}{1 + \epsilon}, \quad \delta_{\mathrm{B}} = \gamma\left(1 - \sigma_{\mathrm{B}}\right) - \frac{\tilde{u}}{1 + \epsilon}, \quad \tilde{u} = \frac{u^2}{1 + u}.$$

Here, the correction term is

$$\Phi_{\mathrm{B}}^{\mathrm{cor}} = \frac{q}{4\pi\epsilon_{\mathrm{i}}a}\left(\frac{\epsilon}{1 + u} - 1 - \gamma - \frac{\delta_{\mathrm{B}}}{\sigma_{\mathrm{B}}}\right) = \frac{q}{4\pi\epsilon_{\mathrm{i}}a}\left(\frac{\epsilon}{1 + u} - \frac{\epsilon}{1 + \tilde{u}}\right). \tag{3.40}$$

3.2.4 Discrete multiple image approximation

To obtain multiple image charge approximations to the reaction field, each line image charge introduced in Equations (3.35) and (3.53) is approximated by a set of discrete point image charges, i.e.,

$$\int_{r_{\mathrm{K}}}^{\infty} \frac{q_{\mathrm{X}}^{\mathrm{line}}(x)}{4\pi\epsilon_{\mathrm{i}}|\mathbf{r} - \mathbf{x}|}\mathrm{d}x \approx \sum_{m=1}^{M} \frac{q_m^{\mathrm{X}}}{4\pi\epsilon_{\mathrm{i}}|\mathbf{r} - \mathbf{x}_m^{\mathrm{X}}|}, \tag{3.41}$$

where $\mathbf{x}_m^{\mathrm{X}} = (x_m^{\mathrm{X}}, 0, 0)$, and for $m = 1, 2, \cdots, M$,

$$q_m^{\mathrm{X}} = \frac{\delta_{\mathrm{X}}}{2\sigma_{\mathrm{X}}}\frac{w_m x_m^{\mathrm{X}}}{a}q, \qquad x_m^{\mathrm{X}} = r_{\mathrm{K}}\left(\frac{2}{1 - s_m}\right)^{1/\sigma_{\mathrm{X}}},$$

and $s_m, w_m, m = 1, 2, \cdots, M$, are Jacobi-Gauss quadrature points and weights on the interval $[-1, 1]$. The label X represents "A" or "B".

3.3   The hybrid solvation model and its theory

3.3.1   Introduction to the Image-Charge Solvation Model (ICSM)

In Section 1.2, we discussed three major categories of the approaches which are widely used to treat electrostatic interactions over the past decades: implicit, explicit and hybrid. In this section, we will focus on the hybrid models and in particular, introduce a new hybrid explicit/implicit model based on the image charge methods mentioned in Chapter 1.2. Our method, termed Image-Charge Solvation Model (ICSM) was first proposed in a paper by Lin *et al.* [30] and was tested for pure liquid water. As one of the advanced hybrid models, the ICSM combines the strengths of both implicit and explicit representations of the solvent. In our model, solute molecules and some solvent molecules within a central spherical cavity are treated explicitly, thus, removing the continuum approximation near the solute. Reaction fields acting on the explicit part are generated by a continuum dielectric medium surrounding the cavity. The reaction fields are computed efficiently by employing the image-charge method and the fast multipole expansion technique. The rest of the this chapter will be devoted to giving a detailed discussion of the mathematical theory and description of the model. Test results to validate our model will be also presented in Section 3.4.2.

3.3.2   Calculation of the reaction field with the multiple-image charges approach

This sub-section covers the mathematical theory and formulas which are utilized to compute reaction fields. Our model, proposed in this work, is based on the spherical
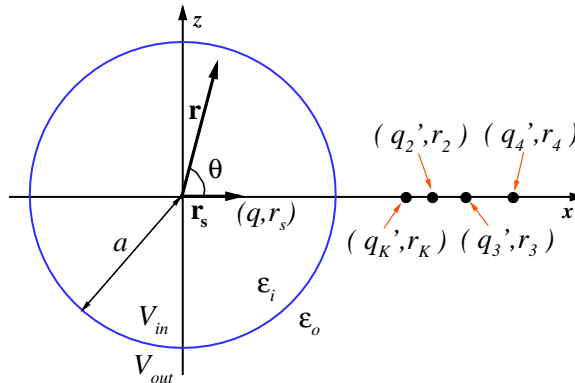
Figure 3.1: An illustration of how the multiple-image method is applied to compute the reaction field in a spherical cavity V_{in} embedded in the solvent bath V_{out}.

geometry of the solute. Consider a local volume Γ of spherical cavity and with dielectric permittivity ϵ_i embedded in an infinite solvent with dielectric permittivity ϵ_o, as shown in Figure 3.1. According to the Debye-Hückel Poission-Boltzmann theory discussed in Section 3.1.2, the total electrostatic potential $\Phi(\mathbf{r})$ in this scheme is given by the Poisson-Boltzmann equation:

$$\epsilon_i \nabla^2 \Phi(\mathbf{r}) = -\rho_{in}(\mathbf{r}), \qquad \mathbf{r} \in V_{in}, \tag{3.42a}$$

$$\left[\nabla^2 - \lambda^2\right] \Phi(\mathbf{r}) = 0, \qquad \mathbf{r} \in V_{out}, \tag{3.42b}$$

where V_{in} is the interior region of the spherical cavity containing all explicit charges of the solute and solvent molecules; ρ_{in} is the charge distribution at V_{in} which is given by

$$\rho_{in}(\mathbf{r}) = \sum_i q_i \delta(\mathbf{r} - \mathbf{r}_i); \tag{3.43}$$

and λ is the inverse Debye-Hückel screening length. In a pure solvent like water, $\lambda = 0$. While in solutions with nonzero ionic strength which are modeled in this work, $\lambda \neq 0$. On the surface of the cavity, two boundary conditions for the continuities of the potentials and

the fluxes along the normal direction hold, i.e.

$$\Phi_{in} = \Phi_{out} \quad \text{and} \quad \epsilon_i \frac{\partial \Phi_{in}}{\partial \mathbf{n}} = \epsilon_o \frac{\partial \Phi_{out}}{\partial \mathbf{n}}, \tag{3.44}$$

where Φ_{in} and Φ_{out} are the values of the potential inside and outside the cavity respectively, and $\mathbf{n}$ is the unit outward vector normal to the surface of the cavity.

Due to the principle of linear superposition, we only need to focus our discussion, in this subsection, on a single point charge q located at $\mathbf{r}_s = (r_s, 0, 0)$ inside the cavity. As discussed in Section 3.1.2, the total potential, which is the solution of (3.42) and (3.44) at position $\mathbf{r}$ inside the cavity V_{in}, can be expressed as the sum of the primary field Φ_S which results from the source charge and the reaction field Φ_{RF} which is created by the source-induced polarization of the solvent in the outside region of the cavity V_{out}, namely

$$\Phi = \Phi_S + \Phi_{RF}. \tag{3.45}$$

For the case of a spherical cavity with radius a, Φ_{RF} inside the cavity is given by the Kirkwood expansion, which in the ionic solution case $\lambda \neq 0$ is

$$\Phi_{\text{RF}}(\mathbf{r}) = \sum_{n=0}^{\infty} A_n r^n P_n(\cos\theta), \tag{3.46}$$

$$A_n = \frac{q}{4\pi\epsilon_i a} \frac{1}{r_{\text{K}}^n} \frac{\epsilon(n+1)k_n(u) + uk'_n(u)}{\epsilon n k_n(u) - uk'_n(u)}, \tag{3.47}$$

$$k_n(r) = \frac{\pi e^{-r}}{2r} \sum_{k=0}^{n} \frac{(n+k)!}{k!(n-k)!} \frac{1}{(2r)^k}. \tag{3.48}$$

where $\epsilon = \epsilon_i/\epsilon_o$, and $r_{\text{K}} = a^2/r_s$.

To employ the Kelvin image charge, r_{K} represents the location of the classic Kevin image charge with charge $q_k = \gamma a q/r_s$, where $\gamma = (\epsilon_i - \epsilon_o)/(\epsilon_i + \epsilon_o)$. Then the potential of the

Kevin image charge is given by

$$V\left(q_K, \mathbf{r}_K; \mathbf{r}\right) = \frac{q_K}{4\pi\epsilon_i \left|\mathbf{r} - \mathbf{r}_K\right|}. \tag{3.49}$$

Using a second-order accuracy approximation discussed in Section 3.2, the reaction field inside the cavity Φ_{RF} is given by the sum

$$\Phi_{RF}(\mathbf{r}) \approx V\left(q_K, \mathbf{r}_K; \mathbf{r}\right) + \int_{r_K}^{\infty} V(q^{\text{line}}(x), \mathbf{x}; \mathbf{r})dx + \Phi^{\text{cor}}, \tag{3.50}$$

where q^{line} is the line image charge given by

$$q^{\text{line}}(x) = \frac{\delta q}{a}\left(\frac{x}{r_K}\right)^{-\sigma}, \quad r_K \leq x, \tag{3.51}$$

and

$$\sigma = \frac{1+\tilde{u}}{1+\epsilon}, \quad \delta = \gamma\left(1 - \sigma_C\right) - \frac{\tilde{u}}{1+\epsilon}, \quad \tilde{u} = \frac{u^2}{1+u},$$

$$\Phi^{\text{cor}} = \frac{q}{4\pi\epsilon_i a}\left(\frac{\epsilon}{1+u} - 1 - \gamma - \frac{\delta}{\sigma}\right) = \frac{q}{4\pi\epsilon_i a}\left(\frac{\epsilon}{1+u} - \frac{\epsilon}{1+\tilde{u}}\right). \tag{3.52}$$

Next, to obtain multiple discrete image charge approximations to the integral in (3.50), a set of discrete point image charges are employed through Gauss integration quadratures, yielding

$$\Phi_{\text{RF}}(\mathbf{r}) \approx \frac{q_K}{4\pi\epsilon_i|\mathbf{r} - \mathbf{r}_K|} + \sum_{m=1}^{N_i} \frac{q'_m}{4\pi\epsilon_i|\mathbf{r} - \mathbf{r}_m|} + \Phi^{\text{cor}}, \tag{3.53}$$

where the magnitude and the location of all discrete image charges are defined as

$$q'_m = \frac{\delta}{2\sigma}\frac{w_m r_m}{a}q, \qquad r_m = r_K\left(\frac{2}{1 - s_m}\right)^{1/\sigma},$$

and s_m, w_m, $m = 1, 2, \ldots, N_i$, are Jacobi-Gauss quadrature points and weights on interval $[-1, 1]$.

Remarks:

1. This approach is based on the work of Neuman and is general enough for computation of Φ_{RF} with arbitrary accuracy at any point $\mathbf{r}$ inside the cavity. The accuracy of the approximation is controlled by the number of image charges employed N_i only; thus, it is not affected by the ratio of the solute and solvent dielectric permittivities ϵ_i/ϵ_o. Although the greater the number N_i is, the better the approximation is, large N_i increases the computational cost of the problem.

2. One of the main objectives to formulate discrete image charge approximations is to apply the treatment by fast multipole methods (FMM). It is discussed previously that combining the FMM and the image charge method can achieve an $O(N)$ complexity in the calculating the electrostatic interactions among N charges inside a dielectric sphere.

3. As the correction term in (3.53) is a constant for given ionic strength and cavity radius, the gradient of Φ^{cor} is zero; thus, it does not contribute to the force between charges/atoms in the simulation system.

3.3.3   Description of the hybrid image charge solvation model with ionic solvents

1) Buffer layer between explicit and implicit solvents

As shown in (3.49), the reaction field computed at the boundary between explicit and implicit solvents $r = a$ diverges. To remove the mathematical singularity at $r = a$ and to prevent the electrostatic forces from growing too high when particles approach the boundary, we consider a mathematical model that utilizes two different radii for one

spherical cavity. This is illustrated in Figure 3.2. The central cavity with a radius R_c is separated from the dielectric continuum with permittivity ϵ_o by a buffer layer of thickness τ. The radius a used for the calculation of reaction field in (3.53) is $a = R_c + \tau$, which is slightly larger than R_c.

The central cavity as well as the buffer layer are filled with solvent. The reaction field is generated by charges within the bigger sphere with the radius r but it acts only on the charges within the central cavity with radius R_c. Adopting this buffer layer in our model is also a means to reduce the surface effect which is a intrinsic property of models involving a sharp transition between two dielectric media. Charges inside the central cavity with radius R_c will not feel the presence of the surface if the thickness of the buffer layer τ is large enough.
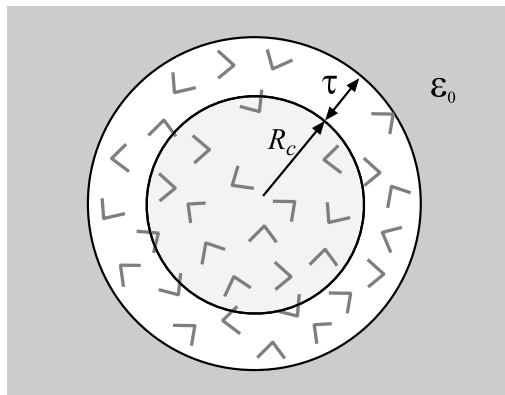

Figure 3.2: Cartoon illustrating the buffer layer filled with solvent.

2) Boundary conditions

While the dielectric boundary is treated by the buffer layer, the boundary conditions as they apply to other potentials, primarily dispersion forces between solvent molecules and their surroundings, are discussed in detail here. To overcome the limitation of the

droplet models and the moving boundary reaction field method, an advanced strategy was proposed which combines the PBC in the simulation cell with the fixed boundary in the spherical cavity [3]. This approach allows nonhomogeneous systems to be simulated with minimal surface effects and also avoids the coexistence problem of two different regions of water in one simulation box. As shown in Figure 3.3, the radius of the central spherical cavity R_c reaches the furthest point in the simulation box from the center of the sphere. As the central cavity encloses the entire simulation box, all particles are treated by the same electrostatics method. For illustrative purposes, a cubic simulation box is shown in the demonstration Figure 3.3. We will discuss the simulation box type in detail later. Due to the application of PBC and the difference in the geometry between a sphere and a cube, some particles within the R_c radius are not unique but periodic images from the nearest copies of the simulation box. How two periodic images are created is illustrated by the dark-shaded areas in Figure 3.3, while the light-shaded areas display all imaged parts within the simulation box. The central part shaded in lightest color, is the area where the charges are not imaged and this area serves as the "productive" region of the simulation box. A solute molecule placed in this "productive" region avoids electrostatic interactions with its periodic image copies.

3) Simulation box type

As shown in Figure 3.3, our mathematical model will accurately represent a solute molecule embedded in an infinite bath of solvent, if the central "productive" region is large enough to also include the nearest solvation shell. Thus, when considering the simulation box type, our goal is to maximize the area of this "productive" region whose size is determined by the difference in the distance between the furthest and nearest points
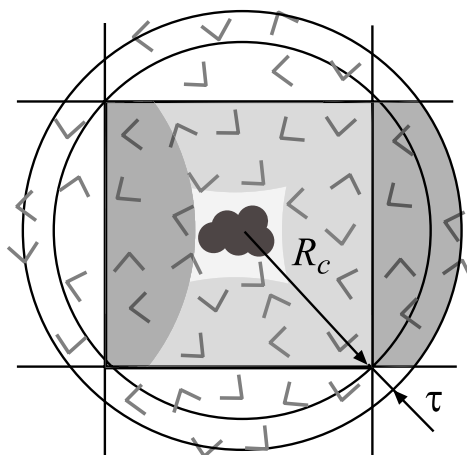
Figure 3.3: Cartoon showing the spherical cavity integrated with a cubic simulation box under PBCs.
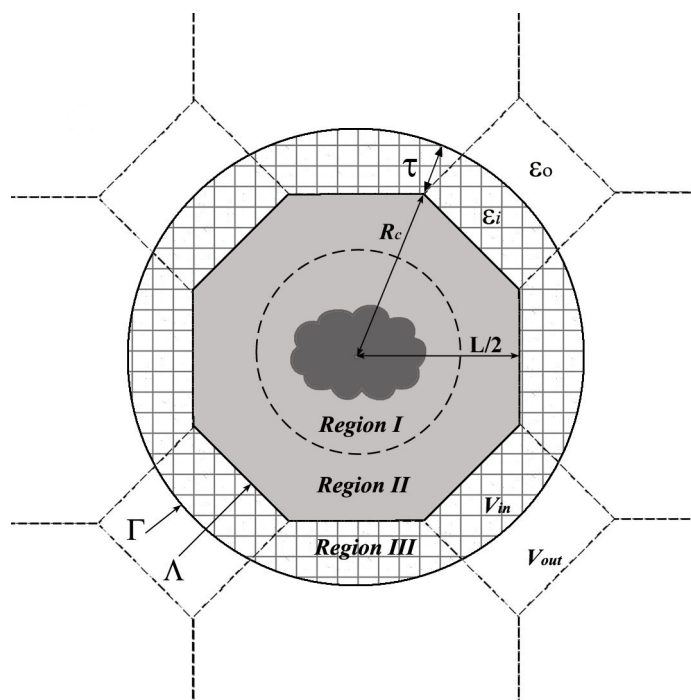

Figure 3.4: Cartoon representing the model used in this work to treat electrostatic interactions of solute molecules embedded in solvent under PBCs.

in the simulation box to the center. In this work, we focus on the truncated octahedron (TO) geometry which is proved in a previous paper by Lin *et al.* to be among the best in terms of maximizing the size of the productive region [30].

Our TO box Λ is created from a cube of length L by cutting all the eight corners at a distance $(1/4\sqrt{2})L$ from the center of its sides. Thus, this TO box has 14 faces (including 8 regular hexagonal faces and 6 square faces) and 24 vertices. Distances from the origin to the square face, to the hexagonal faces and to the corners are $(1/2)/L$, $(\sqrt{3}/4)/L$ and $(\sqrt{5}/4)/L$, respectively. Since the distance from the origin to the furthest point in this geometry is $(\sqrt{5}/4)/L$, the radius of the central sphere is $R_c = (\sqrt{5}/4)/L$. Figure 3.4 shows the cross section of the TO box in the XZ plane with its center at the origin, in which three regions are displayed:

Region I: The inner-most sphere area inside the broken line, where charges are not periodically imaged, is the "productive" region of the simulation box. As discussed previously, a solute molecule in this region may be solvated without experiencing any artificial electrostatic solute-solute interactions. The size of Region I varies among simulation box geometries. In the case of TO box, the radius of this region is $d = L(\sqrt{3} - \frac{\sqrt{5}}{2}) - 2\tau = 0.61L - 2\tau$. If we compare this to the same quantity for a cubic simulation box $d = L(2 - \sqrt{3}) - 2\tau = 0.27L - 2\tau$, the advantage of using the TO geometry is obvious.

Region II: All the remaining area in the TO box Λ excluding the central Region I. Particles in Region II have image copies in the larger sphere cavity Γ of radius $R_c + \tau$.

Region III: Particles in the 14 nearest neighbors around the central simulation box which are at a distance less than $R_c + \tau$ from the origin form a buffer layer, which is shown as the

hatched area.

All charges in the larger cavity Γ, including Region I, II and III, generate a reaction field computed by the image-charge method and acts on the charges in the simulation box Λ. Therefore, the electrostatic forces acting on charges in the main simulation box are least affected by the periodicity artifacts. To compute other nonbonded interactions, such as dispersion forces, standard PBCs with the nearest-image convention are employed. In the simulation of this work, the solvent, consisted of sodium chloride paired ions and water molecules, move freely in all Regions I, II and III.

In summary, the electrostatic force field calculation in the ICSM involves the following three successive steps [2]:

1. Locate periodic images in Region III for those solvent particles in Region II of the main simulation box;

2. Find image charges of reaction field for all charges inside the spherical cavity Γ, including all real charges inside the main simulation box Λ and all periodic images in Region III;

3. Calculate the electrostatic force inside the main simulation box Λ exerted by all charges, including all real charges inside the main simulation box Λ, all periodic images in Region III, and all image charges of reaction fields outside the spherical cavity Γ.

3.4   Numerical results and discussion

3.4.1   Computational details

In this work, the TIP3P all-atom model is used to characterize properties of bulk water because of its simplicity and computational efficiency. All molecular dynamics simulations by the image charge method as well as the trajectory analysis were performed by an in-house software which was developed specially for this project by our research group. To evaluate the electrostatic forces within the simulation box Λ, we adopt a free software KIFFMM developed by Ying *et al.* which uses a kernel-independent adaptive FMM.

The positions and velocities of particles were generated according to an implementation of the velocity Verlet algorithm by Jang and Voth, coupled with the Nosé-Hoover thermostat. The expression for the update of the positions, based on the old positions and velocities, is given by [15]

$$r(t + \Delta t) = r(t) + \Delta t v(t + \Delta t/2), \tag{3.54}$$

and the velocities are updated by

$$v(t + \Delta t/2) = v(t - \Delta t/2) + \Delta t \frac{f(t)}{m}. \tag{3.55}$$

The dielectric constants of the internal and external fields were set to 1 and 80 respectively. The van der Waals interactions were modeled by the Lennard-Jones potential with the truncated distance at 10 Å. The integration time step was set to $2 \, fs$. The temperature of the simulation system was controlled at a constant $T = 300K$ and the thermostats coupling constant was set to $0.05 \, ps$. The trajectories were recorded at every $0.2 \, ps$ for subsequent analysis.

Table 3.1: Parameters for generating the initial coordinates by GROMACS.

	Parameters	Value
Weak coupling to an external heat bath	coupling time constant τ_T	0.1 ps
	target temperature T_0	300 K
Weak coupling barostat	time constant τ_P	0.5 ps
	isothermal compressibility β	$4.5 \times 10^{-5} atm^{-1}$
	target pressure P_0	1 atm

The initial coordinates of the water molecules were generated by the GROMACS program package, from an equilibrium $200\ ps$ simulation in NPT ensemble. A weak coupling to an external heat bath and a weak coupling barostat were applied with parameters shown in Table 3.1. Covalent bonds of TIP3P water molecules were constrained using SHAKE procedure with a relative tolerance of 10^{-4}. Once equilibrium was reached, the system was cut to the desired TO box size. This was followed by randomly replacing the desired number of water molecules by ions (e.g. one pair of sodium chloride ions took the place of two water molecules). The systems were then equilibrated again.

In this work, 15 systems with the same box size but different numbers of sodium chloride pairs were simulated, with the numbers of ions and water molecules listed in Table 3.2. The box side length of the cube from which the TO box was built was 45 Å. Two different buffer layer thicknesses 6 Å and 8 Å were used to test the buffer layer effects with each of the 15 systems. In total, 30 different simulations were performed in this study. The total simulation time was 9 ns for each of the MD simulation. All trajectories were analyzed between 3 ns and 9 ns, leaving the first 3 ns as equilibrium time.

For reference purposes, 15 PME simulations were carried out for 9 ns with a cubic box of side length 45 Å using the GROMACS program package. The number of water molecules

and ions in these simulations are summarized in Table 3.2. As with the simulations with image charge method, all of the PME simulations were 9 ns long, and the last 6 ns were used for the analysis.

Table 3.2: Total number of solvent water molecules in image charge method and PME method.

Number of NaCl Pairs	Total number of water molecules	
	Image charge method	PME
1	1405	3015
2	1402	3013
3	1401	3011
4	1398	3009
5	1396	3007
6	1393	3005
7	1390	3003
8	1389	3001
9	1388	2999
10	1387	2997
11	1384	2995
12	1383	2993
13	1381	2991
14	1382	2989
15	1380	2987

3.4.2   Results and discussion

To validate our solvation model, we focus our analysis on a few observables known to be sensitive to the treatment of long-range electrostatics. Some of our results are compared to those of PME, as a reference electrostatics method.

(1) Radial distribution function (RDF)

We evaluated the effect on the structure by the radius distribution functions (RDF) from which the macroscopic thermodynamic quantities can usually be determined. For each case, four pairs of distribution functions were computed over the entire simulation box:

chloride-hydrogen (Cl-H), chloride-oxygen (Cl-O), sodium-hydrogen (Na-H), and sodium-oxygen (Na-O). The general formula to calculate the distribution function of atomA-atomB is given by

$$g_{AB}(r) = \frac{1}{4\pi\rho r^2 dr} \frac{1}{N} \times \left\langle \sum_{\alpha}^{N} \sum_{r < r_{\alpha\beta}(\tau) \leq r+dr, \beta \neq \alpha}^{N} 1 \right\rangle_{\tau}, \quad g_{AB}(0) = 0, \tag{3.56}$$

where ρ is the number density, N is the total number of molecules, and dr is the window size which equals to 0.8 Å here. $r_{\alpha\beta}(\tau)$ represents the minimum image atomA-to-atomB distance between molecules α and β at time τ, and $< \cdot >_\tau$ denotes averaging over all trajectory frames.

We compared the RDFs between two different thicknesses of the buffer layers, $\tau = 6$ Å and $\tau = 8$ Å. The PME results are also plot as a reference. As shown in Figure 3.5 - 3.8, the difference between the two curves of our models $\tau = 6$ Å and $\tau = 8$ Å is unnoticeable, and overall, both of our models agree well with the results obtained in the PME calculations. The most important features of the RDFs are the locations and magnitudes of the first three density peaks and the first two minima. A close look at the first two minima and the second peak of the RDFs using a higher resolution is shown in the insets of Figure 3.5 - 3.8. Those insets reveal that our models' results slightly differ from the PME results only at the magnitudes of the first peak and minimum in a limited number of cases. Our data numerically show that RDF are not very sensitive to the ionic strength, as can be seen in Figure 3.5 - 3.8. These figures also indicate that our model with buffer layer $\tau = 6$ Å performs as well as that with $\tau = 8$ Å in terms of reproducing the structure of liquid ionic solution correctly.
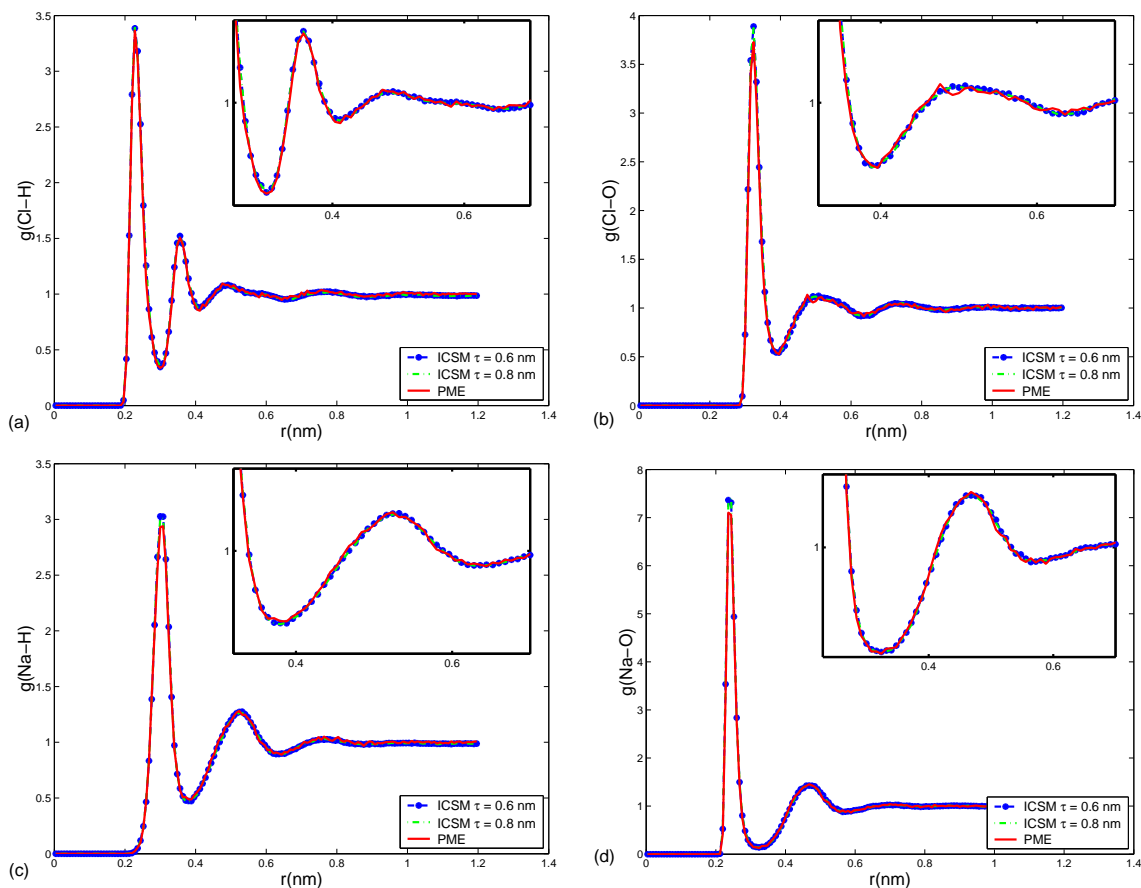
Figure 3.5: RDF computed in this work (1 NaCl pair): (a) Cl-H, (b) Cl-O, (c) Na-H, (d) Na-O.

(2) Density:

(a) Water density

One of the key elements of our model, the sharp boundary between the explicit and implicit solvents, may induce surface effects. As the real bulk water is homogenously distributed, a successful electrostatics model should minimize this surface effect to an acceptable level. To exam the homogeneity of the solvent water in the entire simulated system, relative particle density of the water ρ_r was measured as a function of the position in the simulation box. Due to the symmetry of geometry, it is sufficient for us to look at the density along a line that connects two opposite vertexes of the TO box. To evaluate the
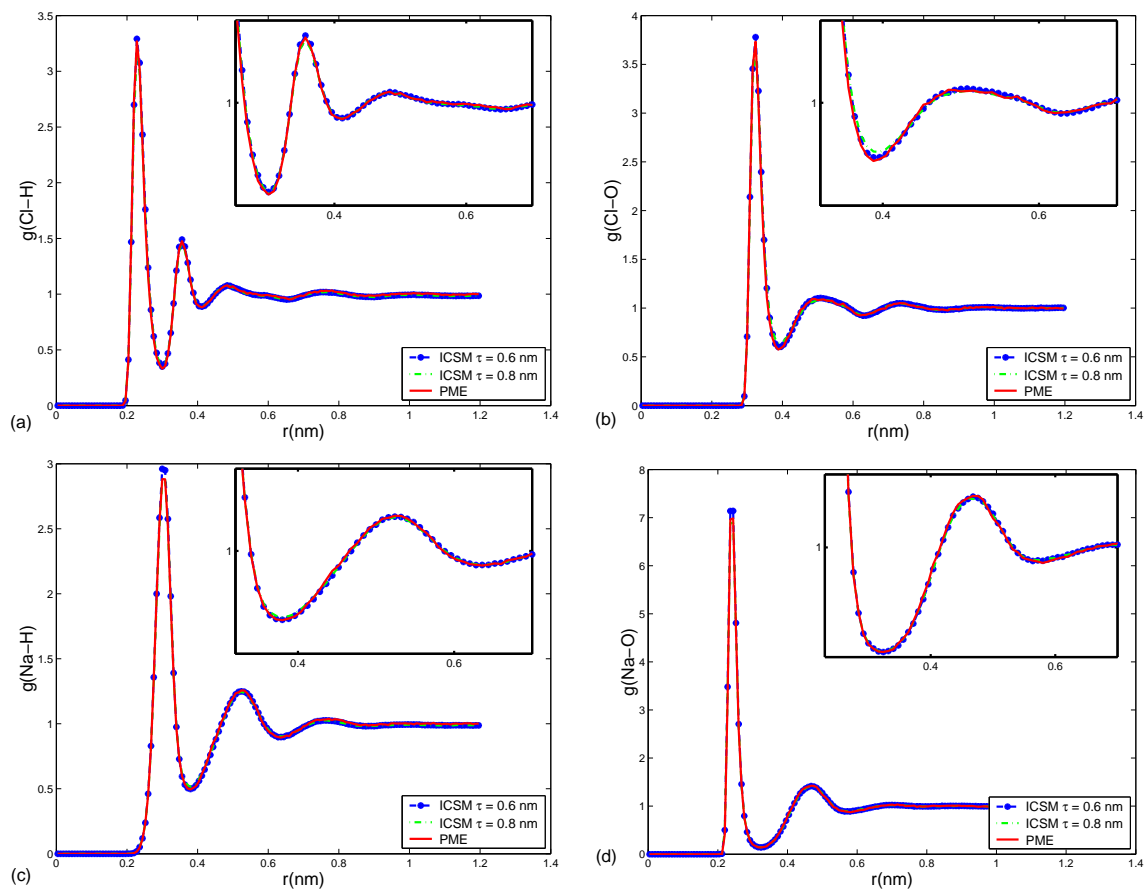
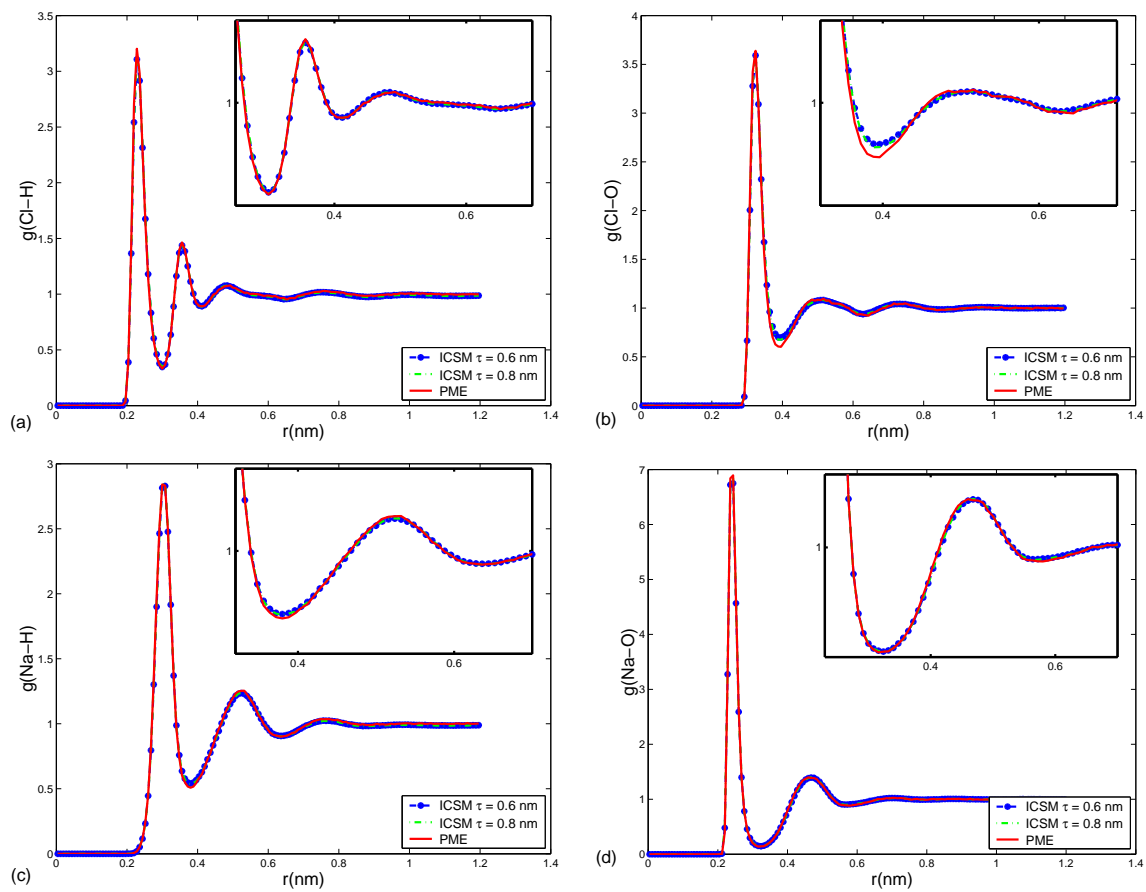Figure 3.6: RDF computed in this work (5 NaCl pairs): (a) Cl-H, (b) Cl-O, (c) Na-H, (d) Na-O.

Figure 3.7: RDF computed in this work (10 NaCl pairs): (a) Cl-H, (b) Cl-O, (c) Na-H, (d) Na-O.
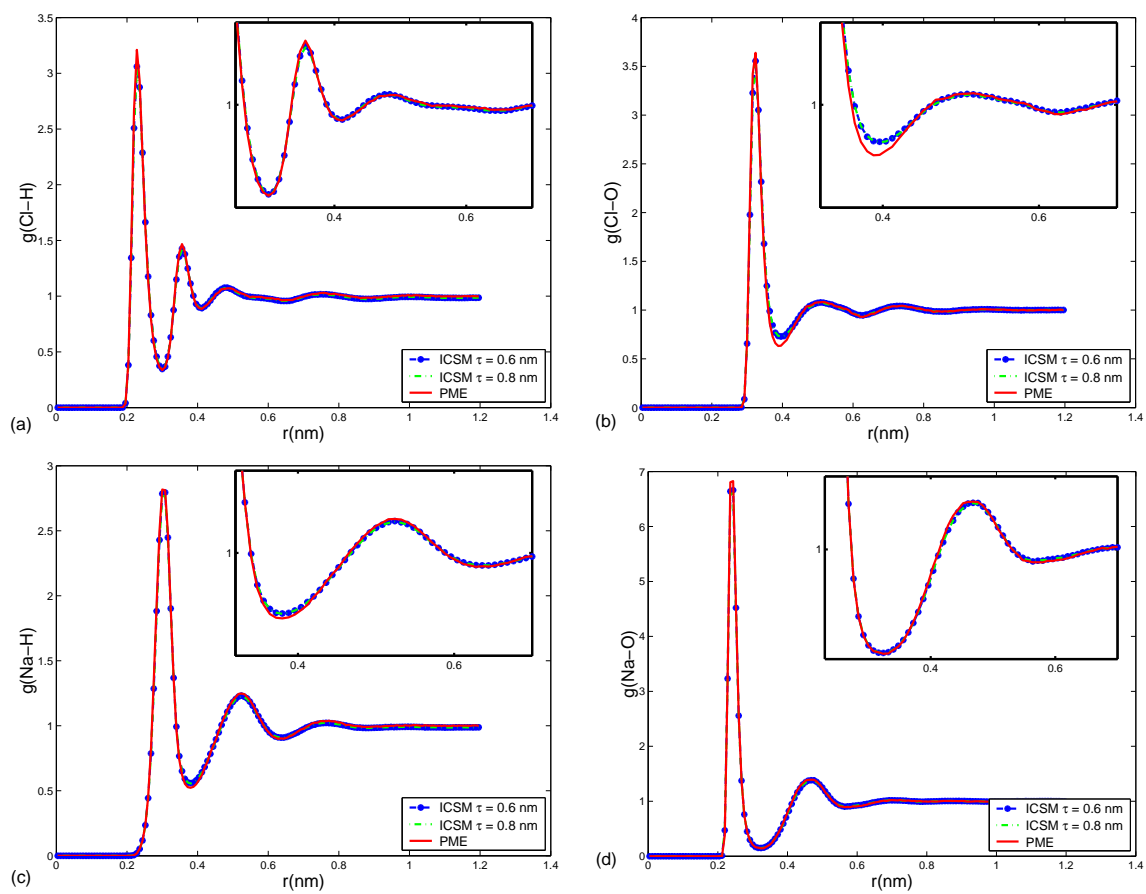
Figure 3.8: RDF computed in this work (15 NaCl pairs): (a) Cl-H, (b) Cl-O, (c) Na-H, (d) Na-O.

local density of the water molecules, a small sphere of radius $r = 5$ Å is drawn around each of the 11 equispaced positions along this line. Using each position as the origin, more specifically, we counted the number of oxygen atoms within each small sphere then converted it to the particle density ρ_i. Normalized with the number density of the whole simulation box, this particle density ρ_i was converted to the relative density ρ_r.

Previous study showed that in aqueous solutions a buffer layer of at least 6 Å is required to yield uniform density of water, and neither the size of the simulation box L nor the number of image charges N_i is important for the density, as long as $N_i > 0$. The relative densities of water along the diagonal of the TO box by our model are shown in Figure 3.9 - 3.12. As can be seen, results of $\tau = 6$ Å and $\tau = 8$ Å are in close agreement with each other, all leading to a uniform water density distribution with some statistical variations. A quantitative summary of the water density deviations along the diagonal is presented in Table 3.3. It is evident that a buffer layer $\tau = 6$ Å works sufficiently well for reducing the surface effects. Increasing the size of the buffer to 8 Å does not lead to a significant improvement in the water density thus $\tau = 6$ Å is good enough to correctly represent homogeneous liquid water.

Table 3.3: Comparison of the standard deviations of relative densities along the diagonal of TO box simulations.

	$\tau = 6$ Å	$\tau = 8$ Å
1 NaCl	0.0018	0.0011
5 NaCl	0.0036	0.0011
10 NaCl	0.0021	0.0014
15 NaCl	0.0027	0.0009

(b) Ion density

Figure 3.9: Relative density of water along the diagonal of TO box with different τ's (1 NaCl pair).

Figure 3.10: Relative density of water along the diagonal of TO box with different τ's (5 NaCl pairs).
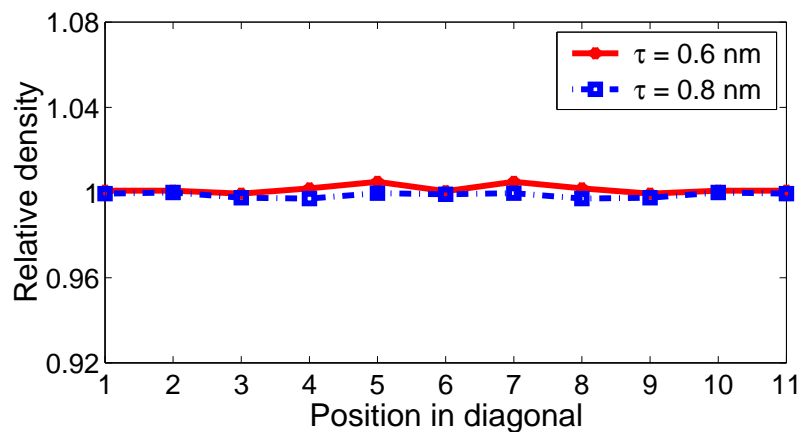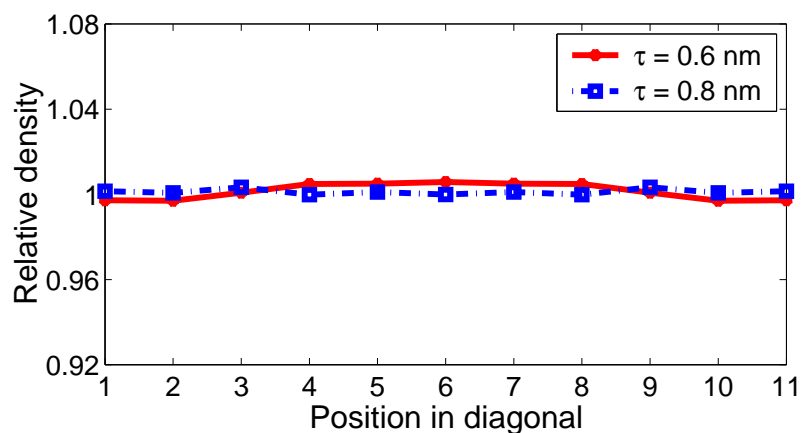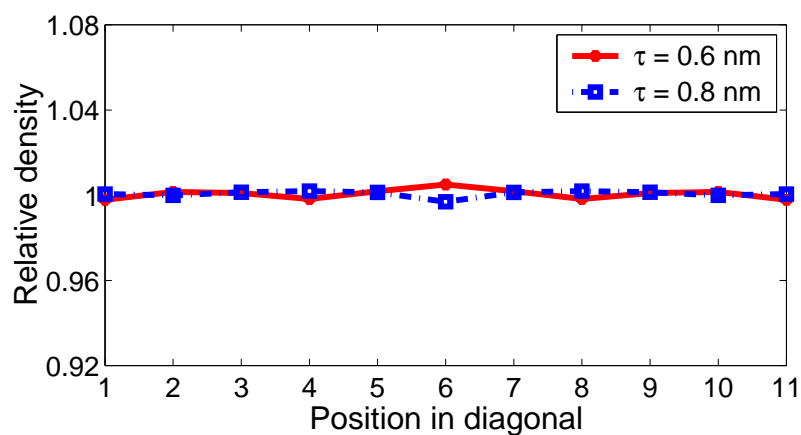

Figure 3.11: Relative density of water along the diagonal of TO box with different τ's (10 NaCl pairs).
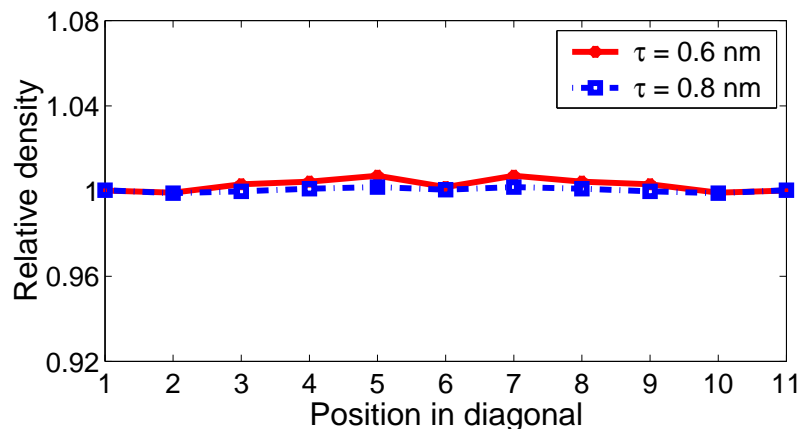
Figure 3.12: Relative density of water along the diagonal of TO box with different τ's (15 NaCl pairs).

Table 3.4: Count of the ion visits within the inscribed sphere of TO box (1 NaCl pair, $\tau = 6$ Å).

Shell no. (from the innermost)	Radius of the Shell (nm)	Areas				Total of the shell
		Area 1	Area 2	Area 3	Area 4	
shell 1	1.22751409	3712	4483	2793	4481	15469
shell 2	1.54657084	3738	3702	2759	2752	12951
shell 3	1.77038167	3470	3410	2093	2387	11360
shell 4	1.94855716	2710	2734	1895	1916	9255

To test the homogeneity of the ion distribution, our idea was to divide the test region into sub-areas with equal volume. In each of these sub-areas, the number of visits of ions was counted and compared.

i) Within the TO box

An inscribed sphere of the TO box was drawn, followed by dividing this sphere into four shells with equal volumes (radii are shown in the second columns of Table 3.4 - 3.11). Each of the shells was then further divided into 4 sub-regions with equal volumes, resulting in 16 sub-regions in total. The number of ion visits in each of these sub-regions is summarized in Table 3.4 - 3.11 and Figure 3.13 - 3.16 (a) and (b) for all the cases of 1, 5, 10, 15 pairs of NaCl respectively.

Table 3.5: Count of the ion visits within the inscribed sphere of TO box (1 NaCl pair, $\tau = 8$ Å).

Shell no. (from the innermost)	Radius of the Shell (nm)	Areas				Total of the shell
		Area 1	Area 2	Area 3	Area 4	
shell 1	1.22751409	3646	2907	3877	3339	13869
shell 2	1.54657084	2893	2791	1567	2412	9663
shell 3	1.77038167	2555	3187	1928	2193	9863
shell 4	1.94855716	1976	3415	2371	1838	9600

Table 3.6: Count of the ion visits within the inscribed sphere of TO box (5 NaCl pairs, $\tau = 6$ Å).

Shell no. (from the innermost)	Radius of the Shell (nm)	Areas				Total of the shell
		Area 1	Area 2	Area 3	Area 4	
shell 1	1.22751409	12044	17364	13465	15458	58331
shell 2	1.54657084	15365	19738	13350	15058	63511
shell 3	1.77038167	13973	16240	10646	13648	54507
shell 4	1.94855716	11847	14928	10116	12798	49689

Table 3.7: Count of the ion visits within the inscribed sphere of TO box (5 NaCl pairs, $\tau = 8$ Å).

Shell no. (from the innermost)	Radius of the Shell (nm)	Areas				Total of the shell
		Area 1	Area 2	Area 3	Area 4	
shell 1	1.22751409	14894	18618	17587	12771	63870
shell 2	1.54657084	13962	16459	13331	14476	58228
shell 3	1.77038167	13295	13599	10898	14063	51855
shell 4	1.94855716	10819	12714	10361	12393	46287

Table 3.8: Count of the ion visits within the inscribed sphere of TO box (10 NaCl pairs, $\tau = 6$ Å).

Shell no. (from the innermost)	Radius of the Shell (nm)	Areas				Total of the shell
		Area 1	Area 2	Area 3	Area 4	
shell 1	1.22751409	30316	28904	28995	24546	112761
shell 2	1.54657084	30208	29827	28547	25498	114080
shell 3	1.77038167	25122	28401	27366	25024	105913
shell 4	1.94855716	25515	27265	26230	24705	103715

Table 3.9: Count of the ion visits within the inscribed sphere of TO box (10 NaCl pairs, $\tau = 8$ Å).

Shell no. (from the innermost)	Radius of the Shell (nm)	Areas				Total of the shell
		Area 1	Area 2	Area 3	Area 4	
shell 1	1.22751409	32458	26253	25933	25490	110134
shell 2	1.54657084	27642	27139	25405	24620	104806
shell 3	1.77038167	26572	26732	24990	24956	103250
shell 4	1.94855716	25831	27560	25397	24728	103516

Table 3.10: Count of the ion visits within the inscribed sphere of TO box (15 NaCl pairs, $\tau = 6$ Å).

Shell no. (from the innermost)	Radius of the Shell (nm)	Areas				Total of the shell
		Area 1	Area 2	Area 3	Area 4	
shell 1	1.22751409	41783	47564	38580	41059	168986
shell 2	1.54657084	41372	43756	39837	36698	161663
shell 3	1.77038167	36843	43717	38829	36315	155704
shell 4	1.94855716	36699	39245	38504	36618	151066

Table 3.11: Count of the ion visits within the inscribed sphere of TO box (15 NaCl pairs, $\tau = 8$ Å).

Shell no. (from the innermost)	Radius of the Shell (nm)	Areas				Total of the shell
		Area 1	Area 2	Area 3	Area 4	
shell 1	1.22751409	37710	41797	44038	44168	167713
shell 2	1.54657084	37675	42054	38438	39158	157325
shell 3	1.77038167	36704	38656	37097	41096	153553
shell 4	1.94855716	36592	37403	37093	40079	151167

Table 3.12: Count of ion visits within the "productive" area (1 NaCl pair, $\tau = 6$ Å).

Shell no. (from the innermost)	Radius of the Shell (nm)	Areas				Total of the shell
		Area 1	Area 2	Area 3	Area 4	
shell 1	0.360652395	150	97	95	92	434
shell 2	0.454393544	107	116	70	131	424
shell 3	0.520150761	133	136	66	149	484
shell 4	0.572499990	111	172	57	170	510

Table 3.13: Count of ion visits within the "productive" area (1 NaCl pair, $\tau = 8$ Å).

Shell no. (from the innermost)	Radius of the Shell (nm)	Areas				Total of the shell
		Area 1	Area 2	Area 3	Area 4	
shell 1	0.360652395	168	137	88	54	447
shell 2	0.454393544	67	53	81	68	269
shell 3	0.520150761	73	80	132	61	346
shell 4	0.572499990	53	92	160	62	367

ii) Within the "productive" region

Our test region here is the "productive" region. Similar to what we did for the TO box, we divided the "productive" region into a total of 16 sub-regions and recorded the numbers of ion visits in each sub-region. Radius of shells and counts of ion visits are shown in Table 3.12 - 3.19 and Figure 3.13 - 3.16 (c) and (d).

Our results indicate that the ion densities within both the TO box and the "productive" area are not shown uniformly distributed when the number of sodium chloride (NaCl) ion pairs is small, especially for the case of one NaCl pair. This is physically true because a smaller number of ions need a longer time to create their homogeneous 'appearance'

Table 3.14: Count of ion visits within the "productive" area (5 NaCl pairs, $\tau = 6$ Å).

Shell no. (from the innermost)	Radius of the Shell (nm)	Areas				Total of the shell
		Area 1	Area 2	Area 3	Area 4	
shell 1	0.360652395	266	437	477	361	1541
shell 2	0.454393544	276	475	394	376	1521
shell 3	0.520150761	209	421	387	387	1404
shell 4	0.572499990	220	373	397	395	1385

Table 3.15: Count of ion visits within the "productive" area (5 NaCl pairs, $\tau = 8$ Å).

Shell no. (from the innermost)	Radius of the Shell (nm)	Areas				Total of the shell
		Area 1	Area 2	Area 3	Area 4	
shell 1	0.360652395	331	464	315	256	1366
shell 2	0.454393544	452	490	453	239	1634
shell 3	0.520150761	490	499	431	209	1629
shell 4	0.572499990	445	423	470	200	1538

Table 3.16: Count of ion visits within the "productive" area (10 NaCl pairs, $\tau = 6$ Å).

Shell no. (from the innermost)	Radius of the Shell (nm)	Areas				Total of the shell
		Area 1	Area 2	Area 3	Area 4	
shell 1	0.360652395	453	567	725	552	2297
shell 2	0.454393544	514	565	742	646	2467
shell 3	0.520150761	623	599	767	650	2639
shell 4	0.572499990	675	639	697	601	2612

Table 3.17: Count of ion visits within the "productive" area (10 NaCl pairs, $\tau = 8$ Å).

Shell no. (from the innermost)	Radius of the Shell (nm)	Areas				Total of the shell
		Area 1	Area 2	Area 3	Area 4	
shell 1	0.360652395	727	820	591	538	2676
shell 2	0.454393544	900	724	595	552	2771
shell 3	0.520150761	863	581	516	615	2575
shell 4	0.572499990	913	583	514	571	2581

Table 3.18: Count of ion visits within the "productive" area (15 NaCl pairs, $\tau = 6$ Å).

Shell no. (from the innermost)	Radius of the Shell (nm)	Areas				Total of the shell
		Area 1	Area 2	Area 3	Area 4	
shell 1	0.360652395	933	954	924	905	3716
shell 2	0.454393544	992	1064	1127	1070	4253
shell 3	0.520150761	958	1226	941	926	4051
shell 4	0.572499990	950	1290	983	917	4140

Table 3.19: Count of ion visits within the "productive" area (15 NaCl pairs, $\tau = 8$ Å).

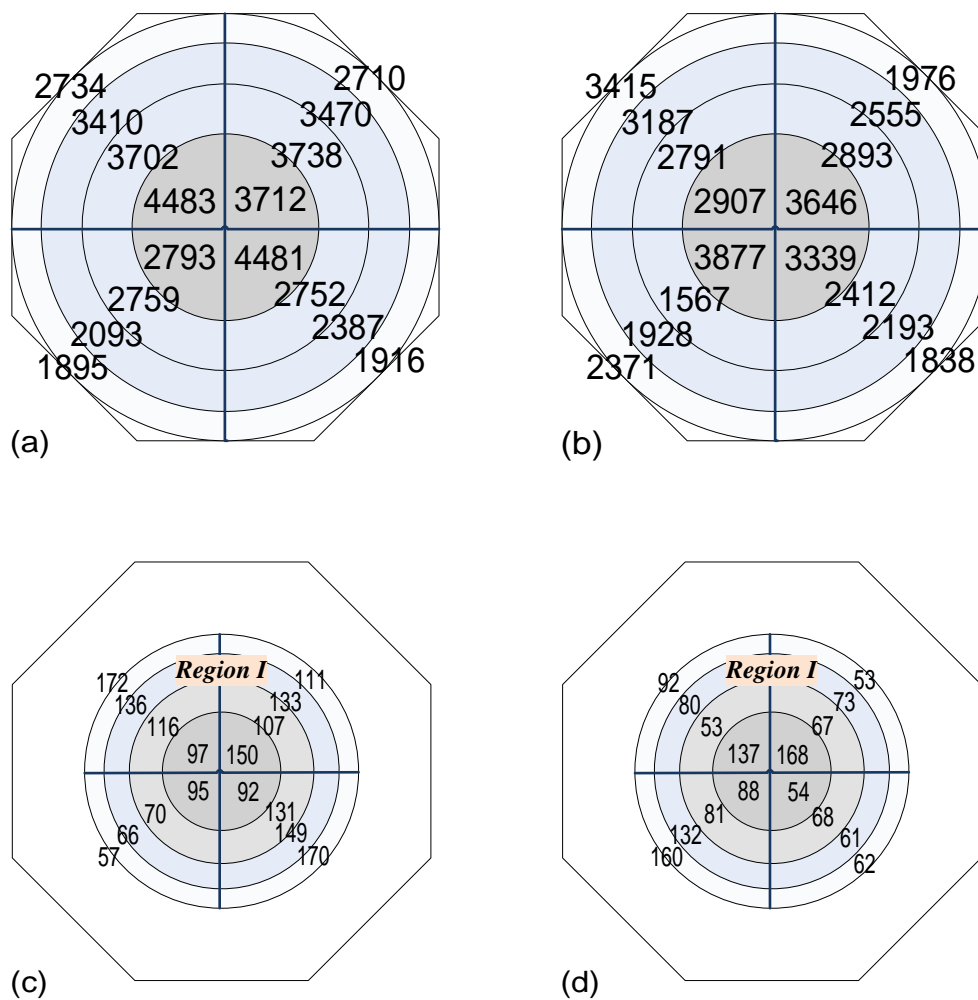| Shell no. (from the innermost)	Radius of the Shell (nm)	Areas				Total of the shell
		Area 1	Area 2	Area 3	Area 4	
shell 1	0.360652395	1065	1058	1042	1095	4260
shell 2	0.454393544	1039	1066	1207	1085	4397
shell 3	0.520150761	1077	1080	1231	1083	4471
shell 4	0.572499990	1001	1022	1240	1111	4374

Figure 3.13: Ion density for 1 NaCl pair (a)Within TO box ($\tau = 6$ Å), (b)Within TO box ($\tau = 8$ Å), (c) Within "productive" area ($\tau = 6$ Å), (d) Within "productive" area ($\tau = 8$ Å).
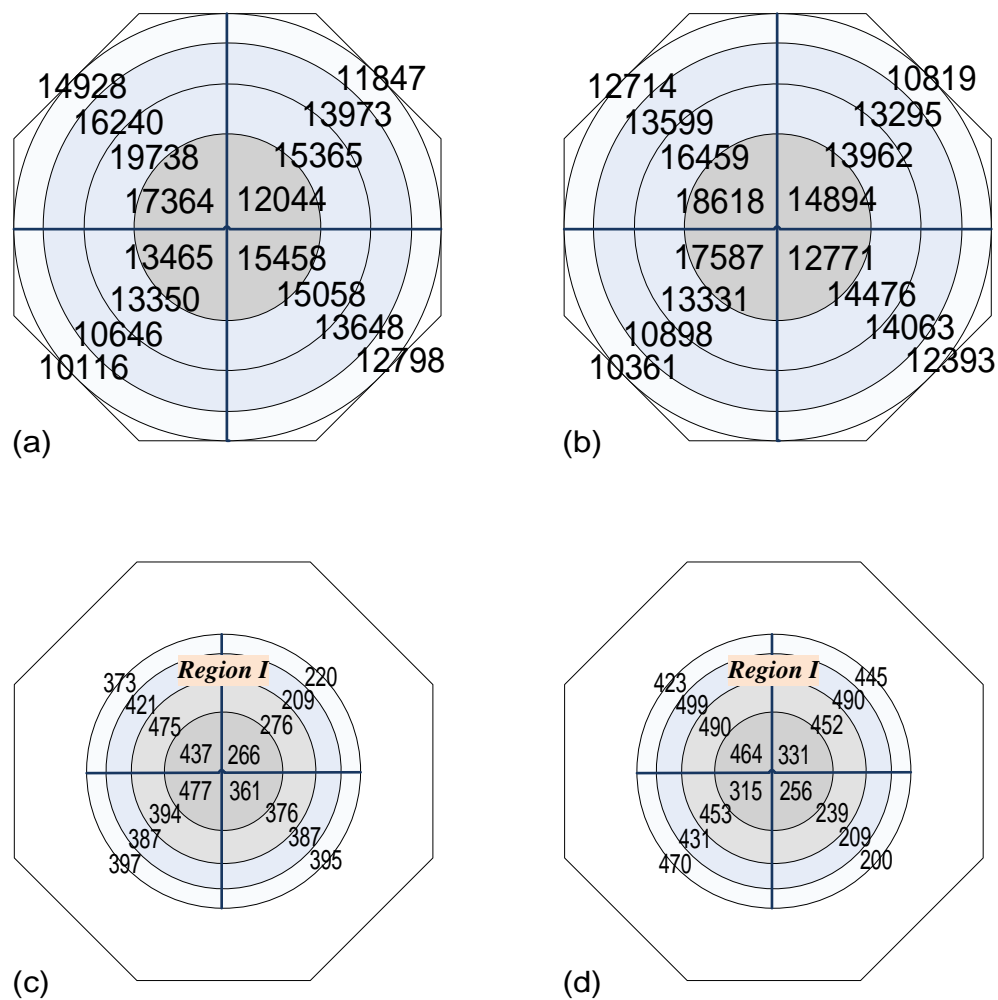
Figure 3.14: Ion density for 5 NaCl pairs (a)Within TO box ($\tau = 6$ Å), (b)Within TO box ($\tau = 8$ Å), (c) Within "productive" area ($\tau = 6$ Å), (d) Within "productive" area ($\tau = 8$ Å).

Figure 3.15: Ion density for 10 NaCl pairs (a)Within TO box ($\tau = 6$ Å), (b)Within TO box ($\tau = 8$ Å), (c) Within "productive" area ($\tau = 6$ Å), (d) Within "productive" area ($\tau = 8$ Å).

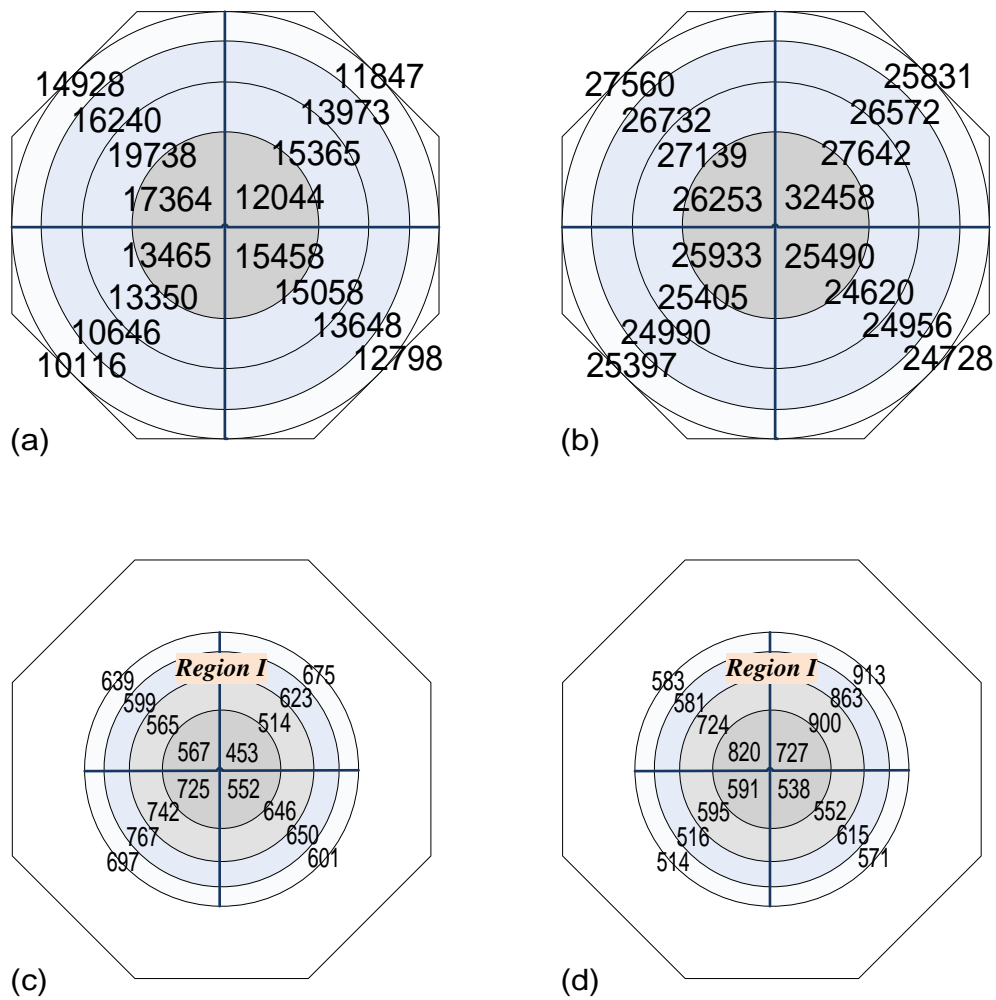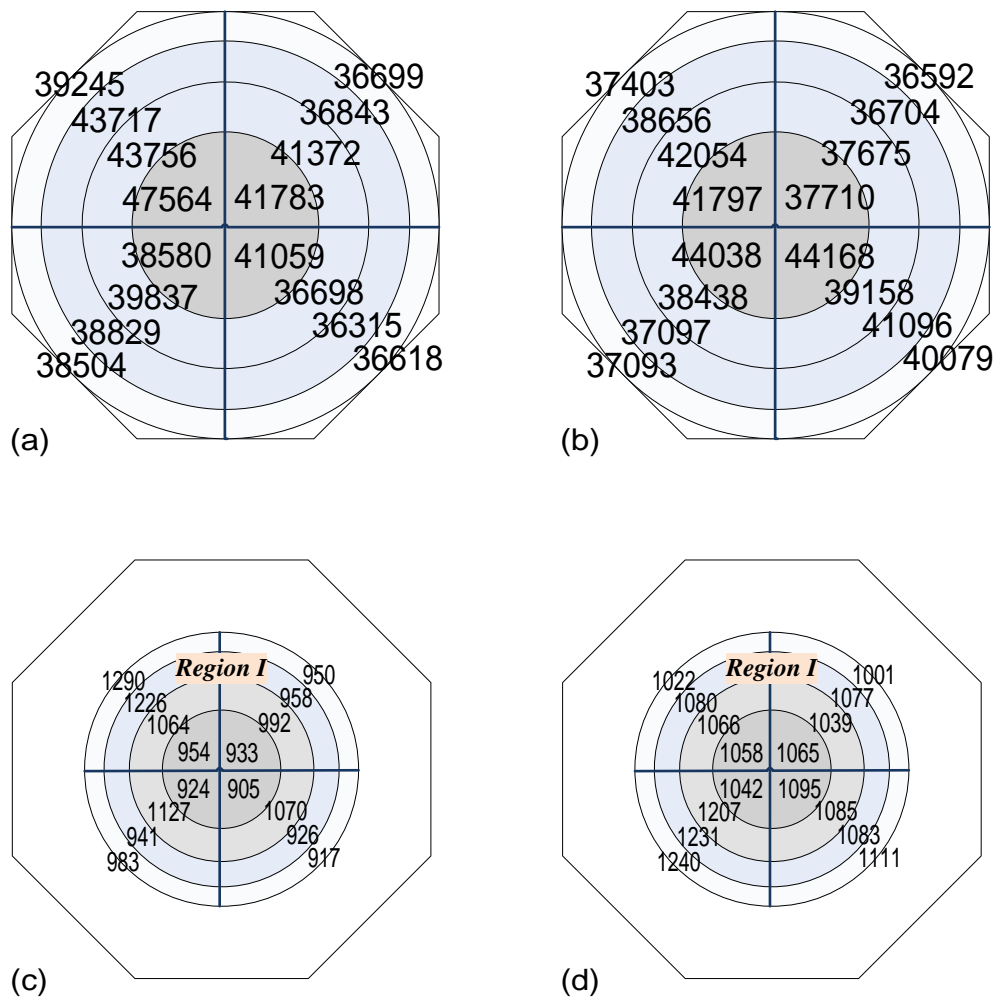Figure 3.16: Ion density for 15 NaCl pairs (a)Within TO box ($\tau = 6$ Å), (b)Within TO box ($\tau = 8$ Å), (c) Within "productive" area ($\tau = 6$ Å), (d) Within "productive" area ($\tau = 8$ Å).

within the entire area that they can reach. With the increase of the number of NaCl pairs to be added, the ion density becomes more and more uniform. As shown in Table 3.18 - 3.19 and Figure 3.16(c)(d), for the case of 15 NaCl pairs, the ion density data demonstrates the capability of our model for simulating a homogeneous ionic solvent within the "productive" area.

(3) Diffusion coefficient

In addition to the structural properties, the dynamical properties were also tested as an assessment of our electrostatics model. We choose to evaluate the self-diffusion of water molecules by calculating the diffusion coefficients from the mean square displacement (MSD) of all oxygen atoms using the Einstein relation below:

$$\lim_{t \to \infty} \left\langle |\mathbf{r}(t' + t) - \mathbf{r}(t')|^2 \right\rangle = 6Dt, \tag{3.57}$$

where $\mathbf{r}(t)$ is the position of the oxygen atom of the water molecule at time t, D is the self-diffusion coefficient and $< \cdot >$ donates averaging over all water molecules and time at origins t'.

The diffusion coefficients calculated by our two models ($\tau = 6$ Å and $\tau = 8$ Å) as well as the results of PME are summarized in Table 3.20. Comparing the two buffer layers, the thickness of the buffer layer τ has no noticeable effect on D, at least for the simulation box $L = 45$ Å. This indicates that $\tau = 6$ Å performs as well as $\tau = 8$ Å in terms of reproducing the dynamics of water molecules. For this system, as shown in Figure 3.17, the diffusion coefficients D, from both the imaged charge methods and PME, decrease with statistical errors when the number of sodium chloride pairs increases. This makes sense since as the number of sodium and chloride ions increases, the oxygen atoms in

Table 3.20: Diffusion coefficients with standard deviation (unit of $D = 10^{-9}m^2s^{-1}$).

# of Nacl pairs	ICSM method $(N_i = 1, L = 45\text{Å TO box})$		PME $(L = 45\text{Å cubic box})$
	$\tau = 6$ Å	$\tau = 8$ Å	
1	6.18($\pm$0.06)	6.16($\pm$0.04)	6.02($\pm$0.02)
2	6.16($\pm$0.05)	6.15($\pm$0.06)	6.00($\pm$0.01)
3	6.14($\pm$0.05)	6.12($\pm$0.06)	5.77($\pm$0.08)
4	6.13($\pm$0.06)	6.11($\pm$0.05)	6.06($\pm$0.28)
5	6.12($\pm$0.06)	6.10($\pm$0.05)	5.73($\pm$0.06)
6	6.11($\pm$0.06)	6.08($\pm$0.06)	5.74($\pm$0.08)
7	6.07($\pm$0.05)	6.06($\pm$0.05)	5.67($\pm$0.05)
8	6.07($\pm$0.06)	6.06($\pm$0.05)	5.66($\pm$0.24)
9	6.02($\pm$0.05)	6.00($\pm$0.05)	5.78($\pm$0.03)
10	6.01($\pm$0.07)	5.98($\pm$0.06)	5.73($\pm$0.24)
11	5.99($\pm$0.06)	5.96($\pm$0.06)	5.53($\pm$0.06)
12	5.95($\pm$0.06)	5.92($\pm$0.06)	5.58($\pm$0.14)
13	5.94($\pm$0.09)	5.92($\pm$0.06)	5.69($\pm$0.07)
14	5.90($\pm$0.07)	5.90($\pm$0.07)	5.75($\pm$0.37)
15	5.91($\pm$0.08)	5.85($\pm$0.08)	5.57($\pm$0.07)

water diffuse more slowly; thus, D goes down. Importantly, the diffusion coefficients D computed for increasing thickness of the buffer layer agree progressively better with those obtained in the PME calculations, although their difference is very small.
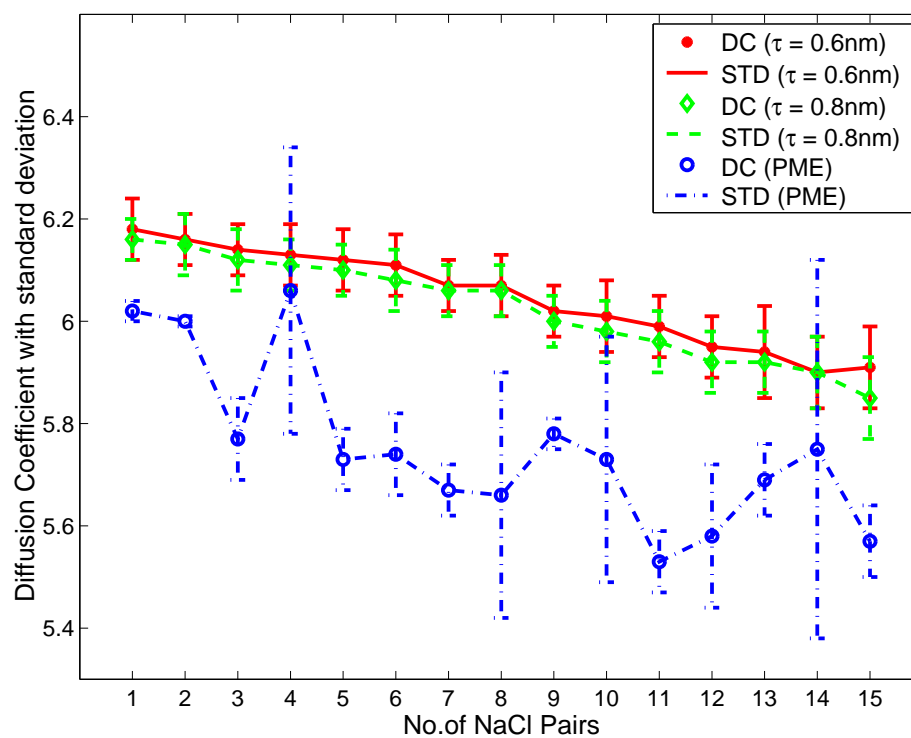
Figure 3.17: Diffusion coefficients error plot.

CHAPTER 4: CONCLUSIONS AND FUTURE WORK

4.1　Conclusions

In this thesis, we have first presented a sixth-order image approximation to the reaction field due to a point charge inside a dielectric sphere immersed in an ionic solvent for small values of $u = \lambda a$ (λ - the inverse Debye screening length of the ionic solvent, a - the radius of the dielectric sphere). $O(N)$ implementations of the image approximation in the electric potential and force field evaluations have been described. Numerical results have demonstrated the sixth-order convergence rate of the image approximation as well as the $O(N)$ complexity of the $O(N)$ implementations of the image approximation. Numerical results have also demonstrated that, compared to the previous fourth-order image approximation, the proposed sixth-order image approximation is more accurate for cases with large u values when a relatively large M value is used.

To apply the image approximation methodology to the molecular simulation to treat electrostatic interactions, we developed the Image Charge Solvation Model (ICSM) which was first introduced in [30] and further tested its performance in simulations of ionic solvent. The ICSM model is a hybrid electrostatic approach that combines the strengths of both explicit and implicit representations of the solvent. A major advantage of the ICSM over the lattice-sum methods, such as PME, is that the solute molecule does not experience electrostatic interactions with its own periodic images. We validated our model

using the ionic solvent as a test system which consisted of water molecules and sodium chloride paired ions. As a result of an extensive investigation, we find that our method is fairly consistent with the PME simulations in reproducing several known physical properties of the ionic solvent. The homogeneity test of water molecules as well as that of ions both demonstrate the capability of our model in simulating a homogeneous system. By a comparison between the two thicknesses of buffer layers, we found that $\tau = 6$ Å performs as well as $\tau = 8$ Å, at least for a TO simulation box with size of $L = 45$ Å.

4.2   Future work

Our model is eventually designed for inhomogeneous systems, and it is free of periodic artifacts in electrostatic interactions,and thus, can be applied in areas where PME is not suitable. One of our future works is to apply the ICSM as a general tool to more complicated molecules such as proteins and viruses which may be bigger in size and vary in geometries. In order for us to do it, we will need to integrate ICSM into the TINKER Molecular Modeling package, which is a complete and general package for molecular mechanics and dynamics with some special features for biopolymers. To avoid drifting outside of the main simulation box, proteins or other big solute in the model will have to be restrained to lie close to the center of, and better within, the "productive area" so that a buffer layer with sufficient thickness to the implicit boundary is affordable. In a recent paper by Baker *et al.*, ICSM was integrated into the molecular dynamics portion of the TINKER package and this integrated package is validated through test simulations of liquid water [2]. We intend to extend and test this integration further in the simulations of ionic solvent in the future.

In existing hybrid solvation models, the spherical geometry is often employed because the reaction field can be solved analytically in such geometry. Moreover, when the image approximation methods are applied, the image charges can be easily found in this case. However, this treatment may become inefficient in applications involving non-spherical solutes such as certain globular proteins and other elongated biopolymers like actin and DNA. For solutes of irregular shapes, using a non-spherical cavity to incorporate only a few layers of solvent molecules adjacent to the solutes would make the simulated system much smaller. However, how to efficiently obtain an accurate reaction field for such cases remains a great challenge. In particular, to employ solvation shells with irregular shapes, the Poisson equations need to be solved either directly by the numerical methods or by using the approximation theory at every simulation time step, which, depending on the system size, may become more computationally expensive than standard explicit all-atom solvent models. Therefore, for studying a biomolecule of irregular shape, it may be more appropriate to adopt a non-spherical but still regular-shaped cavity that can conform closely to the irregular shape of the biomolecule. Employing a regular-shaped cavity (but "less regular" than a sphere) may make it still possible to find some simple but accurate enough image approximations for the corresponding reaction field, thus avoiding the solution of the Poisson equation at every simulation time step. In a recent paper by Deng *et al.*, the hybrid ICSM has been extended to use prolate spheroidal or more general triaxial ellipsoidal cavities for the case of pure water solvent [13]. Extending this generalized ICSM further for the ionic solvent will be a focus of our future work.

REFERENCES

[1] Abramowitz, M., Stegun, I.A.: Handbook of Mathematical Functions with Formulas, Graphs, and Mathematical Tables. Dover Publications, New York (1972)

[2] Baker, K., Baumketner, A., Lin, Y., Deng, S., Jacobs, D., Cai, W., ICSM: An order N method for calculating electrostatic interactions added to TINKER, submitted to Computer Physics Communication, 4/2012.

[3] Barker, J.A., Watts, R.O., Monte-Carlo studies of dielectric properties of water-like models, Mol. Phys. 26, 789–792(1973).

[4] Bockris, J. O., Reddy, A. K. N., & Gamboa-Aldeco, M. (2000), Modern Electrochemisty 2A:Fundamentals of Electrodics, 2nd edn. Norwell, MA: Kluwer Academic Publishers.

[5] Cai, W., Computational Methods for Electromagnetic Phenomena: electrostatics in solvations, scattering, and electron transport, Cambridge University Press.

[6] Cai, W., Deng, S., Jacobs, D.: Extending the fast multipole method to charges inside or outside a dielectric sphere. J. Comput. Phys. 223, 846-864 (2007)

[7] Carrier, J., Greengard, L.F., Rokhlin, V.: A fast adaptive multipole algorithm for particle simulations. SIAM J. Sci. Stat. Comput. 9, 669-686 (1988)

[8] Cheng, H., Greengard, L.F., Roklin, V.: A fast adaptive multipole algorithm in three dimensions. J. Comput. Phys. 155, 468-498 (1999)

[9] Davis, M.E., McCammon, J.A., Electrostatics in biomolecular structure and dynamics, Chem. Rev. 90, 509-521 (1990).

[10] Debye, P. & Hückel, E. (1923), "The theory of electrolytes. I. Lowering of freezing point and related phenomena", Physik. Z. 24, 185-206.

[11] Deng, S., Cai, W.: Discrete image approximations of ionic solvent induced reaction field to charges. Commun. Comput. Phys. 2, 1007-1026 (2007)

[12] Deng, S., Cai, W.: Extending the fast multipole method for charges inside a dielectric sphere in an ionic solvent: High-order image approximations for reaction fields. J. Comput. Phys. 227, 1246-1266 (2007)

[13] Deng, S., Xue, C., Baumketner, A., Jacobs, D., Cai, W., Generalized image charge solvation model for electrostatic interactions in molecular dynamics simulations of aqueous solutions, J. Comput. Phys., submitted, 2012.

[14] Esselink, L.: A comparison of algorithms for long-range interactions. Comput. Phys. Commun. 87, 375-395 (1995)

[15] Frenkel, D. & Smit, B. (2001), Understanding Molecular Simulation, 2nd edn. New York: Academic Press.

[16] Friedman, H.L., Image approximation to the reaction field, Mol. Phys. 29, 1533–1543 (1975).

[17] Gautschi, W.: Algorithm 726: ORTHPOL - a package of routines for generating orthogonal polynomials and Gauss-type quadrature rules. ACM Trans. Math. Softw. 20, 21-62 (1994)

[18] Gouy, G. (1910), "About the electric charge on the surface of an electrolyte", J. Phys. (France) 9, 457-468.

[19] Gradshteyn, I.S., Ayzhik, I.M.: Table of Integrals, Series, and Products. Academic Press, Boston (1994)

[20] Greengard, L.F.: The Rapid Evaluation of Potential Fields in Particle Systems. MIT, Cambridge (1987)

[21] Greengard, L.F., Rokhlin, V.: A fast algorithm for particle simulations. J. Comput. Phys. 73, 325-348 (1987)

[22] Greengard, L.F., Roklin, V.: A new version of the fast multipole method for the Laplace equation in three dimensions. Acta Numer. 6, 229-269 (1997)

[23] Greengard, L.F., Huang, J.: A new version of the fast multipole method for screened Coulomb interactions in three dimensions. J. Comput. Phys. 180, 642-658 (2002)

[24] Juffer, A., Botta, E.F.F., van Keulen, B.A.M., van der Ploeg, A., Berendsen, H.J.C.: The electric potential of a macromolecule in a solvent: A fundamental approach. J. Comput.Phys. 97, 144-171 (1991)

[25] Kirkwood, J.G., Theory of solutions of molecules containing widely separated charges with special applications to awitterions, J. Chem. Phys. 2, 351–361 (1934).

[26] Hill, T.L., An Introduction to Statistical Thermodynamics. New York, NY: Dover, 1987.

[27] Holst, M., The Poisson-Boltzmann equation: Analysis and multilevel numerical solution, 1994.

[28] Lee, M.S., Olson, M.A.: Evaluation of Poisson solvation models using a hybrid explicit/implicit solvent method. J. Phys. Chem. B 109, 5223-5236 (2005)

[29] Lee, M.S., Salsbury Jr., F.R., Olson, M.A.: An efficient hybrid explicit/implicit solvent method for biomolecular simulations. J. Comput. Chem. 25, 1967-1978 (2004)

[30] Lin, Y., Baumketner, A., Deng, S., Xu, Z.L., Jacobs, D., Cai, W., An Image-based reaction field method for electrostatic interactions in molecular dynamics simulations of aqueous solutions, the Journal of Chemical Physics, 131, 154103 (2009).

[31] Lindell, I.V: Electrostatic image theory for the dielectric sphere. Radio Sci. 27, 1-8 (1992)

[32] Lu, B., Cheng, X., McCammon, J.A.: New-version-fast-multipole-method accelerated electrostatic calculations in biomolecular systems. J. Comput. Phys. 226, 1348-1366 (2007)

[33] Morse, P.M., Feshbach, H.: Methods of Theoretical Physics. McGraw-Hill, New York (1953)

[34] Neumann, C.: Hydrodynamische Untersuchen nebst einem Anhang uber die Probleme der Elecktrostatik und der magnetischen Induktion. Teubner, Leipzig. 279-282 (1883)

[35] Norris, W.T.: Charge images in a dielectric sphere. IEE Proc.-Sci. Meas. Technol. 142, 142-150 (1995)

[36] Okur, A., Simmerling, C.: Hybrid explicit/implicit solvation methods. In Spellmeyer, D. (Ed.), Annu. Rep. Comput. Chem., Vol. 2, Chapter 6 (2006)

[37] Phillips, J.R., White, J.K.: A precorrected-FFT method for electrostatic analysis of complicated 3-D structures. IEEE Trans. Comput.-Aided Des. Integr. Circuits Syst. 10, 1059-1072 (1997)

[38] Schlick, T., Molecular Modeling and Simulation: An Interdisciplinary Guide, Springer, New York, 2002.

[39] Tanford, C., Kirkwood, J.G. , Theory of protein titration curves. I. General equations for impenetrable spheres, J. Am. Chem. Soc. 79, 5333–5339(1957).

[40] Ying, L., Biros, G., Zorin, D.: A kernel-independent adaptive fast multipole algorithm in two and three dimensions. J. Comput. Phys. 196, 591-626 (2004)

[41] Xu, Z., Cai, W., Fast analytical methods for macroscopic electrostatic models in biomolecular simulations, SIAM Rev. 53, pp. 683-720.

[42] Xu, Z., Deng, S., Cai, W., Image charge approximations of reaction fields in solvents with arbitrary ionic strength, J. Comput. Phys., 228 , 2092–2099(2009).

[43] http://en.wikipedia.org/wiki/Cubic_equation